Optical properties of low-dimensional semiconductor nanostructures

Janneke Blokland

Optical properties of low-dimensional semiconductor nanostructures
Janneke H. Blokland
Thesis Radboud Universiteit Nijmegen - Illustrated
With references - With summary in Dutch
ISBN: 978-90-9024824-0
NUR-code: 926
Cover: Photography by Peter Albers. Design by the author.

Optical properties of low-dimensional semiconductor nanostructures

een wetenschappelijke proeve op het gebied van
de Natuurwetenschappen, Wiskunde en Informatica

PROEFSCHRIFT

ter verkrijging van de graad van doctor
aan de Radboud Universiteit Nijmegen,
op gezag van de Rector Magnificus prof. mr. S.C.J.J. Kortmann,
volgens besluit van het College van Decanen
in het openbaar te verdedigen
op woensdag 6 januari 2010,
om 13:30 uur precies

door

Jantje Hendrika Blokland

geboren op 5 november 1982
te Tiel

Promotor: Prof. dr. ir. J. C. Maan

Copromotor: Dr. P. C. M. Christianen

Manuscriptcommissie: Prof. dr. W. J. van der Zande

Prof. dr. P. M. Koenraad
(Technische universiteit Eindhoven)

Prof. dr. A. Meijerink
(Universiteit Utrecht)

Het werk beschreven in dit proefschrift is uitgevoerd aan de faculteit der Natuurwetenschappen, Wiskunde en Informatica van de Radboud Universiteit Nijmegen

Das wovor wir leben, das worin wir leben, woraus und worein wir leben, das Geheimnis: es ist geblieben, was es war.

Martin Buber
Ich und Du, 1923

Voorwoord

Het voorwoord is het meest gelezen onderdeel van bijna alle proefschriften en de plek bij uitstek om mensen te bedanken. Met het risico iemand te vergeten, zijn er toch mensen die ik wil noemen in het bijzonder. In 2006 ben ik afgestudeerd en direct daarna begonnen aan mijn promotie bij het HFML. Vanaf het begin heb ik de vrijheid gehad om mijn eigen project vorm te geven, waarvoor ik mijn begeleiders, Peter en Jan Kees wil bedanken.

Frans, vanaf de eerste dag dat ik op het HFML kwam, heb ik met jou samen gewerkt. Op zoek naar single dots, naar de hoek θ in een model of naar een tafeltennistafel; we hebben veel samen gedaan en ik heb veel van je geleerd. Ik ben blij dat we een goede vriendschap aan deze tijd hebben overgehouden. Tijdens de vaak nachtelijke experimenten heb ik veel samengewerkt met externe gebruikers. Niek, ik ben blij dat we na ruim drie jaar eindelijk een single ring bij dertig Tesla hebben gezien en hoop dat we ook zonder wetenschappelijk excuus nog een keer een biertje gaan drinken. Also all other users, Gregor, Dima, Boris, Daniele, Lola, Alfonso, Eric, Antonio and Lyuda, I would like to thank for the nice and fruitful collaborations. Ook dank aan mijn collega's Jeroen, Jos, Erik en Erik, Victor, Arend, Genia, Alix, Giorgio, Iris en Vadym. Ik heb veel van jullie geleerd en ook was het vaak gezellig tijdens de meetnachten en -weekenden.

Victor, misschien waren we iets productiever geweest zonder elkaar, maar het was zeker minder leuk geweest. En aan wie had ik dan al mijn verhalen kwijt gemoeten? Het is goed om mensen zoals jij en TuHa te hebben voor een avond gezellig eten en spelletjes spelen, en die ook nog snappen wat een promotie niet altijd even gemakkelijk maakt.

Andries Meijerink en Paul Koenraad ben ik erkentelijk voor het lezen van mijn proefschrift, dat voor een groot deel op waardevolle samenwerkingen en discussies met jullie is gebaseerd. Ook ben ik blij dat Wim van der Zande mijn proefschrift heeft gelezen. Gedurende mijn hele promotie heb ik bij jou binnen kunnen lopen en je hebt altijd vertrouwen gehad dat dit proefschrift er zou komen, zelfs als ik dat niet had. Mijn dank hiervoor is groot. In het eerste jaar van mijn promotie heb ik gewerkt aan een opstelling voor optica in gepulste magneetvelden. Lijnis, jij hebt eigenlijk de opstelling gebouwd en vaak had je al iets gemaakt voordat ik het bedacht had. Ook de insert waarmee we enkele objecten meten in hoge magneetvelden hebben we samen ontworpen en heb jij gemaakt, tot aan de plaatjes in mijn proefschrift toe. Ook jullie, Ramon, Jos, Harry, Hung, Peter, Stef, Jos, Uli, Hans, Andries en Ine wil ik bedanken voor de goede samenwerking. To learn how to use a pulsed magnet, I have been to the LNCMP at Toulouse. Stefan, I am very grateful that you helped me intensively those two months, inside and outside the lab. I hope the next years I will experience that Berlin truly is the best place of Europe.

One of the reasons to start a PhD project was the experience of being a summer student at CERN. Ann and Olav, thank you very much for the great and inspiring time I had in the RICH2 group. Tijdens werkuren, ben ik talloze keren heen en weer gelopen naar het Huygensgebouw. José, de gezelligheid in jouw kantoor en op de afdeling was vaak de belangrijkste reden hiervoor. Ik vind het dan ook leuk dat jij en Victor mijn paranimfen willen zijn. Ook jou, Lieke wil ik bedanken voor de gezelligheid en steun van afstand, maar toch dichtbij. Tim en Antje, jullie wil ik in het bijzonder bedanken voor de vele avonden samen eten en de korte vakanties. Ok, misschien was mijn hotelkeuze niet altijd even sterk, maar het was toch wel gezellig. Tijdens een groot deel van mijn vakanties tijdens mijn studententijd, en een wat kleiner deel tijdens mijn promotietijd heb ik altijd met veel plezier sportartikelen verkocht. Henk-Jan, Jacko, Daniëlle en Henrie, altijd als ik binnen loop, hebben jullie tijd voor een praatje en ook de volgende barbecue ben ik er weer graag bij . . .

Ook buiten het werk om, heb ik veel plezier en steun gehad van familie en vrienden in en om de universiteit, te veel om allemaal op te noemen. Zo kan ik me me moeilijk voorstellen wat een dinsdagavond is zonder repetitie in Ochten. Nijmegen-Ochten was nog een acceptabele afstand, maar Berlijn-Ochten wordt toch wel erg ver, maar ik kom zeker luisteren naar ons 100-jarig-jubileumconcert. Vanaf het eerste moment dat ik in Nijmegen woon, heb ik me erg welkom gevoeld in de Petruskerk: tijdens de JIP-avonden, het weekend naar Diever, de kindernevendienst en alle andere activiteiten. Ik heb altijd veel gezelligheid en inspiratie ervaren van jullie allen en ik vind het jammer dat ik weg ga in deze tijd van opbouw aan een nieuwe gemeenschap.

Wat is een paragraaf zonder conclusie? Daarom samenvattend, wil ik iedereen met wie ik een korter of langer stukje ben meegelopen op mijn weg, bedanken en in het bijzonder mijn familie: mijn ouders, Els en Mark op wie ik altijd heb kunnen en kan terugvallen.

Janneke, november 2009

Contents

Chapter 1

General introduction

The field of nanotechnology started about fifty years ago with Richard Feynman's talk *There is plenty of room at the bottom*, and is now amongst the most active research fields in biology, chemistry and physics. The prefix nano, denoting the factor 10^{-9}, originates from the Greek $\nu\alpha\nu o\varsigma$ meaning dwarf. With nanoscience we usually mean the study of structures with one or more dimensions in the range of $1 - 100$ nanometers. In the past decades the ability to produce new materials on the nanometer scale has increased substantially. Nanostructures can be for example based on naturally occurring structures such as DNA [1] or can be large supra-molecular structures [2].

Right from the beginning semiconducting materials have played an important role in the development of nanoscience. In 1970 Esaki en Tsu proposed the fabrication of the first two-dimensional nanostructure, a superlattice: an artificial periodic structure, consisting of alternating layers of different semiconductors [3]. Growth techniques such as molecular beam epitaxy were developed further and in 1993 Leonard et al. showed the formation of epitaxially grown quantum dots [4]: islands of semiconductor material in which electrons are confined in all three directions.

Next to the development of these top-down fabricated nanostructures, methods have been developed to create semiconductor nanostructures by chemical synthesis [5, 6], so-called colloidal nanocrystals. The main advantage of these nanocrystals over epitaxially grown quantum dots is that they are easy to fabricate. Moreover, the size and shape of the nanocrystals can be relatively easily varied by changing the synthesis process. Colloidal nanocrystals are usually synthesized in solution, which makes them also promising candidates for biolabeling. Recently, it has become possible to synthesize such as quantum rods and tetrapod-shaped nanocrystals [7,8]. Technologically, all of these nanomaterials have proven to be relevant in electro-optical applications such as lasers [9], single photon sources [10] and infrared photodetectors [11].

In this thesis we describe the study of optical properties of several low-dimensional semiconductor nanostructures in high magnetic fields. The central question of this thesis is *How do electrons behave in low-dimensional semiconductor nanostructures?* We define low-dimensional structures here as structures in which electrons behave as if they can only move freely in two or less dimensions. On the one hand we try to answer this question by exploring the energy levels of single electrons in semiconductor nanostructures, on the other hand we study the correlations between electrons. In both cases we find that not only the dimensionality - usually given by the shape of the nanostructure - is important, but many other factors contribute. Amongst these are the material of which the nanostructure is made and the symmetry of the electronic bandstructure. Also the number of electrons and the occupation of the electron levels can change the electronic behavior significantly as well as the environment of the nanostructure, such as their surface and the template on which they are grown.

To answer the question stated above we use optical experiments in high magnetic fields. Optical experiments have given direct evidence for the low-dimensional behavior of electrons and holes in confined semiconductors. The density of states of the electrons changes from a parabola in three dimensions to a staircase in two dimensions to atomic-like isolated energy levels in zero dimensions. For an optical transition to be allowed, the electric-dipole matrix element of the transition has to be non-zero. This condition, combined with the symmetry of the system, is translated into the so-called optical selection rules. For example, we know that a photon carries one unit of angular momentum and does not interact with spin. These restrictions on the observed optical transitions help to identify the initial and final state of the system.

The magnetic field is an important tool to explore the energy levels of low-dimensional structures. We can estimate the dimensions of a nanostructure by measuring the diamagnetic shift. Furthermore we lift the degeneracy of the two spin polarizations of the electrons, which is caused by the anomalous Zeeman effect. Charged particles in a magnetic field have quantized cyclotron orbits which have discrete energy values, so-called Landau levels. In high magnetic fields this leads for example to the observation of the quantization of the conductivity in two-dimensional systems, the quantum Hall effect. Also the magnetic field can change the properties of the wave functions, such as the coupling between electrons and even new states of matter can be induced by the magnetic field. An example of the latter is the incompressible quantum liquid formed by electrons in a two-dimensional electron system where all electrons reside in the lowest Landau level, also known as the fractional quantum Hall effect [12].

This thesis is divided into seven chapters. Chapter 2 is an introduction to the basic physics of semiconductor nanostructures in magnetic fields. The essential concepts of the different nanostructures that are studied in this thesis are explained, so the more detailed studies in Chapter 4 to 7 can be fully appreciated. After this chapter, two of the experimental setups used to measure optical properties in high magnetic fields are described in Chapter 3. The last four chapters are each devoted to a different type of low-dimensional nanostructure.

In Chapter 4 we show the results of a combined study of the energy levels and physical structure of self-assembled indium-arsenide quantum dots and the effect of growing these dots on a patterened superlattice. These results are important to fully understand the relation between the structural and spectroscopic properties of nanostructures.

By changing the growth procedure of self-assembled InAs quantum dots, it is possible to grow nanostructures with a hole in their middle, thus changing from a dot-like to a ring-like geometry. The aim of Chapter 5 is to study what the implications of this ring-like geometry are for the energy levels. In the first part of this chapter we show the results of photoluminescence measurements on an ensemble of quantum rings at different excitation powers. The obtained spectra are broad, due to the averaging over a large number of rings. To obtain a higher spectroscopic resolution, we show in the second part of this Chapter measurements on individual quantum rings, where we look at the ground state emission of individual nano-objects.

Colloidal nanocrystals are the subject of Chapter 6. In the first part we show that we can change the exciton fine structure of cadmium-selenide nanocrystals by changing their shape from spherical to elongated. This change in the fine structure of the lowest confined state has a dramatic effect on the photoluminescence of the elongated rods, which is explained by a magnetic-field dependent mixing of energy levels. In the second part of this Chapter we study the temperature dependent circularly polarized emission of spherical nanocrystals of different materials having a completely different crystal symmetry and electronic band structure.

In Chapter 7 we show that we can optically probe the electronic fractional quantum Hall states. We study the emission of high-quality heterojunctions at low temperatures and in high magnetic fields, where the electrons form a correlated incompressible quantum liquid.

In all experiments we have performed, we find that it is not *only* the dimensionality of a nanostructure that determines the behavior of the electrons. The variety of low-dimensional systems is too large to draw a general conclusion on their properties. However, the dimensionality of an object often determines the starting point, from which we can begin to understand the complex behavior of confined electrons.

References

[1] Seeman, N. *Nano Letters* **1**, 22 (2001).

[2] Lehn, J. *Nobel Lecture in Chemistry* (1987).

[3] Esaki, L. and Tsu, R. *IBM J. Res. Devel.* **14**, 61 (1970).

[4] Leonard, D., Krishnamurthy, M., Reaves, C. M., Denbaars, S. P., and Petroff, P. M. *Appl. Phys. Lett.* **63**, 3203–3205 (1993).

[5] Ekimov, A., Efros, A. L., and Onushchenko, A. *Solid State Comm.* **56**, 921 (1985).

[6] Alivisatos, A. *Science* **271**, 933 (1996).

[7] Manna, L., Scher, E. C., and Alivisatos, A. P. *J. Am. Soc. Chem.* **122**, 12700 (2000).

[8] Milliron, D. J., Hughes, S. M., Cui, Y., Manna, L., Li, J., Wang, L.-W., and Paul Alivisatos, A. *Nature* **430**, 190 (2004).

[9] Arakawa, Y. and Sakaki, H. *Appl. Phys. Lett.* **40**, 939 (1982).

[10] Zhiliang, Y., Kardynal, B., Stevenson, R., Shields, A., Lobo, C., Cooper, K., Beattie, N., Ritchie, D., and Pepper, M. *Science* **295**, 102 (2002).

[11] Chu, L., Zrenner, A., Böhm, G., and Abstreiter, G. *Appl. Phys. Lett.* **75**, 3599 (1999).

[12] Tsui, D. C., Stormer, H. L., and Gossard, A. C. *Phys. Rev. Lett.* **48**, 1559 (1982).

Chapter 2

Low dimensional semiconductors in magnetic fields

Abstract

In this chapter we discuss the basic physics of confined semiconductor systems and the effect of a magnetic field on their energy levels. The focus is on the optics of the nanostructures discussed in this thesis: epitaxially grown quantum dots, quantum rings and heterojunctions and colloidal II-VI and IV-VI nanostructures. This chapter provides a general introduction to the physics playing a role in these nanostructures, such as the Aharonov-Bohm (AB) effect for quantum rings, the exciton fine structure of the ground state for colloidal dots and the fractional quantum Hall effect for high-quality heterojunctions.

2.1 Optics of confined semiconductors

Optical excitations in a semiconductor lead to the formation of excitons, pairs of photo-excited electrons in the conduction band and holes in the valence band bound together by the Coulomb interaction. The energy of the excitons in a bulk semiconductor is determined by the bandstructure of the material. The semiconductors considered here all have four valence electrons which are derived from the s (orbital angular momentum $L = 0$) and p (orbital angular momentum $L = 1$) atomic orbitals. When these atoms are brought together they form bonding and antibonding states. In a crystalline solid these bonding and antibonding states evolve to a valence band filled with electrons and an empty conduction band seperated by an energy gap (Figure 2.1). The top of the valence band corresponds to the highest bonding states and has a p-like character. The bottom of the conduction band is the lowest antibonding state and therefore has an s-like character.

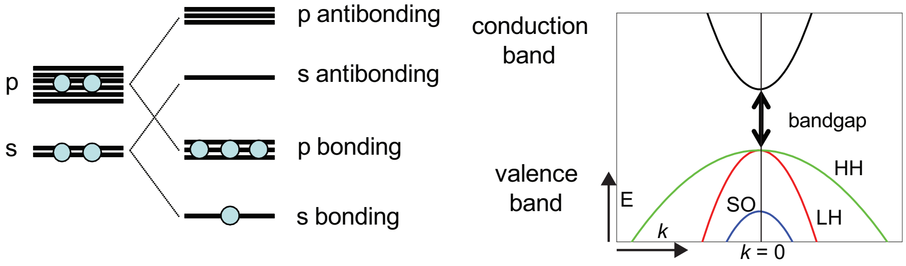

Figure 2.1: *Schematic picture of the covalent bonding in direct gap IV-IV, III-V and II-VI semiconductors leading to a single lowest conduction band and three highest valence bands.*

The conduction band can be well described around its minimum (i.e. for wavevectors k close to zero, cf. Figure 2.1) by a single parabola. This follows from the atomic s symmetry of the lowest bonding state. The valence band cannot be described by a single parabola, but consists of three different bands. Due to the spin-orbit interaction the total angular momentum $\vec{J} = \vec{L} + \vec{S}$ is a good quantum number. The total angular momentum of the conduction band is therefore $S_e = 1/2$ with the projections $m_{S_e} = \pm 1/2$. Here we have used for convention the symbol S_e for the total angular momentum of the conduction band. In the same way we see that the valence band has a state with total angular momentum $J_h = 3/2$ and one with total angular momentum $J_h = 1/2$. The latter is the so-called split-off (SO) band, which is much lower in energy and is therefore not considered any further.

The state with total angular momentum $J_h = 3/2$ has projections $m_{J_h} = \pm 3/2$, the heavy holes and $m_{J_h} = \pm 1/2$, the light holes. The notion of heavy and light holes follows from the curvature of the bands, which is inversely proportional to the effective mass:

$$\frac{1}{m^*} = \frac{1}{\hbar^2}\frac{\partial^2 E}{\partial k^2}. \tag{2.1}$$

In the approximation of parabolic bands, electrons and holes behave as free particles, only having a mass different from the mass of free electrons. The value of the effective mass is thus a result of all the interactions of the electrons with the host material. The energy levels of confined systems scale inversely with the mass of the confined particles. Since the electrons in the light-hole (LH) and heavy-hole (HH) bands have a different effective mass, their degeneracy is lifted in confined systems.

During the creation and the recombination of excitons, the total angular momentum has to be conserved. This leads to the selection rule that only transitions with $\Delta m_J = m_{S_e} + m_{J_h} = \pm 1$ are allowed. Exciton states with $m_J = \pm 1$ ($m_J \neq \pm 1$) are called "bright" ("dark") exciton states.

The transition from bulk-like behaviour to the confinement regime occurs roughly when the dimensions of the nanostructure become smaller than the exciton Bohr radius of the material. The exciton Bohr radius of a bulk semiconductor is given by:

$$a_X = \frac{4\pi\epsilon_0\epsilon_r\hbar^2}{m^* e^2} = \frac{m_0\epsilon_r}{m^*}a_H, \tag{2.2}$$

where m^* is the effective exciton mass of the material and a_H is the Bohr radius of the hydrogen atom ($a_H = 5.29 \cdot 10^{-11}$ m). Table 2.1 gives an overview of exciton Bohr radii of the materials used in this thesis.

The effect of the magnetic field on a nanostructure can be estimated by comparing the confinement potential of the nanostructure with the confinement induced by the magnetic field. A rough comparison between the two contributions can be made by comparing the dimensions of the nanostructures to the magnetic length:

$$l_m = \sqrt{\frac{\hbar}{eB}} \tag{2.3}$$

For a magnetic field of 30 T the magnetic length is 4.7 nm, which is comparable to the dimensions of nanostructures investigated in this thesis, so significant effects of the magnetic field are expected.

Material	a_X (nm)	E_g (eV)	Crystal structure
CdSe	5.4	1.84	Zincblende or Wurtzite
CdTe	6.7	1.61	Zincblende
GaAs	13	1.52	Zincblende
InAs	34	0.42	Zincblende
PbS	18	0.29	Rock salt
PbSe	46	0.17	Rock salt

Table 2.1: *Exciton Bohr radius (a_X), direct band gap (at $T \approx 0\,K$) and crystal structure of the semiconductor materials used in this thesis [1–4].*

Energy scales

A better way to estimate the relative importance of the physical processes, such as the confinement, the binding energy, the temperature and the magnetic field is to compare their energy scales. In the following we will give an overview of the energy scales relevant for this thesis. Although the formulas given here are mostly oversimplified to apply for a specific problem, they give a good indication for the relative magnitudes of the energies.

The **confinement energy** of a nanostructure is given by

$$E_{\text{conf}} = \frac{\hbar^2 \pi^2}{2m^*} \left(\frac{n_x}{l_x^2} + \frac{n_y}{l_y^2} + \frac{n_z}{l_z^2} \right) \tag{2.4}$$

where $l_{x,y,z}$ are the dimensions of the nanostructure in the three dimensions. For $n_x = n_y = n_z = 1$ these energies range from about 50 meV, which is the lateral confinement for epitaxial quantum dots to several eV for the smallest colloidal nanostructures.

The typical energy scale of the magnetic field is expressed by the **cyclotron energy**

$$E_c = \hbar\omega_c = \frac{\hbar e B}{m^*} \tag{2.5}$$

which is 50 meV for electrons in GaAs ($m^* = 0{,}067 m_0$) at $B = 30\,\text{T}$. In a magnetic field Landau levels are formed with energy

$$E = \left(N + \frac{1}{2} \right) E_c. \tag{2.6}$$

The **Zeeman spin splitting** for electrons in a magnetic field splits the two spin polarized levels and is given by

$$\Delta E_{\text{Zeeman}} = g\mu_B S_z B, \tag{2.7}$$

where the Landé g factor determines the magnitude of the slope of the shift and $\mu_b = e\hbar/2m_e$ is the Bohr magneton. In contrast to atoms, the Landé factor depends strongly on the size, shape and material of the nanostructure due to the spin-orbit coupling and ranges here from $g \approx$ -1 for the electrons in epitaxial dots which are the subject of Chapter 4 to $g \approx$ -30 for the excitons in the colloidal quantum rods studied in Chapter 6. For $g = 1$ the both spin polarized energy levels of the electrons have an additional splitting of 3 meV at 30 T.

The average **thermal energy** of the atoms in a solid is given by $k_B T$, which is 6 μeV at $T = 1$ K and 25 meV at room temperature. Therefore most experiments are performed at low temperatures to minimize the effect of thermal processes.

The Coulomb interaction between two electrons, two holes or an electron and a hole can usually be added as a pertubation under the assumption that the quantization energies are larger than the Coulomb energies. The Coulomb energy for interactions between two electrons (holes) can be written as the sum of two integrals, the **direct Coulomb energy**, representing the electrostatic interaction between the electrons (holes),

$$E^c_{ij} = \frac{e^2}{4\pi\epsilon_r\epsilon_0} \int\int \frac{|\psi_i(\mathbf{r}_1)|^2 |\psi_j(\mathbf{r}_2)|^2}{|\mathbf{r}_1 - \mathbf{r}_2|} d\mathbf{r}_1 d\mathbf{r}_2 \tag{2.8}$$

and the **exchange Coulomb energy**, arising from the antisymmetrization of the wavefunctions and having no classical interpretation

$$E^x_{ij} = \frac{-e^2}{4\pi\epsilon_r\epsilon_0} \int\int \frac{\psi_i(\mathbf{r}_1)^* \psi_j(\mathbf{r}_2)^* \psi_i(\mathbf{r}_2) \psi_j(\mathbf{r}_1)}{|\mathbf{r}_1 - \mathbf{r}_2|} d\mathbf{r}_1 d\mathbf{r}_2 \tag{2.9}$$

The Coulomb energy for the interaction between an electron and a hole in an exciton is given by equation 2.8 for an electron at position $\mathbf{r}_1$ and a hole at position $\mathbf{r}_2$. Obviously there is no exchange integral for an electron and a hole in this approximation, because the two charge carriers are distinguisable.

Not all energies are relevant for every nanostructure. For example, if we charge a nanostructure Coulomb interactions will be more important than if the system is charge-neutral. Also the relative importance of the confinement and thermal energy will depend both on the temperature of the experiment and the size of the nanostructure. In the following subsections we discuss the characteristic properties of the nanostructures studied in this thesis.

2.2 Epitaxial quantum dots and rings

Quantum dots are often regarded as "artificial atoms", since they have discrete energy levels with a shell-like structure. Quantum dots show some behavior similar to that of atoms, such as the Zeeman spin splitting in a magnetic field. However, since the height of the epitaxial quantum dots and quantum rings we have investigated is an order of magnitude smaller than their lateral extent, they are regarded as circularly symmetric, instead of the spherically symmetric hydrogen atom. Also the confinement potential in quantum dots (harmonic) is different from that of the hydrogen atom (Coulomb potential).

Quantum dots can be made in different ways, such as by lithography, chemical synthesis or molecular beam epitaxy (MBE). The quantum ring and (coupled) quantum dot samples we study in Chapter 4 and 5 are fabricated by the latter method and their basic characteristics are discussed in this paragraph. The typical lateral extent of these nanostructures is 10-50 nm.

2.2.1 Quantum dots: the two-dimensional harmonic oscillator

For epitaxial quantum dots the energy levels of the electrons are well described by regarding the dot as a two-dimensional harmonic oscillator. The Hamiltonian of two-dimensional harmonic oscillator in a magnetic field in the z-direction is given by

$$H = \frac{1}{2m^*}(\vec{p} - e\vec{A})^2 + \frac{1}{2}m^*\omega_0 r^2, \tag{2.10}$$

where the first term describes the particle moving in the xy-plane perpendicular to a magnetic field with vector potential $\vec{A}$ and the second term describes the lateral confinement, which is assumed to be harmonic with oscillator frequency ω_0. In this paragraph we do not take into account the Zeeman spin splitting, giving all energy levels an additional two-fold degeneration which is lifted by the magnetic field. The energy of the electron (hole) levels is determined by the eigenvalues of the Schrödinger equation and is given by the so-called Fock-Darwin energy levels [5–7] (Figure 2.2):

$$E_{l,m_z} = (l+1)\hbar\sqrt{\omega_0^2 + \left(\frac{\omega_c}{2}\right)^2} + \frac{1}{2}\hbar m_z \omega_c, \tag{2.11}$$

where $\omega_c = eB/m^*$ is the cyclotron frequency, m^* is the effective electron (hole) mass and $l, m_z = -l, -l+2, ..., l-2, l$ are the quantum numbers corresponding to the different energy levels[1].

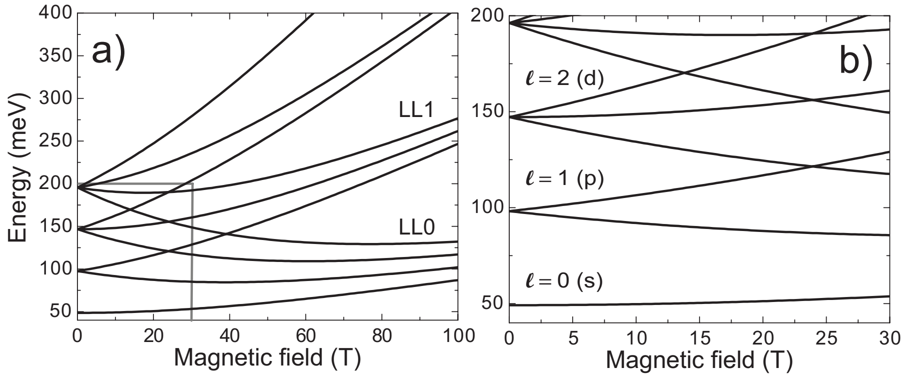

Figure 2.2: *Electron s, p, and d Fock-Darwin energy levels for a two-dimensional harmonic oscillator versus perpendicular magnetic field. $\hbar\omega = 55\,\text{meV}$. The values of the confinement energy and effective mass are taken from literature [7] and comparable to those of the quantum dots used in this thesis. a) Energy levels up to $B = 100$ T, where at high fields the magnetic confinement becomes dominant and Landau levels (LL0, LL1) are formed. b) Zoom in of the energy levels up to $B = 30$ T, where the confinement dominates.*

The naming of the quantum dot energy levels is analoguous to the shell-like energy level structure of atoms:

shell	l	m_z
s	0	0
$p_\pm$	1	± 1
d_0	2	0
$d_\pm$	2	± 2

For low magnetic fields the potential is predominantly determined by the confinement of the charge carriers, for higher magnetic fields the magnetic potential becomes more important and Landau levels are formed, as shown in Figure 2.2a. For the dots investigated in this thesis we will not reach the Landau level limit up to 30 T. These Fock-Darwin energy levels have proven to predict the enery of electron levels very well. For the hole levels the situation

---

[1] In terms of the total angular momentum quantum number j equation 2.11 looks like $E_{j,j_z} = \hbar(2j+1)\sqrt{\omega_0^2 + \left(\frac{\omega_c}{2}\right)^2} + \hbar j_z \omega_c$. However, in literature it is conventional to use the quantum numbers $l = 2j$ and $m_z = \frac{1}{2}j_z$.

is more complicated, since the HH and LH valence bands mix and the holes have a larger effective mass. The latter makes that the energy separation between the confined levels is of the same order as the Coulomb energies, which prohibits a pertubative inclusion of the Coulomb interaction. In Chapter 4 we study the single particle hole levels by photoluminescence spectroscopy, using optical selection rules and the well-known energy levels of electrons in a quantum dot. In the quantum dots we considered, the Coulomb interaction only weakly affects the optical spectra and therefore we simply add the electron and hole contributions to obtain the exciton structure. In addition to the optical selection rule for the total angular momentum $\Delta m_J = \pm 1$ only transitions with $\Delta l = \Delta m_z = 0$ are allowed, so we only observe $s - s$, $p_\pm - p_\pm$, ... transitions.

In the first part of Chapter 4 we study the quantum numbers of the hole levels of semiconductor quantum dots, taking into account both the Coulomb interaction and valence band mixing. Furthermore we study the relation between the size, shape and structure of quantum dots and their energy levels. Although in literature usually assumptions are made on the geometry of the dots, we combine structural and spectroscopic information to find how the geometry of the dots affects its energy levels. The last part of Chapter 4 is devoted to the study of clusters of coupled InAs quantum dots. These so-called quantum dots molecules grown on a superlattice are coupled and show a behavior which is completely different from that of the isolated quantum dots we have investigated. From the spectroscopic data, we try to understand deduce through which mechanism these dots are coupled.

2.2.2 Quantum rings: the Aharanov-Bohm effect

To find the energy levels we use the Hamiltonian given in 2.10, without the second term describing the harmonic potential. Furthermore we use that the vector potential $\vec{A} = \vec{\nabla}\chi$, since $B = 0$ at the rim of the ring. From the symmetry of the system we know that the wavefunction is periodic in the azimuthal angle ϕ: $\psi(\phi) = \psi(\phi + 2\pi)$. We find that the energy levels for the ring in a magnetic field (Figure 2.3) are given by

$$E_l = \frac{\hbar^2}{2m_e^* R^2}\left(\pm l + \frac{\Phi}{\Phi_0}\right) \tag{2.12}$$

where R is the radius of the ring $\Phi = \pi R^2 B$ is the flux penetrating the ring and $\Phi_0 = h/2e = 2.068 \cdot 10^{-15}$ Wb is the magnetic flux quantum.

In this approach, we describe the effect of the magnetic field by its vector potential. To simplify the problem we also have set the confinement potential to zero and neglected the Coulomb interactions. In Chapter 5 it is shown that

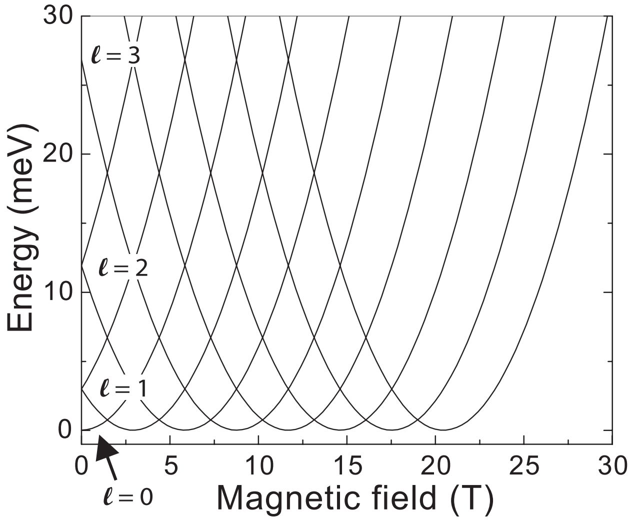

Figure 2.3: *Electron energy levels in a quantum ring for* $l = 0, 1, 2, 3$ *versus perpendicular magnetic field.* $m_e^* = 0.057 m_e$*,* $R = 15\,nm$*. The energy is given with respect to the lowest confined energy level at 0 T.*

this approach is oversimplified and cannot describe the exciton energy levels in realistic quantum rings.

In contrast to the energy levels of quantum dots, for quantum rings all the energy levels, except for the lowest one, are two-fold degenerate ($m_z = \pm l$) and the levels are not equidistant at 0 T. The main difference between the ground state of quantum dots and quantum rings is that for quantum dots the ground state always has a $l = 0$ character (cf. Figure 2.2), whereas for quantum rings the angular momentum of the ground state increases. This is a manifestation of the Aharanov-Bohm effect [8]: the magnetic field where two energy levels cross, is where the flux penetrating the ring is $\Phi = (N + \frac{1}{2})\Phi_0$. Also for quantum rings the optical selection rules $\Delta l = \Delta m_z = 0$ have to be obeyed.

In Chapter 5 we investigate the exciton energy structure of realistic quantum rings. By previously performed cross-sectional STM and magnetization measurements it has been shown that the quantum rings have a volcano-like shape and confined electrons show features of the AB-effect. By photoluminescence experiments on an ensemble of rings and on single rings we investigate what are the energy levels of neutral excitons. The main question is what distinguishes the quantum rings from quantum dots. We look at features typical for the ring geometry, such as the AB-effect, the two-fold degeneracy of the excited states and the orbital angular momentum of the ground state.

2.3 Colloidal nanocrystals

In colloidal nanocrystals the confinement in all three spatial directions is of the same order of magnitude, in contrast to the confinement in expitaxial quantum dots. For the latter we regard the energy levels with $n_z = 0; n_x = 0, 1, 2, ...; n_y = 0, 1, 2, ...$ (cf. equation 2.4). In colloidal nanocrystals we study energy levels with quantum numbers $n_x = 0, 1, 2, ...; n_y = 0, 1, 2, ...; n_z = 0, 1, 2, ...;$. The nanoscrystals we have studied are usually very small, so the confined levels are separated by a large energy. In the following we look only to the transition of electrons and holes in their lowest confined level. This transition dominates the optical properties of colloidal nanocrystals at low temperatures. In the general discussion in this paragraph we consider spherical nanocrystals surrounded by an infinite potential barrier. The energy of the confined electron and hole levels are written within the parabolic effective mass approximation (EMA) [9] as

$$E^{e,h}_{l,n} = \frac{\hbar^2 \phi^2_{l,n}}{2m^*_{e,h} a^2}, \tag{2.13}$$

where a is the crystal radius and $\phi_{l,n}$ is the nth root of the spherical Bessel function of order l. Also this equation the effective mass m^* appears, taking into account the interactions of the electons with in the host material. In Chapter 6 we will look to the fine structure of the exciton ground state ($1S_{h,3/2}1S_e$) of a nanocrystal, i.e. $l = n = 0$ and thus $\phi_{0,0} = \pi$.

For CdSe and CdTe, the exciton ground state is constructed from the two-fold degenerate state in the conduction band and the four-fold degenerate state (HH and LH) in the valence band, and therefore is eight-fold degenerate. However, this degeneracy is lifted, due to the symmetry of the lattice, the non-spherical shape of the nanocrystal, by which the heavy and light hole bands are split in energy (left side of Figure 2.4). The electron-hole exchange interaction cannot be treated as a pertubation for these crystals and splits the exciton levels into an $F = 1$ and an $F = 2$ multiplet (right side of Figure 2.4).

For wurtzite crystals, the eight-fold degenerate exciton ground states splits up into five levels due to the combination of above mentioned effects. Three of those levels are two-fold degenerate without a magnetic field, giving a sequence of bright (optically allowed) and dark (optically not allowed) exciton states. These states are characterized by their projections of the total angular momentum $F_m = J_h + s_z$: $F_m = \pm 2$, $F_m = \pm 1^U$, $F_m = \pm 1^L$, $F_m = 0^U$, $F_m = 0^L$ (Figure 2.4). Here the superscript U (L) denotes the upper (lower)

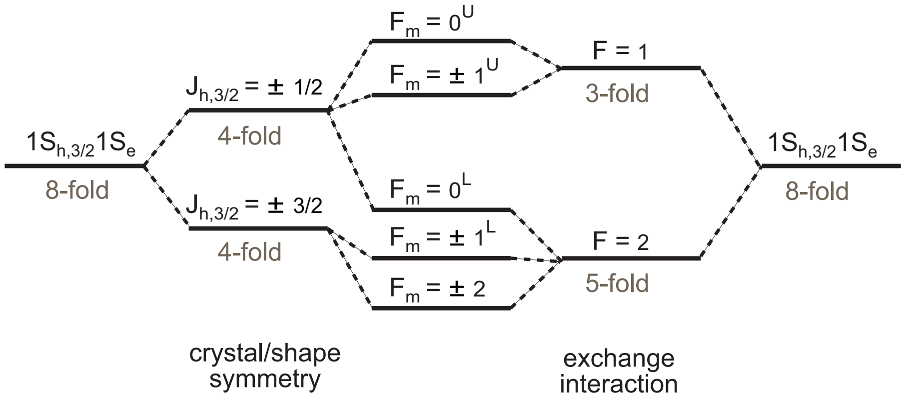

Figure 2.4: *Energy levels of the exciton fine structure of the lowest confined state $1S_{h,3/2}1S_e$ for a non-spherical quantum dot with wurtzite lattice symmetry. The eight-fold degenerate level is split into five levels due to the non-spherical shape of the dot, the crystal structure and the electron-hole exchange interaction. Figure after ref. [10].*

state with the same quantum number F_m. For zinc-blende crystals, having a higher symmetry, the exciton ground states splits up into only two levels. The energy and the sequence of the exciton F states depend strongly on the size and crystal structure of the nanocrystal, as can be seen in Figure 2.5, which shows the size dependent exciton fine structure for CdSe and CdTe NQDs. However, characteristic for both types of NQDs is the dark exciton ground state. For PbS and PbSe, the situation is even more complex, since both the conduction and valence band are eight-fold degenerate at their minimum. The description of this exciton fine structure, consisting of 64 energy levels, is beyond the scope of this thesis.

In a magnetic field exciton states with non-zero angular momentum split up into two circularly polarized components. Furthermore the magnetic field mixes the exciton states, causing the dark states to mix with the bright states and therefore gaining oscillator strength. The effect of the magnetic field strongly depends on the crystal symmetry, the size and shape of the nanocrystal and its orientation in the magnetic field. More details on the results of the exiton fine structure in a magnetic field within the EMA can be found in ref [9, 11].

In Chapter 6 we study which other parameters contribute to the exciton fine structure. More specifically, we study the influence of the shape and material properties on the optical emission.

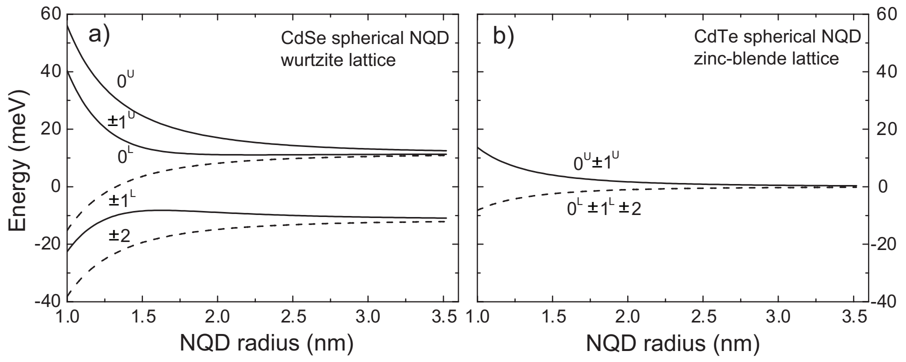

Figure 2.5: *Exciton energy levels as function of the NQD size. a) CdSe NQD with wurtzite lattice symmetry. b) CdTe NQD with zinc-blende lattice symmetry.*

2.4 The fractional quantum Hall effect

The integer quantum Hall effect (QHE) was discovered by Klaus von Klitzing and coworkers in 1980 [12], for which he was rewarded the Nobel Prize in Physics in 1985. They observed that the Hall conductivity σ of two-dimensional electron gases (2DEGs) is quantized at values

$$\sigma = \nu \frac{e^2}{h}, \tag{2.14}$$

where the filling factor

$$\nu = \frac{n_e}{B} \frac{hc}{e} \tag{2.15}$$

can take integer values. Here, n_e is the density of free electrons.

The integer QHE can be understood in terms of non-interacting electrons quantized in Landau levels. In 1982 Daniel Tsui and coworkers [13] discovered the fractional quantum Hall effect (FQHE), which in contrast to the integer quantum Hall effect, cannot be understood in terms of non-interacting electrons. It appeared that the electrons in a 2DEG at low temperatures behave as if they carry 1/3 of the elementary charge at the fractional filling factors $\nu = 1/3$. Experimentally it was also observed that small deviations of the electron density did not affect the conductivity.

2.4.1 Laughlin wavefunctions and fractional statistics

At low electron densities and high magnetic fields, such that $\nu < 1$, all electrons are in the lowest Landau level and mixing between Landau levels can be neglected. When the temperature and disorder are sufficiently low, the electrons form a strongly interacting system, from which the elementary excitations, quasi-electrons (QEs) and quasi-holes (QHs) are fractionally charged [14, 15]. Robert Laughlin [15] showed that at fractional filling factors $\nu = \frac{p}{q}$, where p and q are integers, electrons condense into an incompressible liquid state. The eigenstates of the $\nu = \frac{1}{q}$ state are described by a many-body wavefunction

$$\psi_m = \prod_{i<j}(z_i - z_j)^q \prod_k \exp(-|z_k|^2/4l_B^2), \tag{2.16}$$

where $z_j = x_j + iy_j$ is the coordinate of the jth electron and l_B is the magnetic length. The derivation of this wavefunction is beyond the scope of this thesis. For the following discussion the precise form of this wavefunction is not important, but what is important here is that from the fact that this wavefunction has to be anti-symmetric under the interchange of two electrons (changing the i and j), it follows that denominator q has to be odd.

Excitations of the correlated electron system at $1/q$ have a finite energy gap and behave like particles carrying $1/q$ of the elementary charge. They have an energy dispersion with a minimum at finite momentum k, called the magneto-roton minimum [16] in analogy to Feynman's theory for superfluid ^{4}He.

In the three-dimensional world, particles have to be either fermions or bosons, meaning that the eigenvalue of the permutation operator P has to be ± 1, since $\hat{P}^2$ has to be the identity-operator. In our case, the quasi-particles are confined to a two-dimensional system, so they have two-dimensional wave-functions. Particles restricted to two dimensions do not do not have to obey either Fermi or Bose statistics and are therefore called anyons. The eigenvalue of $\hat{P}$ can be any phase factor [17]:

$$\hat{P}\Psi(z_1, z_2, z_3, ..., z_N) = \mathrm{e}^{\pm i\theta}\Psi(z_1, z_2, z_3, ..., z_N) \tag{2.17}$$

It has been shown that quasiparticles in the $\nu = 1/q$ state have fractional statistics with angle $\theta = \pm 1/q$. This is linked to the fact that in two dimensions the winding number has to be conserved. Or in other words, if we have two arbitrary paths in a two-dimensional plane, we cannot always transform them into eachother without crossing the origin. In two dimensions the phase difference between such two paths is accounted for by attaching a flux quantum to the corresponding particle. In the case of the FQHE this is a magnetic flux quantum and the electrons with a number of flux quanta attached to it are commonly called composite fermions.

2.4.2 Composite fermion theory

The composite fermion theory is an intuitive way to look at the state of these strongly interacting electrons and was developed by Jainendra Jain [18]. The strongly interacting electrons in a magnetic field B are described as weakly interacting composite fermions in a reduced magnetic field B^* given by

$$B^* = B - 2p\rho\Phi_0, \tag{2.18}$$

where $2p$ is an even integer. This means that the electrons at filling factor ν are described as composite fermions with filling factor ν^* given by

$$\nu = \frac{\nu^*}{2p\nu^* \pm 1} \tag{2.19}$$

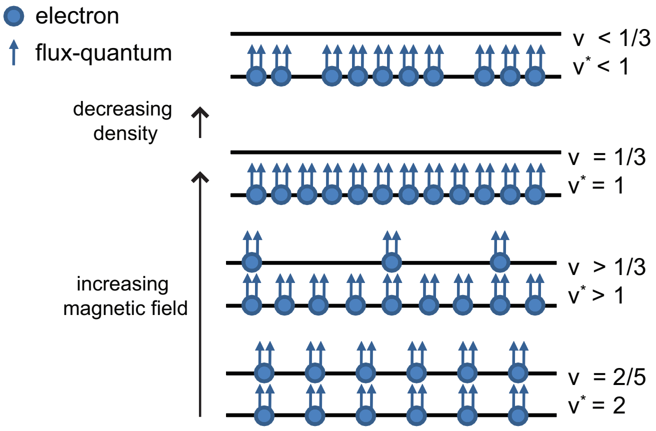

Figure 2.6: *Schematic view of the evolution from $\nu < 1/3$ to $\nu = 2/5$. The distribution of the electrons bound to two flux quanta over the lowest two composite fermion energy levels changes as the filling factor changes. In the lowest three panels the filling factor is changed by changing the magnetic field, so the number of particles is constant. The top panel shows what happens when the density is decreased. Figure after ref. [18].*

The minus sign represents cases where B^* is antiparallel to B. In this description a composite fermion is a bound state of an electron with $2p$ flux quanta. In this picture $\nu = 1/3$ corresponds to $\nu = 1$ for $2p = 2$, so these are composite fermions with two flux quanta $\phi_0 = hc/e$ attached.

In this approach the concept of QEs and QHs can be explained as shown in Figure 2.6. When $\nu < 1/3$ the lowest quasi-Landau level is not completely filled. In this situation there is a QH in the lowest quasi-Landau level. Precisely at $\nu = 1/3$ there are only completely filled or empty levels, whereas for $1/3 < \nu < 2/5$ there are QEs present in the second quasi-Landau level. Note that in this case still the lowest level is completely filled, since by decreasing the magnetic field its degeneracy is reduced. At $\nu = 2/5$, corresponding to $\nu^* = 2$, the lowest two quasi-Landau levels are completely filled.

2.4.3 Photoluminescence spectroscopy in the fractional quantum Hall regime

In Chapter 7 we study the FQHE by means of photoluminescence spectroscopy. In this situation we have, in addition to the correlated 2DEG, a photo-excited valence hole interacting with the 2DEG. A schematic picture of a dispersion relation of the initial and final state is shown in Figure 2.7. The local minimum in the dispersion of the final state corresponds to the magnetoroton minimum.

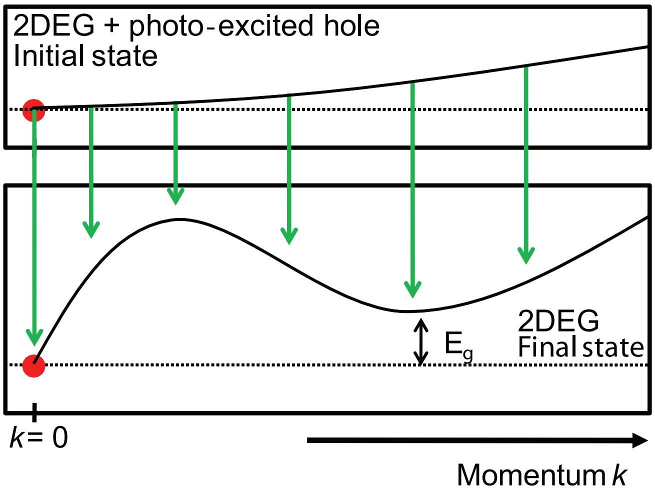

Figure 2.7: *Schematic picture of the dispersion relation of the initial, photo-excited, state and the final state, the correlated 2DEG and the possible optical transitions.*

To connect the anomalies observed in photoluminescence spectroscopy with the interactions in the 2DEG, we have to know the influence of the valence hole on the system. Two limiting cases can be considered: the distance between the electron and hole layers d is zero. This is the case of an infinitely thin quantum well. In the other limit the valence hole is very far away and its effect on the 2DEG can be neglected. In the first situation the interaction between the electrons in the 2DEG and between the electron and the photo-excited hole is equal. Because of this so-called hidden symmetry between electrons and holes only neutral excitons are formed, isolated from the 2DEG. In this limit we will not observe any effects of the correlated 2DEG.

In literature mostly experiments on thin quantum wells have been reported. In Chapter 7 we study the opposite limit, where the valence hole does not disturb the 2DEG. However, since we do observe photoluminescence emission, there is interaction between the hole and the 2DEG. We describe our experimental results in terms of the formalism developed by Quinn and Wójs (for a recent review, ref [19]). The photoluminescence at $\nu = 1/3$ in this case is attributed to the recomination of the photo-excited valence hole with quasi-particles from the 2DEG. Depending on the strength of the electron-hole interaction, emission from excitons, trions (charged excitons) or trions immersed in the 2DEG is expected. In the case of a very weak electron-hole interaction the only optically active and stable states around $\nu = 1/3$ are the fractionally charged excitons h, $h\mathrm{QE}^*$ (the excited state of the dark hQE) and $h\mathrm{QE}_2$ [20].

At $\nu < 1/3$, there are no QEs available, and the spectrum consists of a single line due to the recombination of a hole with an electron in the condensate creating three QHs

$$h \rightarrow 3\mathrm{QH} + \mathrm{photon}. \tag{2.20}$$

Since the photo-excited hole is repelled by the QHs, due to the repulsive Coulomb interaction, complexes of a photo-excited hole with QHs are not stable. At $\nu > 1/3$ QEs exist, since they cannot all be accomodated in their lowest Landau level (which is exactly the case at $\nu = 1/3$, cf. Figure 2.6). These QEs form fractionally charged hole-QE complexes, that recombine via annihilation of QEs and creation of QHs within the condensate:

$$h\mathrm{QE}_n = (3 - n)\mathrm{QH} + \mathrm{photon}. \tag{2.21}$$

In Chapter 7 we will interpret the emission spectra of high quality GaAs/AlGaAs heterojunctions in terms of the above mentioned quasiparticles in the limit of a hole weakly interacting with the 2DEG.

References

[1] Fox, M. *Optical properties of solids.* Oxford University Press, (2001).

[2] Sze, S. and NG, K. K. *Physics of Semiconductor Devices.* John Wiley and Sons, (2007).

[3] Millo, O., Steiner, D., Katz, D., Aharoni, A., Kan, S., Mokari, T., and Banin, U. *Physica E* **26**, 1 (2005).

[4] Okuno, T., Lipovskii, A. A., Ogawa, T., Amagai, I., and Masumoto, Y. *Journal of Luminescence* **87-89**, 491 (2000).

[5] Fock, V. *Z. Phys.* **47**, 446 (1928).

[6] Darwin, C. *Proc. Cambridge Philos. Soc.* **27**, 86 (1930).

[7] Warburton, R. J., Miller, B. T., Dürr, C. S., Bödefeld, C., Karrai, K., Kotthaus, J. P., Medeiros-Ribeiro, G., Petroff, P. M., and Huant, S. *Phys. Rev. B* **58**, 16221 (1998).

[8] Aharonov, Y. and Bohm, D. *Phys. Rev.* **115**, 485 (1959).

[9] Efros, A. L. and Rosen, M. *Ann. Rev. Mater. Sci.* **30**, 475 (2000).

[10] Klimov, V. and editor. *Semiconductor and Metal Nanocrystals.* Marcel Dekker Inc., (2004).

[11] Efros, A. L., Rosen, M., Kuno, M., Nirmal, M., Norris, D., and Bawendi, M. *Phys. Rev. B* **54**, 4843 (1996).

[12] Klitzing, K. v., Dorda, G., and Pepper, M. *Phys. Rev. Lett.* **45**, 494– (1980).

[13] Tsui, D. C., Stormer, H. L., and Gossard, A. C. *Phys. Rev. Lett.* **48**, 1559 (1982).

[14] MacDonald, A. H. and Girvin, S. M. *Phys. Rev. B* **34**, 5639 (1986).

[15] Laughlin, R. B. *Phys. Rev. Lett.* **50**, 1395 (1983).

[16] Girvin, S. M., MacDonald, A. H., and Platzman, P. M. *Phys. Rev. B* **33**, 2481 (1986).

[17] Wilczek, F. *Phys. Rev. Lett.* **49**, 957 (1982).

[18] Jain, J. *Composite Fermions.* Cambridge University Press, (2007).

[19] Quinn, J. J., Wójs, A., Yi, K.-S., and Simion, G. *cond-mat/0906.5182v1* .

[20] Wójs, A. and Quinn, J. J. *Phys. Rev. B* **63**, 045304 (2000).

Chapter 3

Optical techniques in high magnetic fields

Abstract

In this chapter we describe two experimental setups for photoluminescence (PL) spectroscopy in high magnetic fields. The first technique is ensemble PL spectroscopy in pulsed magnetic fields up to 52 T at low temperatures. Timing and triggering play an important role, since the duration of the total magnetic field pulse is less than a second. The setup described in the second part of this chapter enables us to measure spatially dependent time-resolved PL in continuous magnetic fields up to 33 T. We have designed an imaging setup which is minimally sensitive for displacements due to the magnetic field, has a spatial resolution of 0.127 μm and a time resolution of 4 ps.

3.1 Introduction

A setup for photoluminescence (PL) spectroscopy in high magnetic fields for a user facility as the *High Field Magnet Laboratory* (HFML) should be flexible and relatively easy to use under a broad range of experimental conditions. Amongst these experimental conditions are the possibility to measure from mK to room temperature, high spectral and spatial resolution, the highest magnetic fields available, high detection sensitivity and time resolution from picoseconds to microseconds. Obviously not all these requirements can be met with the same setup. In this chapter two different setups are described: 1) a fiber setup to perform ensemble spectroscopy in the highest (pulsed) magnetic fields, at the cost of sensitivity and spatial resolution and 2) an optical imaging setup, which is used to measure spatially resolved time-resolved photoluminescence (TRPL) at temperatures between 1.2 K and 4.2 K in static magnetic fields up to 33 T.

3.2 Photoluminescence in pulsed magnetic fields

3.2.1 The pulsed field facility

The HFML has three sites for pulsed magnets, one of which is equipped with optical fibers allowing for PL spectroscopy. The sites are electrically connected to a capacitor bank and separated from the rest of the building, for safety reasons. Figure 3.1 shows the setup of the coil (a), the cryostat (b) and the electrical connections to the capacitor bank (c). The wire-wound coil is made using copper wire with ZYLON reinforcement and has a bore of 23 mm at 77 K[1]. The coil is cooled by liquid nitrogen and is positioned in a hole in the ground for safety reasons. The home-made liquid-helium cryostat is placed on top.

The energy to operate the coil is drawn from a 2 MJ capacitor bank, which can be charged up to 16 kV. It consists of 60 capacitors which are charged by three chargers in parallel. The peak field of the setup used for optical experiments is 52 T. Where the amplitude of the peak can be varied by changing to voltage to which the capacitors are charged, the duration of the pulse can be varied by using different crowbars. These crowbars also limit the dissipation of heat into the coil. The rise time of the longest pulse is 30 ms and its FWHM 65 ms (cf. Figure 3.3). After a 52 T pulse it takes about four hours for the coil to cool down before it can be used again up to full field.

---

[1] Since the coil is immersed into liquid nitrogen, experiments at room temperature require a anti-cryostat. This reduces the effective bore available for experiments.

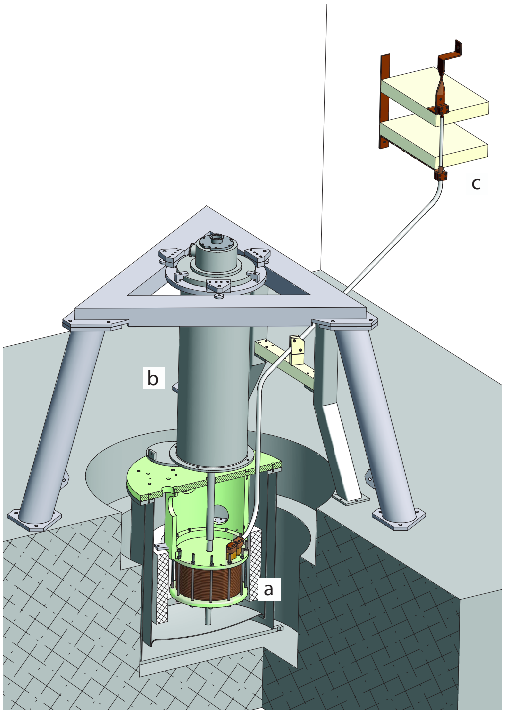

Figure 3.1: *Schematic illustration of the 52 T pulsed magnet with cryostat. (a) Wire would coil. (b) Home-made LHe cryostat. (c) Connectors to the capacitor bank. Picture by Lijnis Nelemans.*

3.2.2 Photoluminescence setup

For the excitation and detection of the light different laser sources, spectrographs and cameras are available, covering the region from the ultra-violet (UV) light to the near infrared (NIR). Both the excitation and detection are guided through 550 μm multimode fibers (Thorlabs FG550LEC and BFH22-550 for the VIS-NIR and UV-VIS region respectively). The probe used to guide the light into the center of the magnetic field is shown in Figure 3.2. The probe is mainly made from glass fiber and hysol and no metal parts are used, since these would warm up the system during the pulse, due to Eddy currents. Between the fibers and the sample a glass polarizer and plastic retarder plate are positioned, to allow for the excitation and detection of crossed-circularly polarized light (σ^+/σ^- or σ^-/σ^+).

Above the sample, symmetrically with respect to the field center, a pick-up

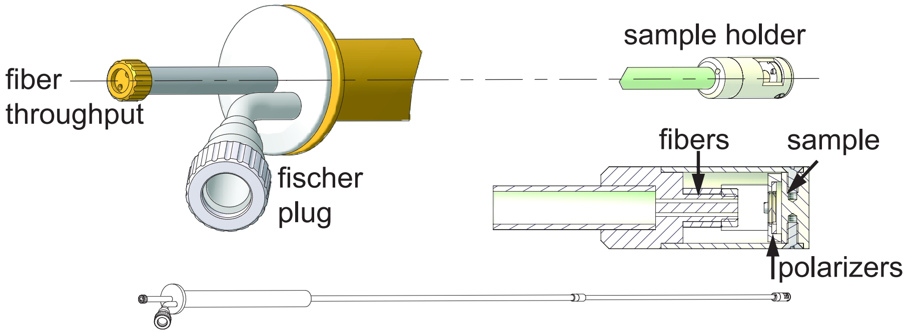

Figure 3.2: *Schematic illustration of the probe for photoluminescence experiments in pulsed magnetic fields. Picture by Lijnis Nelemans.*

coil (not shown) is situated with about ten windings to measure the magnetic field at the sample, which is proportional to the integrated voltage change and the inverse area of the coil:

$$B = \frac{1}{A}\int V\mathrm{d}t \tag{3.1}$$

The pick-up area of the coil is calibrated using a 33 T Bitter magnet and a Hall probe.

To reconstruct the magnetic field at which a given spectrum was taken, the integrated signal of the pick-up coil is compared with the exposures of the camera, as shown in Figure 3.3. The controller of the camera (Princeton Instruments ST-133) has a TTL output which is high during the camera readout and low during the exposure. We know which spectrum corresponds to which time during the pulse by counting the number of times the signal is low. This procedure is necessary since the jitter on the timing sequence of the discharge of the pulsed magnet is an order of magnitude larger than the exposure time needed for one spectrum (≈ 2 ms). This means that we do not know precisely at which time the pulse starts after the discharge command is executed. At the down-sweep, the variation of the magnetic field during one spectrum of 2 ms is about 1 T. As an example, Figure 3.4 shows the photoluminescence spectra of a 25 nm wide GaAs quantum well taken as a function of time during a typical pulse up to $B = 52$ T. Before the pulse the magnetic field is zero; ten spectra are taken before the pulse. During the upsweep the emission peak is strongly broadened due to the changing magnetic field during the exposure. During the downsweep the field changes about 1 T during one exposure.

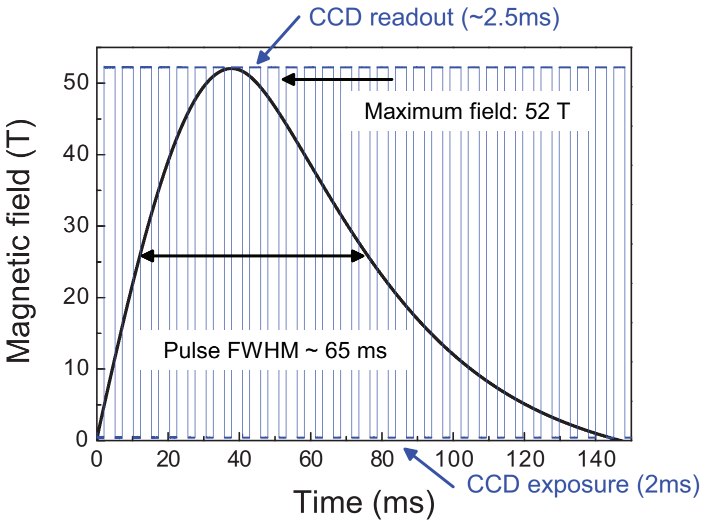

Figure 3.3: *Magnetic field profile of a 52 T pulse and the corresponding scan-signal of the CCD camera.*

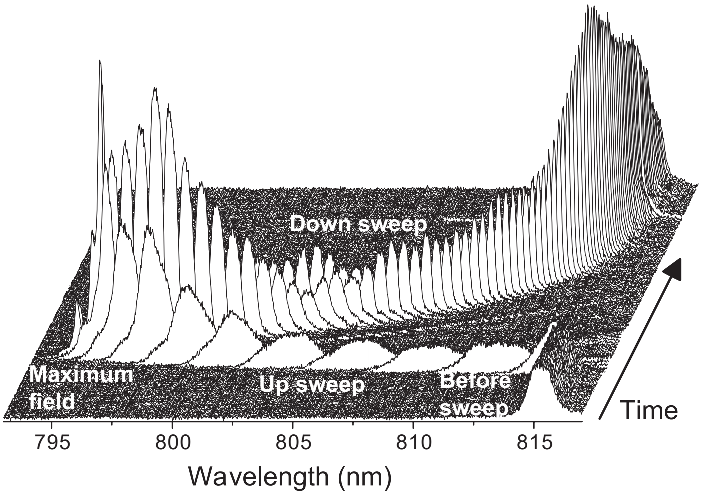

Figure 3.4: *Photoluminescence spectra of a 25 nm wide GaAs quantum well at $T = 4.2\,K$ with 2 ms exposure time. The spectra are shown as function of time.*

3.3 Spatially and time resolved photoluminescence

Most of the optical parts for the setup described in this paragraph are optimized for the spectral region around 800 nm, i.e. around the emission wavelength of GaAs nanostructures. The excitation for the TRPL measurements is provided by a mode-locked picosecond Ti:Sapphire laser (Spectra Physics, Tsunami), providing 2 ps pulses at a repetition rate of 82 MHz and wavelengths between 710 nm and 980 nm. The pulsed laser is pumped by an argon ion laser (Spectra Physics, model 2080). The laser beam is reflected by a broadband hybrid cube beamsplitter (Melles Griot, 03BSC027) and focussed by a 40x objective (Melles Griot) on the sample, which is positioned in the field center of the magnet. The Bitter magnet used for optical experiments provides 33 T and has a room-temperature bore of 32 mm. On top of the magnet is a LHe bath cryostat, which has an inner diameter of 21.6 mm. This diameter limits the outer diameter of the probe we can use to 19 mm, since the latter is mounted in an outer tube which shields the probe from direct contact with the LHe bath.

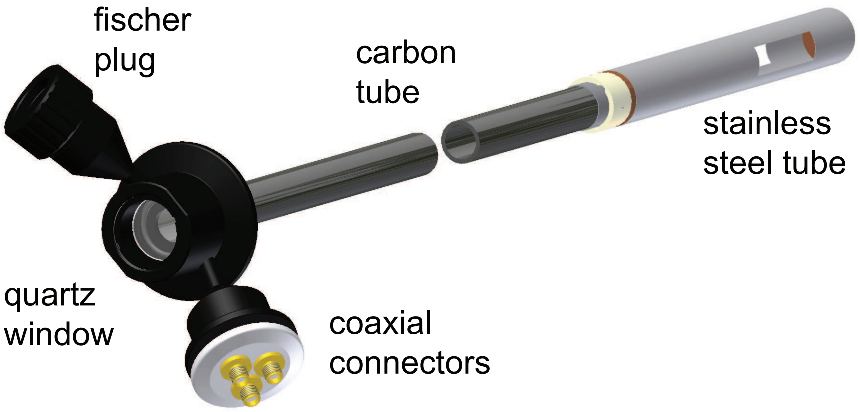

Figure 3.5: *Illustration of the carbon probe for high static magnetic fields and low temperatures. On the carbon tube an objective is screw-mounted. The sample is mounted on piezo-positioners (not shown) and fixed in a stainless steel tube that is connected to the carbon tube. Picture by Lijnis Nelemans.*

The probe we have designed for these measurements, is shown in Figure 3.5. On the left side of Figure 3.5, at the top, there are a vacuum tight quartz window to provide optical access and electrical connections. The probe itself consists of a carbon tube [1], which has the advantages that the material is very strong and rigid, (almost) non-magnetic and that it is black, so it minimizes the background due to scattered light. At the end of the carbon tube the objective is screw-fixed. The bottom part of the probe (cf. right side of Figure 3.5) where the sample and nanopositioners (Attocube ANP50 series [2]) are mounted, is made from stainless steel. This part can be slid onto the carbon tube and be fixed with screws.

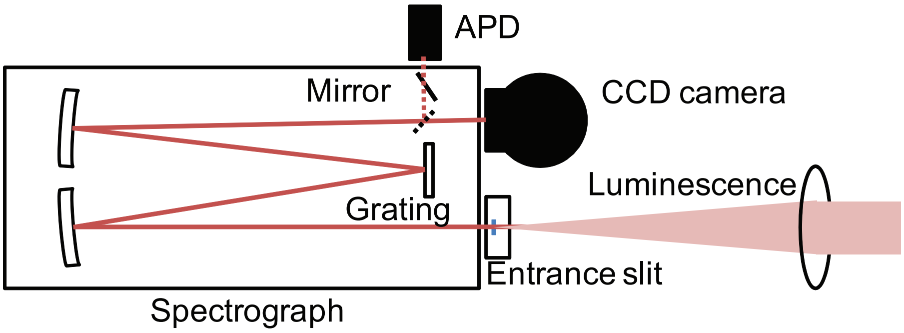

Figure 3.6: *Schematic representation of the detection part of the spatially resolved TRPL setup. The (polarized) luminescence is collected by a 40x Melles Griot objective and imaged by a lens with $f = 1000$ mm on the entrance slit of an imaging spectrograph (Jobin Yvon HR640). The light is dispersed by a 1200 g/mm grating and for spatially resolved PL focused onto a back-illuminated LN-cooled CCD camera with pixels of 24 μm. The system has a spatial resolution of 0.127 μm and a spectral resolution of approximately 0.05 meV around 1.6 eV. For TRPL the light is focused on an with a time resolution of 4 ps and a 50 μm chip, giving a spatial resolution of 0.265 μm. The time traces are recorded by a time-correlated single photon counting system.*

The PL from the sample is collected by the same objective used for the excitation, transmitted by the beamsplitter and focussed on the entrance slit of an imaging spectrograph (Jobin Yvon HR640, 1200 g/mm grating) by a $f = 1000$ mm lens, as shown in Figure 3.6. Optionally the circular polarization of the light can be selected by placing an achromatic retarder (B.Halle Achromatic Quartz and MgF_2 Retarder) and Glan-Taylor polarizer (Melles Griot) in the detection path. The spectrograph we use has two exits, on one of which a liquid-nitrogen cooled CCD camera with a square 512x512 pixel chip (Princeton Instruments TEK512x512DB) is positioned. On the other exit an avalanche photon detector (APD; MPD PD5CTC) is positioned, with a time resolution of 4 ps and a 50 μm chip. With a mirror inside the spectrograph one of the two exits can be selected.

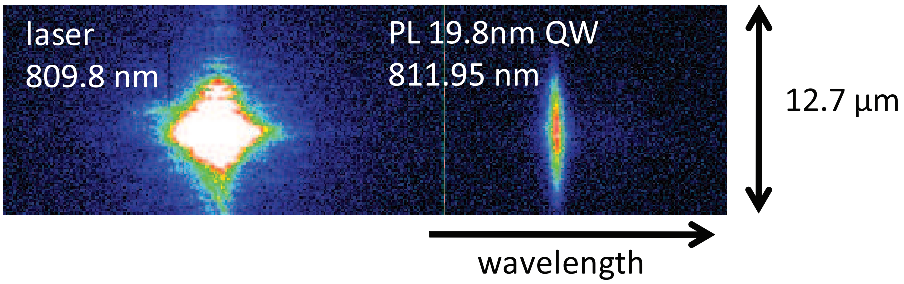

Figure 3.7: *Spatially and spectrally resolved image of a 19.8 nm wide GaAs/AlGaAs quantum well at 4.2 K. At the left there is the spot of excitation and on the right the luminescence of the quantum well.*

With the CCD camera we can make a spatially and spectrally resolved image of the PL, as shown in Figure 3.7 for a 19.8 nm wide GaAs/AlGaAs quantum well [3]. The quantum well is mounted such that confinement direction of the quantum well ($z = 19.8\,\text{nm}$) is mounted perpendicular to the light an the magnetic field. Along the axis of the chip parallel to the entrance slit of the spectrograph the spatial profile is recorded, giving information how far the excitons travel in the quantum well plane before they recombine. Along the other axis the spectral information is recorded.

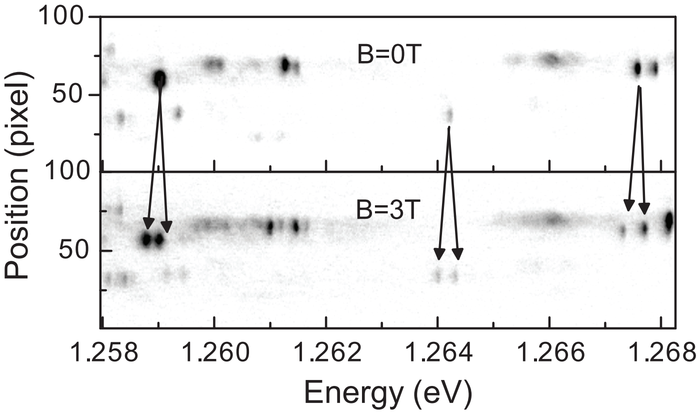

Figure 3.8: *Photoluminescence image of single self-assembled InAs/GaAs quantum rings at* $T = 4.2\,\text{K}$. $B = 0$ *T (upper panel);* $B = 3$ *T (lower panel).*

We can also use this method to measure isolated nanostructures, such as the single quantum rings discussed in Chapter 5. The advantage in this case is that we are able to measure the emission of multiple objects in a single run, since they are both spatially and spectrally separated. This differs from for example a fiber-setup, where it is not possible to spatially separate the signal from individual objects. An example of an image of single self-assembled InAs/GaAs rings is shown in Figure 3.8 at $T = 4.2\,\mathrm{K}$ and $B = 0\,\mathrm{T}$ (upper panel) and $B = 3\,\mathrm{T}$ (lower panel). For three dots the Zeeman spin splitting is indicated by arrows.

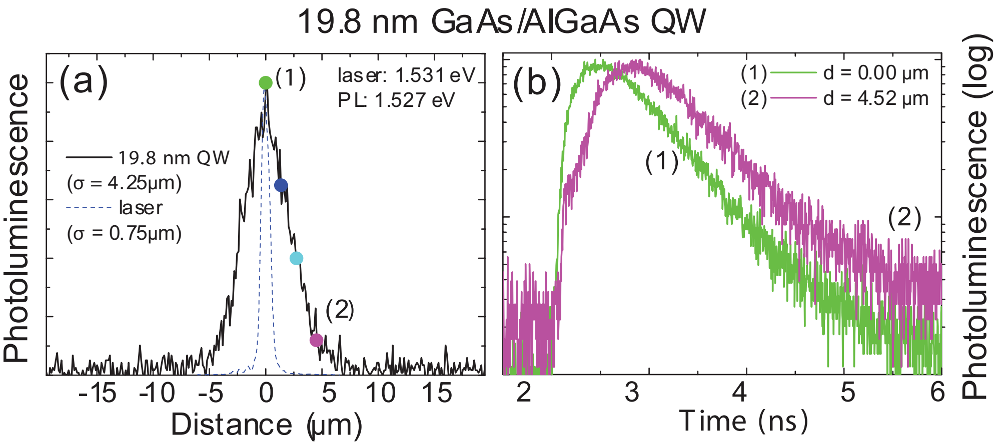

Figure 3.9: *Spatially resolved TRPL of a 19.8 nm wide GaAs/AlGaAs QW at $T = 4.2\,\mathrm{K}$. (a) Cross section of a PL image at 1.531 eV (laser) and 1.527 eV (quantum well PL). The spatial extension is determined by a Gaussian fit. (b) Time resolved spectrum at two points in the image.*

Figure 3.9a shows a cross section of the image of Figure 3.7 at the laser energy and the PL energy. The intensity of each peak is normalized by its maximum intensity. The widths of the peaks are obtained by a gaussian fit. We find a width of the laser peak $\sigma = 0.75\,\mu\mathrm{m}$. This width is not the actual laser width, but the response of the system to an infinitely narrow peak, i.e. the experimental accuracy. The spatial extent of the PL of the QW ($\sigma = 4.25\,\mu\mathrm{m}$) is much larger than that of the laser. This implies that the photo-excited excitons travel a certain distance in the plane of the quantum well before they decay radiatively. The speed at which the excitons travel can be extracted by combining the spatial information with the timetraces shown in Figure 3.9b. As can be clearly seen in Figure 3.9b the rise time of the curve taken at $d = 0.00\,\mu\mathrm{m}$

is much shorter than the rise time of the curve taken at $d = 4.52\,\mu$m. A quantitative analysis of these data is beyond the scope of this thesis, but at least we can conclude the exciton transport is not instantaneous.

References

[1] `www.wolkenstuermer.de`.

[2] `www.attocube.com`.

[3] Pullizi, F. *Imaging the Motion of Exitonic Complexes in Semiconductor Quantum Wells.* PhD thesis, Katholieke Universiteit Nijmegen, (2003).

Chapter 4

Energy levels and structural characterization of InAs quantum dots

Abstract

We have measured the energy levels and charging spectra of holes in self-assembled InAs quantum dots using capacitance-voltage (C-V) and polarized photoluminescence (PL) spectroscopy. The magnetic field dependence of the single-particle hole energy levels can be understood by considering a spin-orbit coupled valence-band and agrees well with the observed behavior of the charging spectra. Furthermore, we report a detailed structural characterization of the same dots based on cross-sectional scanning tunneling microscopy experiments on 13 individual quantum dots, which reveal an ellipsoidal dot shape with an average height of 8 nm and a 26 nm diameter. The dots consist of an InGaAs alloy with a profound gradient in the indium concentration in both horizontal and vertical directions. Finally, samples of InAs quantum dots grown on a template are investigated in pulsed magnetic fields up to 42 T by means of polarized PL spectroscopy. The emission of these laterally coupled quantum dots changes significantly in high magnetic fields and the behavior of the PL energy, width and polarization is discussed.

This work is based on:
J. H. Blokland et al. Phys. Rev. B **75**, 233305 (2007)
J. H. Blokland et al. Appl. Phys. Lett. **94**, 023107 (2009)

4.1 Introduction

Three-dimensional spatial confinement in semiconductor quantum dots (QDs) leads to discrete energy levels that can be filled consecutively by charge carriers [1]. To fully exploit the properties of QDs for advanced applications [2,3] it is important to understand their energetic shell structure and charging sequence. To date mainly electron systems were investigated, both in lithographically-defined [4] as well as in self-assembled QDs [5–7]. It was found that charging QDs resembles shell filling (*s, p, d, ...*) in atoms, whilst describing the lateral confining QD potential by a two-dimensional (2D) harmonic oscillator and treating the interactions between electrons as a perturbation [4,6]. In this chapter we investigate self-assembled InAs QDs filled with *holes* that exhibit a different behavior [8–12]. The main difference arises from the complicated valence band structure, which is governed by multiple, spin-orbit coupled bands [12–14], rather than the single band for electrons. Furthermore, for holes the quantization energy is comparable to the Coulomb-interaction energies, which can, therefore, no longer be treated as a perturbation. These aspects make the energy structure and charging sequence of hole systems interesting from a fundamental point of view to explore novel carrier configurations that defy rules of atomic systems [8, 10, 11]. In addition, knowledge of the hole energy levels is crucial for the optical properties of QDs, [15–20] originating from electron-hole recombination.

The energy levels and physical properties of QDs strongly depend on their actual dimensions and composition. It is therefore important to investigate this structure-property relationship. In many studies on epitaxial QDs, however, there is only limited information on their structure [6, 17, 21, 22], and in order to describe those experiments an idealized QD shape and composition had to be assumed. This lack of information hinders a thorough interpretation of experimental results and limits the applicability of theoretical calculations [23–25]. Recent progress in advanced structural characterization techniques has made it possible to determine shape and composition of In(Ga)As QDs, demonstrating a large variety in shape: lens-shaped dots found by tunneling electron microscopy [26, 27], pyramid-shaped dots by cross-sectional scanning tunneling microscopy (X-STM) [28] and more complicated faceted shapes by STM [29]. A major advantage of X-STM is that it is able to characterize QDs embedded in matrix, which can be substantially different from those at the sample surface, as measured by atomic-force microscopy and STM [30]. Indeed, X-STM experiments on embedded InAs QDs [31] and quantum rings [32] have shown that their actual electronic properties could only be explained by the unexpected geometry and composition of the nano-objects.

In the following two sections we will describe the hole energy level structure of InAs QDs and a full structural characterization of the same dots. We have used samples from the same wafer to perform both type of experiments.

4.2 Energy levels of holes in InAs quantum dots

4.2.1 Introduction

To identify the QD energy levels we use capacitance-voltage (C-V) and polarized photoluminescence (PL) spectroscopy in high magnetic fields (B). Previously, high field energy spectra of electron [4, 6] and exciton [6, 17, 33] systems were analyzed within the Fock-Darwin (FD) model [34, 35], i.e. a 2D harmonic oscillator in a perpendicular magnetic field. Using this description recent C-V experiments on p-type InAs QDs have suggested an incomplete shell filling, which means that the d-shell starts filling before the p-shell is full [8, 36]. A different, yet similar, anomalous filling due to hole correlation effects was found theoretically by He *et al.* [10, 11], using an atomistic pseudopotential approach. An alternative explanation was given by Climente *et al.* [12] in terms of the single-particle hole levels.

Contrary to previous magneto-PL experiments on QDs [17, 20] we explore the circular polarization of the PL emission. By using the optical selection rules we determine the angular momentum of the confined electron and hole energy levels. We find that, unlike the electron levels, the hole levels cannot be described within the FD model, but require a description that takes into account the spin-orbit coupling of the valence band [12]. The resulting hole energy level diagram is consistent with the C-V charging experiments on the same sample, without the need to invoke anomalous filling due to hole correlation effects.

4.2.2 Experimental details

The p-type InAs QD sample was grown by solid source molecular beam epitaxy on an undoped GaAs(100) substrate and details of the growth can be found elsewhere [8, 9, 37]. The layer sequence is 300 nm carbon doped GaAs (back-contact), 19 nm undoped GaAs (tunneling barrier), an InAs QD layer (0.2 nm InAs islands followed by 8 nm GaAs overgrowth), 22 nm GaAs, an AlAs/GaAs superlattice ($32 \times 3\,\text{nm}$ AlAs/1 nm GaAs) and a 10 nm GaAs cap layer. Under the growth conditions used [8] QDs with $\sim 20\,\text{nm}$ diameter and $\sim 3\,\text{nm}$ height are formed with a density of $\sim 10^9\,\text{cm}^{-2}$.

From the samples optically accessible Schottky diodes were prepared with semitransparant $300 \times 300\,\mu\text{m}^2$ ITO top gates. A Schottky diode is a device in which a Schottky barrier is formed, which occurs when a metal is brought in contact with a semiconductor. The band structure of the Schottky diode with quantum dots is given in Figure 4.1. Without the application of a gate voltage, the energy diagram of the valence band of the Schottky barrier is given by Figure 4.1c.

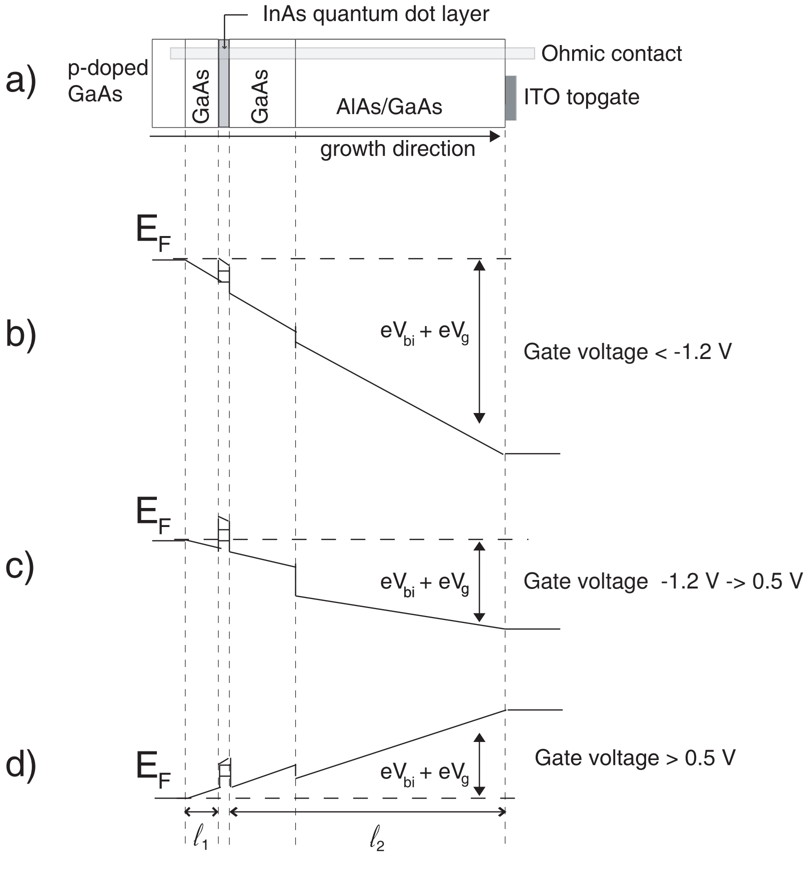

Figure 4.1: *Sample layout of the Schottky diode for different gate voltage regions. The hole energy levels in the quantum dot layer are indicated by the horizontal lines.*

On the left side of the diagram the Fermi energy is determined by the *p*-doped GaAs, on the right side it is determined by the Fermi energy of the metal. Because the Fermi energy has to be the same through the whole structure, the valence band is bent in the way shown in Figure 4.1c. By applying a negative gate voltage, the bending of the valence band is enhanced (Figure 4.1b); by applying a positive gate voltage, the bending is decreased (Figure 4.1d). When a dot level is in resonance with the Fermi level, the holes can tunnel into the dot. This tunneling is seen as an increase in the capacitance, a so-called charging peak. For gate voltages below -1.2 V, the bending of the valence band is such that the dot's energy levels are all below the Fermi level, and the dot is empty. Above 0.5 V the holes can tunnel into the two-dimensional wetting layer, which has a continuous energy structure, and a rapid increase in capacitance is observed.

C-V and polarized PL experiments were performed on the same gate at 4.2 K using a standard capacitance bridge (Andeen-Hagerling AH2500) and a standard PL setup (Ti-Sapph. laser excitation (spot size $\sim 10\mu$m), single grating spectrometer, LN-cooled InGaAs detector) respectively.

4.2.3 Experimental results

The optimized growth procedure resulted in sufficiently small inhomogeneous level broadening to enable the observation of individual charging peaks in C-V and narrow, well-separated PL peaks in ensemble measurements [37]. Figure 4.2 shows typical C-V traces (a) and PL spectra (b) recorded for magnetic fields up to 28 T, applied parallel to the growth direction. A linear background was subtracted from each C-V curve to obtain the capacitance signal of the QDs. The signal exhibits six clear charging peaks, each of which corresponds to the charging of one additional hole per QD. With increasing magnetic field each charging peak displays a characteristic shift. These shifts in voltage ΔV_g are transformed to shifts in energy ΔE by the usual lever arm law:

$$\Delta E = \lambda^{-1} e \Delta V_g, \qquad (4.1)$$

where λ^{-1} is the ratio between the thickness of the tunneling barrier (19 nm) and the distance between the back-contact and the surface (168 nm) [6, 9].

This analysis reveals a behavior that was also found in previous C-V measurements on a similar sample [8]. Peaks 1 and 2 exhibit an opposite, but small shift (± 0.02 meV/T). At low fields ($<$ 12 T) peaks 3 and 5 (4 and 6) shift to lower (higher) fields, while the slopes of peaks 5 and 6 (± 0.38 meV/T) are twice those of peaks 3 and 4 (± 0.20 meV/T). Above 12 T the shifting direction of peaks 4, 5 and 6 is reversed. Within the FD model these shifts are directly related to the orbital angular momentum quantum number l, which would indicate that peaks 1 and 2 are s-like ($l = 0$), 3 and 4 are p-like ($l = 1$) and 5 and 6 are d-like ($l = 2$). These results suggest that the d-shell starts filling before the p-shell is completely full, in contrast to the rules of sequential filling in atomic physics.

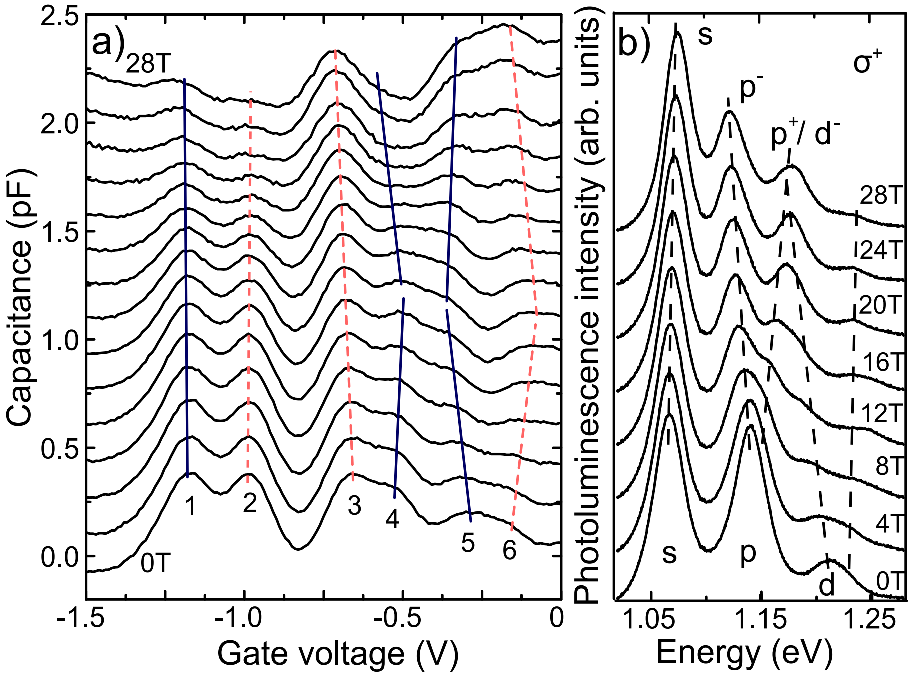

Figure 4.2: *(a) C-V traces at T = 4.2 K for p-type InAs QDs in magnetic fields from 0 to 28 T (2 T steps). The curves are vertically offset for clarity and the lines are calculated using the model for hole filling outlined in the text. (b) Magnetic field dependent σ^+-polarized PL spectra of the QD ensemble (λ_{exc} = 734.8 nm, T = 4.2 K, V_g = 0.0 V, $P_{\mathrm{exc}} \sim$ 50 Wcm^{-2}). The dashed lines are a guide to the eye.*

In PL we observe three peaks, which are related to s-, p- and d- electron-hole transitions. To further characterize the relevant QD energy levels we follow these peaks as a function of magnetic field, for two circular polarizations ($\sigma^{\pm}$) and several photo-excited carrier densities (Figures 4.2b, 4.3). In σ^+-polarization the s-peak shifts slightly to higher energies, the p-peak splits into two separate peaks, one of which crosses a d-peak that shifts to lower energies (Figure 4.2b). The s-, p- and d-levels can be consecutively populated with increasing carrier density, realized via variation of both laser excitation power P_{exc} and wavelength λ_{exc}. When the excitation energy is lower than the GaAs energy gap (Figure 4.3a) carriers are only excited in the QDs and wetting layer, leading to a relatively low carrier density and only s-level recombination. With an excitation energy higher than the GaAs bandgap, carriers are excited

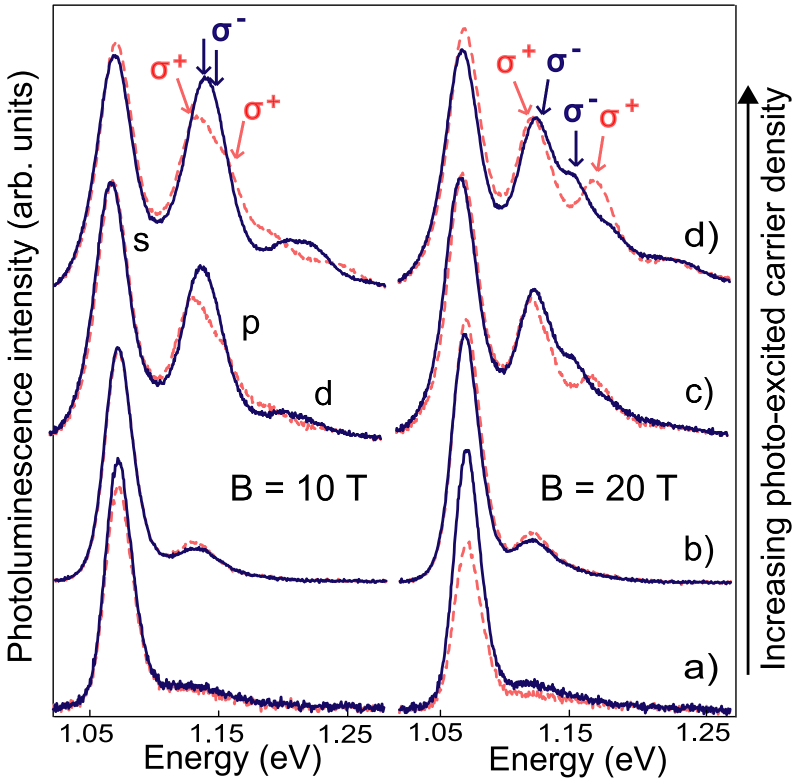

Figure 4.3: *Circularly polarized PL spectra of InAs QDs for different photo-excited carrier densities at* B = 10 *T and* B = 20 *T (*T = 4.2 *K,* V_g *=0.0 V).* $\lambda_{\rm exc}$ *and* $P_{\rm exc}$ *are 831.0* nm *and* ∼ 10 *W*cm^{-2} *for (a), 809.1* nm *and* ∼ 50 *W*cm^{-2} *for (b), 734.8* nm *and* ∼ 50 *W*cm^{-2} *for (c) and 734.8* nm *and* ∼ 80 *W*cm^{-2} *for (d).*

throughout the GaAs barrier layers and are subsequently captured by the QDs, leading to emission from *p*- and *d*-states as well (Figure 4.3b-d). Within the resolution of our ensemble measurements the PL peak positions were found to be independent of the photo-excited carrier density [16]. Surprisingly, our experiments are insensitive to hole charging effects, since we did not observe a change in the relative energy distances between PL transitions with gate voltage (the number of holes per dot), despite small shifts of the spectra as a whole due to charge accumulation in the structure.

A possible reason is the slow hole tunneling through the 19 nm barrier compared to the carrier relaxation and recombination times (∼ns), which means

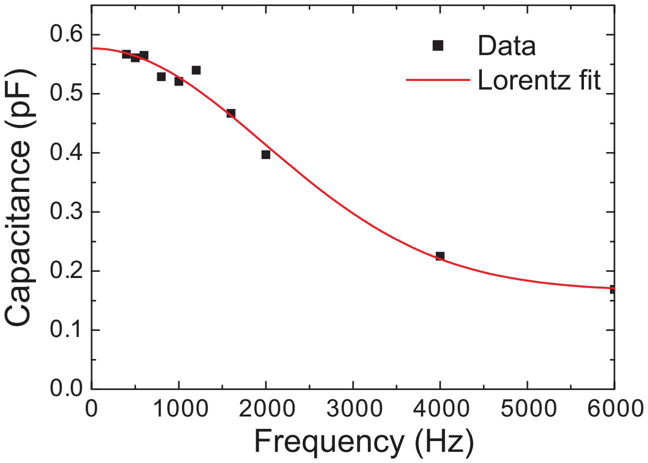

Figure 4.4: *Frequency dependent capacitance for the first s-peak. The solid line is a Lorentz fit through the data to obtain the tunneling time.*

that an average over different charge states is measured, on top of the average over different dot dimensions.

The thickness of the tunneling barrier (l_1) affects the tunneling time of the holes. To quantify the dependence of the tunneling time, the WKB approximation with a triangular tunneling barrier can be used [9]. The tunneling time τ is inversly proportional to the tunneling coefficient T^2, which is in the WKB approximation given by

$$T^2 = \exp\left(\frac{-4l_1}{3\hbar}\sqrt{2m_h^* E}\right) \tag{4.2}$$

where E is the barrier height and m^* the effective hole mass in the barrier.

The tunneling time is determined from frequency dependent C-V measurements, shown in Figure 4.4 for the first s-peak. From the frequency dependent capacitance we extract the tunneling time τ, by fitting the data with the following curve:

$$C(f) = \frac{N}{1 + (1\pi\tau f)^2}, \tag{4.3}$$

where $C(f)$ is the frequency dependent capacity and N is a normalization factor. We find for the first s-peak a tunneling time $\tau = 80 \pm 3\,\mu$s.

Important information is revealed by the pronounced circular polarization of the PL peaks, visible in the spectra at high carrier densities (Figure 4.3c,d). The s-peak splits up in two, oppositely polarized, closely-spaced, peaks. The p-transition splits up in four lines with a characteristic sequence of, with increasing energy, $\sigma^+, \sigma^-, \sigma^-, \sigma^+$ peaks, indicated by arrows in Figure 4.3d.

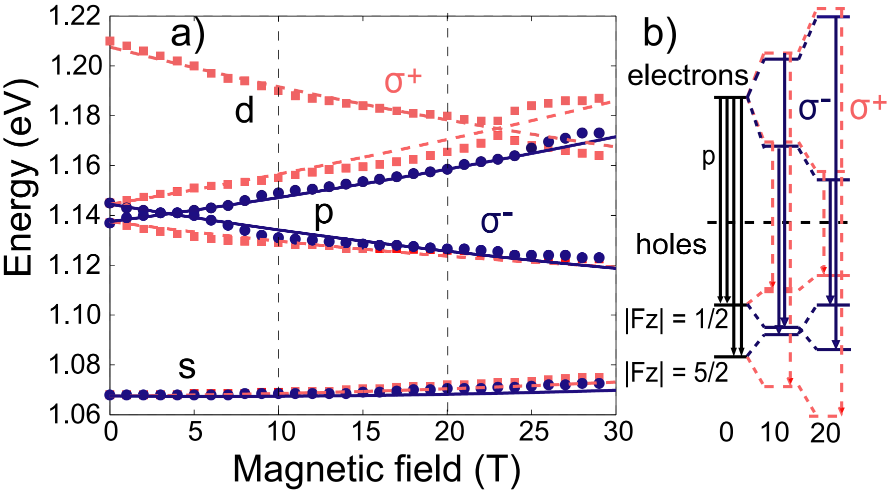

Figure 4.5: *(a) Exciton recombination energies (symbols) in magnetic fields up to 29 T (4.2 K $V_g = 0.0$ V, $\lambda_{\mathrm{exc}} = 734.8$ nm, P_{exc}=50 Wcm^{-2}). The symbol size corresponds to the uncertainty in the energy position (2 meV). The lines are fits of the exciton energies as outlined in the text. (b) Electron and hole p-levels at B=0,10,20 T. The arrows indicate the optically allowed polarized transitions. The polarization of the peaks ($\sigma^+, \sigma^-, \sigma^-, \sigma^+$) in order of increasing energy is in agreement with the observations.*

The PL spectra were fitted by Gaussian peaks of 26 meV width (Full- Width-at-Half-Maximum), resulting in the fan diagram shown in Figure 4.5a. PL series taken at different carrier densities and gate voltages, resulted in similar diagrams. The fan diagram resembles the behavior of excitons within the FD model [17, 33], which assumes FD spectra for both carrier types. However, the splitting of the p-levels at $B = 0$ T and the sequence of polarized peaks, already indicate that this is an oversimplification, since the FD model predicts no splitting, and an sequence of alternating polarized peaks. To obtain the underlying single-particle levels, we disentangle the electron and hole contributions to the PL energy. For electrons we take the FD energies [34, 35]:

$$E_{l,m_z} = \hbar(l+1)\sqrt{\omega^2 + \left(\frac{\omega_c}{2}\right)^2} + \frac{1}{2}\hbar m_z \omega_c + g S_z \mu_B B,$$

where $\omega_c = eB/m^*$ is the cyclotron frequency, e is the electron charge, m^* is the electron effective mass, g is the Landé factor and μ_B is the Bohrmagneton. ω defines the energy scale due to the lateral confinement and $S_z = \pm 1/2$ is the z-component of the electron spin. The energy levels are further labeled by their quantum numbers, the orbital quantum number l ($l = 0, 1, 2$ for the s, p, d-shell respectively) and its z-projection $m_z = -l, -l+2, ..., l-2, l$. We use $\hbar\omega = 55$ meV, $m^* = 0.077 m_0$ (m_0 is free electron mass) and g=1.2, which are reasonable values considering previous experiments [6, 15, 38–40].

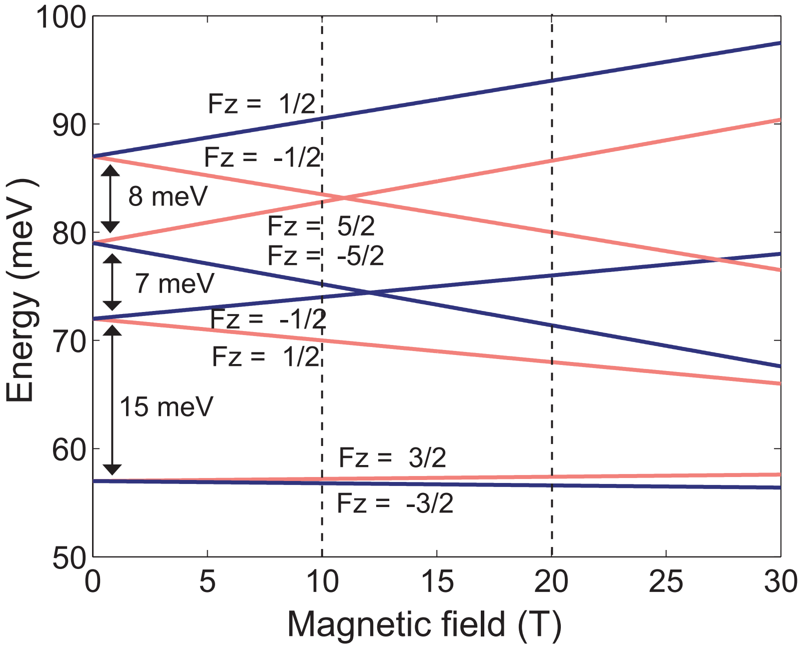

Figure 4.6: *Single-particle hole energy levels in magnetic field as obtained from the PL-spectra. The shifts (in order of increasing energy) are* ±0.02, ±0.20, ±0.38 *and* ±0.35 *meV/T.*

The shifts of the PL lines with field are mainly governed by the FD spectrum of electrons. However, since the electron Zeeman splitting is small, the PL polarization is predominantly determined by the hole levels, as is explained in the following. Due to spin-orbit coupling within the valence band, the effect

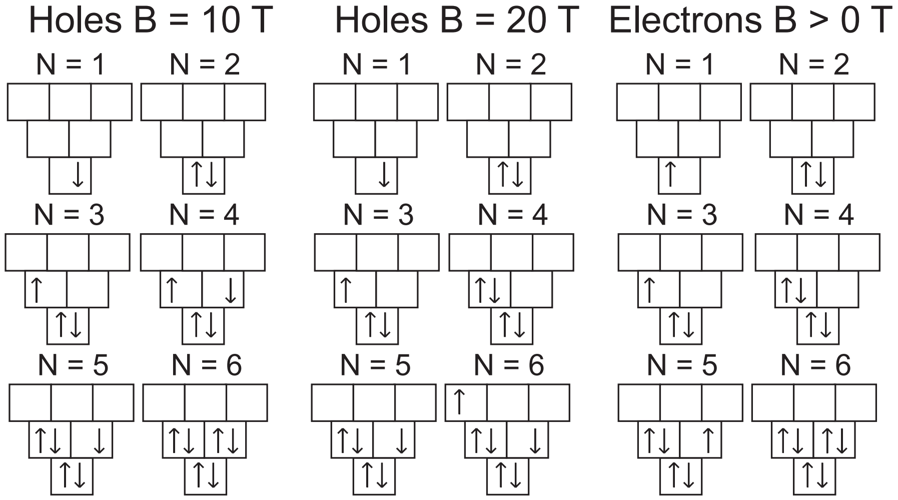

Figure 4.7: *Filling sequence for electrons and holes up to $N = 6$. The arrows up (down) correspond to $J_z = 3/2$ ($J_z = -3/2$) for holes and $S_z = 1/2$ ($S_z = -1/2$) for electrons.*

of which is enhanced due to the lateral confinement [13, 14], m_z and S_z are no longer proper quantum numbers for holes. It is convenient to define the quantum number $F_z = J_z + m_z$, the sum of the z-projection of the Bloch angular momentum J_z ($J_z = \pm 3/2, \pm 1/2$ for heavy and light holes respectively) and m_z [12]. For each F_z different combinations of J_z and m_z are possible. As a result of the particular mixture of these combinations, the magnetic field dependence of the energy levels differs strongly from that of a FD model for holes. The effect on the PL polarization is most clearly seen in the behavior of the p-states, schematically shown in Figure 4.5(b) for $B = 0, 10$ and 20 T. The p-like hole levels, labeled by $|F_z|$= 1/2 and 5/2, with a small zero-field splitting due to the coupled valence bands, split up in a field, leading to a characteristic emission pattern as a result of the optical selection rules: $\Delta m_z = 0$ and spin conservation $S_z + J_z = \pm 1$. To determine the allowed transitions we use only the dominant m_z contribution of each F_z level. For example, the main contribution to the F_z= 1/2 (5/2) p-like levels comes from J_z= 3/2; m_z = -1 (+1) which both recombine in σ^+ polarization. In contrast, the F_z= -1/2 (-5/2) p-levels (J_z= -3/2; m_z = +1 (-1)) give σ^- emission. The resulting polarization series with increasing energy is indeed $\sigma^+, \sigma^-, \sigma^-, \sigma^+$ in the 5-25 T field range, as observed experimentally (Figure 4.5). In fact, using this model, we are able to quantitatively describe the field dependent exciton energies (lines in Figure 4.5a). An additional energy $E = 1.0125\,\mathrm{eV}$ was used to account for the energy gap of InAs, the z-confinement energy and the exciton binding energy [41]. From this fit we find hole levels that shift with magnetic field in an approximately linear fashion (Figure 4.6) [12]. The difference in shift of the F_z=1/2 and F_z=5/2 p-like levels is due to the specific mixture of m_z contributions to these levels.

Remarkably, the field dependence of the single-particle hole levels determined by PL agrees very well with the C-V data (see lines in Figure 4.2a). Adding a constant Coulomb blockade energy of 18 meV to the zero-field splitting results in the proper spacing between the different charging peaks. The field induced shifts in energy of the C-V charging peaks are nicely reproduced. Finally, the cusps in the shifting direction of peaks 4, 5 and 6 around 12 T naturally follow from crossings of hole levels. For example, peaks 4 and 5 change shifting direction when the $F_z = -1/2$ and $F_z = -5/2$ p-like levels cross. Below (above) this field the fourth hole occupies the $F_z = -1/2$ ($F_z = -5/2$) p-like state (Figure 4.7). Likewise, peak 6 changes slope when the $F_z = 5/2$ p-like level crosses the $F_z = -1/2$ d-like level.

Our final level diagram as shown in Figure 4.6) qualitatively agrees with recent bandstructure calculations of hole levels in InAs QDs [12]. In particular, hole-charging effects do not have to be invoked for a satisfactory explanation of the magnetic field dispersion of energy levels for both a non-interaction system as measured with PL as well as for the charging spectra deduced from C-V spectroscopy. However, other recent theoretical calculations, using an atomistic pseudopotential description, propose a different filling sequence of the hole levels. [10, 11] Because of the competition between Coulomb repulsion and level spacing the d-like shell starts filling before the p-like shell is fully occupied. In terms of the hole levels in Figure 4.6) this implies that the d-like $|F_z| = 1/2$ levels energetically move below the p-like $|F_z| = 5/2$ levels at zero magnetic field. Since the magnetic field dispersion of these levels is very similar such a reversed level sequence is still consistent with our experimental results for an interacting system as measured by C-V spectroscopy.

4.2.4 Conclusion

By combining optical and C-V spectroscopy experiments in high magnetic fields we determine the single-particle levels and charging energies of holes in self-assembled InAs QDs . Our analysis of the PL polarization shows that, unlike electrons, holes do not follow the Fock Darwin spectrum, and underlines the crucial role of the complex valence-band structure for the properties of semiconductor QDs. The resulting model for the single-particle hole levels is consistent the charging spectra obtained from C-V spectroscopy.

4.3 Structural characterization of InAs quantum dots

4.3.1 Introduction

To determine the size and dimensions of the QDs, we present X-STM measurements on the p-type InAs QDs. We find an unprecedented ellipsoidal shape with a large indium gradient in both vertical and horizontal directions. This result can be used as input for realistic models to better understand the charging characteristics and optical properties of semiconductor QDs.

4.3.2 Experimental details

The sample used is identical to the sample described in the previous section. The relatively narrow PL lines and the observation of individual charging peaks evidence the large uniformity of the QDs. We estimate an inhomogeneous size distribution of only 5%. X-STM measurements have been conducted at room temperature in an ultra high vacuum chamber ($p < 4 \cdot 10^{-11}$ Torr) on the (in-situ cleaved) [011] cross-sectional surface. Polycrystalline tungsten tips prepared by electrochemical etching have been used. The images have been taken at high voltage ($\sim 3.0\,\mathrm{V}$) to suppress the electronic contrast and to enhance the topographic contrast due to the outward relaxation [42]. After cleavage of the sample, the indium-rich regions relax out of the GaAs matrix due to the strain caused by the 7% lattice constant mismatch between GaAs and InAs. Determining the outward relaxation thus provides a measure for the local indium content inside the dot.

4.3.3 Experimental results

We have investigated 13 individual QDs originating from a piece of the wafer next to the part that has been used for PL and CV measurements [43]. A representative topography image is shown in Figure 4.8 (after Fourier filtering to highlight the atomic layers) and 4.11b (as measured). These images represent the QD with the largest measured height of $8.1 \pm 0.4\,\mathrm{nm}$ with a diameter of $27.5 \pm 4\,\mathrm{nm}$. These X-STM images reveal that the shape of the dot can be best described by an ellipsoid, as is further demonstrated below.

Figure 4.9 shows the height-base diameter distribution for all 13 dots, where the tallest dot (Figure 4.8) corresponds to the encircled data point. The height-base diameter statistics contains important information on the average shape

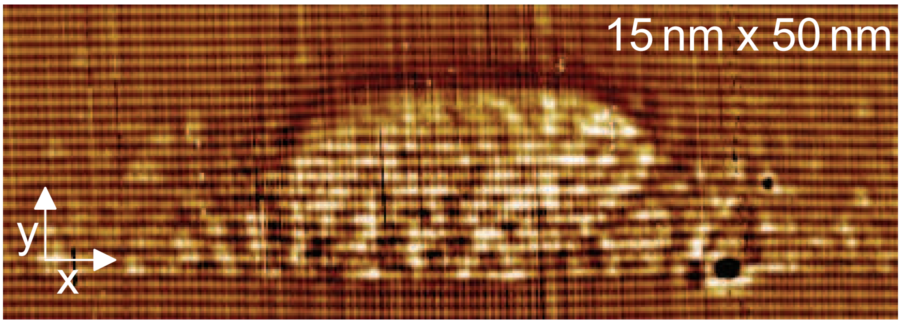

Figure 4.8: *Fourier filtered topography image taken by X-STM of a representative QD assumed to be cleaved through its middle plane. This dot corresponds to the encircled data point in Figure 4.9.*

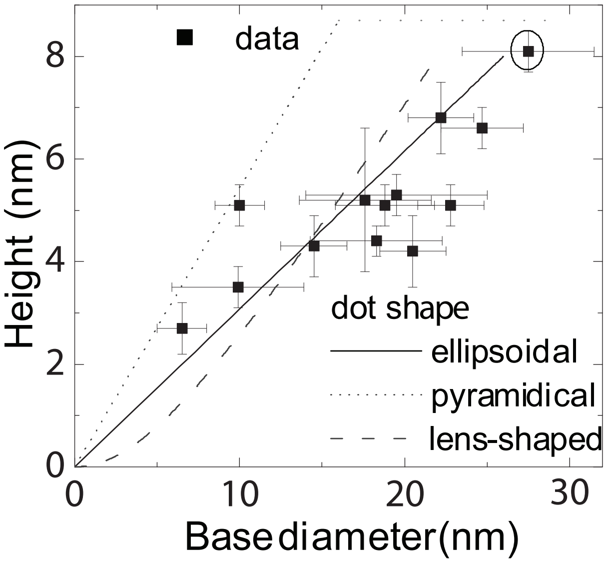

Figure 4.9: *Height versus base diameter for the 13 measured QDs (symbols). Theoretical curves for ellipsoidal (solid line, height $h = 8\,\mathrm{nm}$, diameter $d = 26\,\mathrm{nm}$), pyramidal (dotted line, $h = 8.7\,\mathrm{nm}$, base $b = 29\,\mathrm{nm}$) and lens-shaped QDs (dashed line, $h = 8\,\mathrm{nm}$, $d = 22\,\mathrm{nm}$).*

of the QDs. Considering their high uniformity we assume that all dots are identical. The measured height and base diameter then merely depend on the cleavage plane through the dot, occurring at random positions. For instance, the dot with the largest measured height is thought to be cleaved through its middle plane, whereas the others are cleaved closer to the edge. Each dot shape has therefore a specific height-base diameter relationship. Remarkably, the statistics of the 13 dots strongly deviates from a pyramidal shape (dotted line), previously found by X-STM [28, 42]. Better agreement is found using a lens-shape (dashed line) or ellipsoidal (solid line) QD, which agrees well with the topography of the dot (outlined in Figure 4.11b).

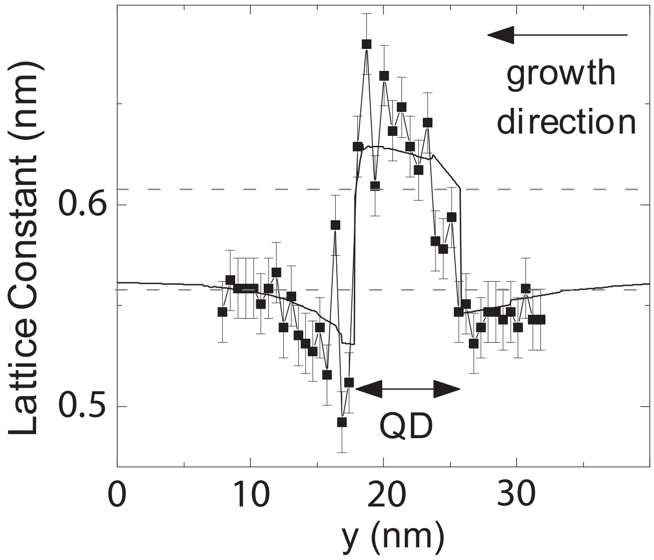

Figure 4.10: *Measured (symbols) and calculated (line) lattice constant profile through the middle plane in the growth direction of an InAs QD. The dashed lines indicate the lattice constant of bulk InAs (0.61 nm) and GaAs (0.56 nm).*

To obtain a full characterization of the QD shape and composition we have performed a detailed analysis of the representative dot in Figures 4.8 and 4.11b. In particular, the indium concentration profile follows from analysis of the lattice constant (Figure 4.10) and the outward relaxation (Figure 4.11a). The lattice constant is determined in the middle of the dot by taking line profiles across the cleaved surface and measuring the distances between the atom rows, using the Fourier filtered topography image (Figure 4.8). The lattice constant increases from the GaAs value at the bottom of the dot to the InAs value at the top.

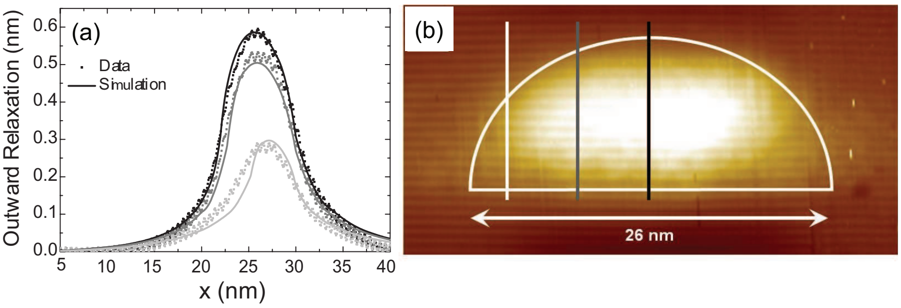

Figure 4.11: *(a) Measured (symbols) and simulated (solid lines) outward relaxation at three different positions with respect to the middle of an InAs QD. (b) Topography image taken by X-STM of the tallest QD measured. The z-range of this image is 0.7 nm. The solid lines indicate the positions at which the outward relaxation is plotted in (a).*

The measured outward relaxation at different lateral positions in the cleavage plane (cf. Figure 4.11b) is compared to simulations (Figure 4.11a). The simulation is performed with finite element calculations based on continuum elasticity theory. In these calculations the QD consist of an InGaAs alloy, in which the internal indium concentration profile is described by an expression that uses the indium end concentrations at different points inside the dot and using linear interpolation in between. The dot is assumed to be surrounded by a pure GaAs matrix and is on top of a seven monolayer thick $In_{0.225}Ga_{0.775}As$ wetting layer (WL). The thickness of the WL has been determined experimentally by X-STM at a position far from a QD (not shown) and agrees well with a total indium content of 1.7 ML.

4.3.4 Discussion

Comparing the measured and modeled outward relaxation, we obtain excellent agreement with an ellipsoidal dot, whose shape is described by the equation $(x/13)^2 + (y/8)^2 = 1$ (dimensions in nm) and with the indium profile depicted in Figure 4.12. The indium concentration varies significantly over the dot. The fraction InAs increases vertically from 70% at the base center to 100% at the top center. In addition, horizontally the fraction InAs decreases to 25% at the base edge, evolving in a 22.5% 7 ML thick wetting layer. These dot parameters

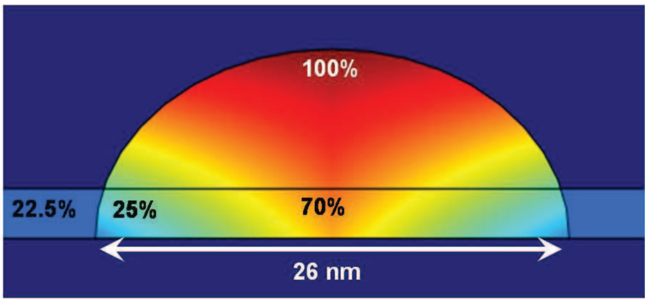

Figure 4.12: *Simulated indium content of a InAs QD. The color scale indicates the percentage of indium arsenide composition, and the given numbers correspond to the end values at the top center, base center, base edge and wetting layer.*

nicely reproduce the variation of the lattice constant in going from bottom center to top center as shown by the solid line in Figure 4.10, which is further evidence of the large gradients in indium content.

It is important to note that this level of agreement between simulation and data could not be obtained with a lens-shaped dot or using a dot without WL. The present simulations thus represent the simplest dot shape and composition that matches the data. More complicated faceted dots [29] cannot be disregarded but additional minor changes in the dot shape would not greatly influence the results we have found. Our relatively tall dots with large indium gradients differ significantly from some of the dots previously used in calculations, where usually a fixed InAs fraction is assumed.

Linking this geometry and composition to the previously performed photoluminescence (PL) and hole charging experiments in high magnetic fields on the *same* sample [43], requires a sophisticated model, which is beyond the scope of this paper. However, by qualitative arguments we are able to explain the PL emission energy of these dots. In view of the strong indium gradient found in these dots and the fact that the energy gap of InAs is lower than that of GaAs, the wavefunction is expected to be localized primarily in the top (indium rich) region of the QDs. This would reduce both the effective height and the effective diameter that have to be used as input parameters in a simplified model to calculate the emission energy. Furthermore, our measured geometry can be used as input for calculations to determine the hole charging sequence and the character of the hole wavefunctions, which are still under debate.

4.3.5 Conclusion

We have measured the shape, size and composition of self-assembled InAs QDs in a GaAs matrix. We have found that the dot shape is best described by an ellipsoid with a strong indium gradient in both horizontal and vertical directions. This conclusion is supported by the outward relaxation and lattice constant profiles across the dot, and by the height-base diameter statistics on 13 individual QDs. These results are crucial for a more thorough understanding of the influence of the dot's geometry on its spectroscopic properties.

4.4 Lateral quantum dot molecules in high magnetic fields

4.4.1 Introduction

Coupling between individual QDs is a necessity to apply these systems in quantum information processing [44] and as entangled photon sources [45]. The technologically easiest way to couple QDs and create so-called quantum dot molecules (QDMs) is the vertical stacking of QDs along the growth direction of the host semiconductor [46], but also electrostatically defined QDMs have been realized [47,48] and the formation of lateral QDMs has been demonstrated [49].

The coupling and entanglement of quantum states in such systems has been shown [48, 50–52], as well as the electrical manipulation of the coupling strength [53]. Because the number of coupled QDs is limited to several tens both in vertically stacked structures and electrostatically defined dots, lateral arrangements of QDs are preferred for large scale applications.

The dots can be grown in such a configuration that quantum mechanical coupling between the dots becomes important [51]. For strongly quantum-mechanically coupled QDs the carrier wavefunctions delocalize due to inter-dot tunneling, leading to extended states that are a coherent quantum mechanical superposition of the individual QD states. The quantum mechanical coupling is strongly dependent on the distance between two dots and has been shown to be $\approx 1\,\mathrm{meV}$ for dots less than $10\,\mathrm{nm}$ apart [51, 53].

Alternatively, the coupling can be mediated by interactions between the carriers in the dots and with the hosting semiconductor material. This coupling include effects such as the influence of carrier exchange channels with the wetting layer, transfer of carriers to the largest QDs and the presence of non-radiative channels [54, 55]. The latter effects depend not solely on the distance between the individual QDs, since their surroundings are also important.

Here we investigate a system consisting of clusters of four laterally coupled self-assembled QDs grown on a patterned superlattice. The coupling between the dots is manipulated by and probed with a strong perpendicular magnetic field. PL spectra of these QDMs show that the coupling is magnetic field dependent and indicate that the QDs start to decouple around 15 T.

4.4.2 Experimental details

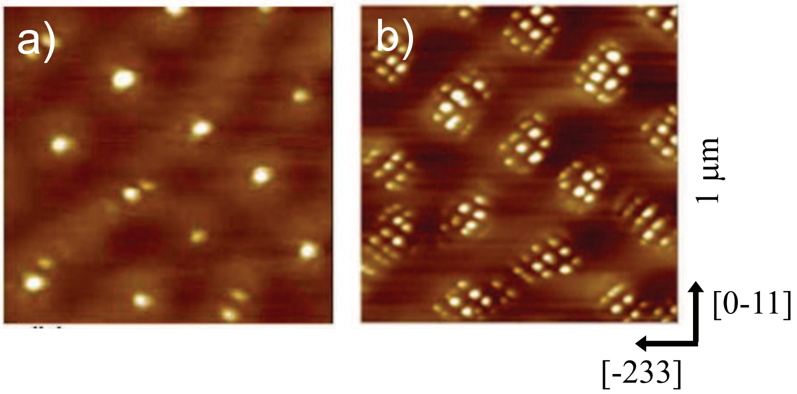

Figure 4.13: *AFM pictures of QDMs containing a) one dot per molecule, b) eight dots per molecule [56].*

The samples were grown by solid-source molecular-beam-epitaxy (MBE). Figure 4.13 shows AFM pictures of QDMs, containing one (a) and eight (b) atoms per molecule. The QDMs are formed by self-assembled growth of InAs quantum dots on self-organized (In,Ga)As/GaAs superlattice (SL) templates on a GaAs (311)B substrate. The substrate is covered by a 250-nm thick GaAs buffer layer followed by 10 periods of (In,Ga)As/GaAs superlattice (SL). On this SL InAs was deposited with a nominal thickness between 0.5 and 0.6 nm. A detailed description of the growth procedure can be found elsewhere [57,58].

The QDMs we have used for PL studies contain on average four laterally coupled quantum dots (not shown in Figure 4.13). The QD density is $\approx 10^{10}\,\mathrm{cm}^{-2}$. To enhance the coupling between the carriers we have used modulation-doped samples. The n- and p-type modulation doped samples are obtained by inserting 30 nm Si- or Be-doped GaAs, which results in a two dimensional carrier density of 4 and $2 \cdot 10^{11}\,\mathrm{cm}^{-2}$ for Si and Be doping, respectively. We have used two reference samples, so we can decide which features are characteristic for the QDMs. A sample of isolated QDs, grown on the same template as the QDMs and a sample containing a two-dimensional matrix of closely packed QDs. These two samples represent the limiting cases of isolated QDs and an infinite amount of coupled QDs.

Polarized PL experiments were performed on an ensemble of QDMs in static magnetic fields up to $B = 30\,\mathrm{T}$ and in pulsed magnetic fields up to $B = 42\,\mathrm{T}$ in Faraday configuration at $T = 4.2\,\mathrm{K}$. The excitation was provided by a Ti:Sapphire laser operating at a wavelength of 720-740 nm for the experiments in a static magnetic field and by a solid state laser operating at 532 nm for the experiments in pulsed magnetic fields. The luminescence was dispersed by a single grating spectrometer (300 g/mm grating, f=30 cm) and recorded by a LN-cooled InGaAs camera.

4.4.3 Experimental results

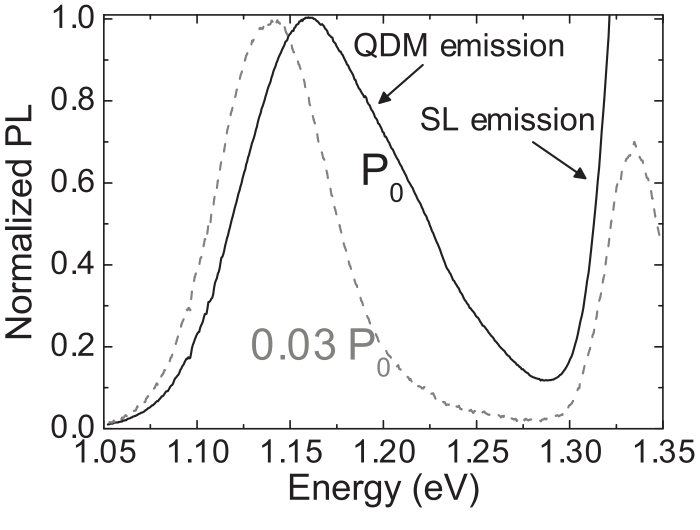

Figure 4.14: *Photoluminescence of the n-type doped QDM sample for two excitation powers.* $\lambda_{exc} = 720\,nm$, $P_0 \approx 5\,kW/cm^2$, $T = 4.2\,K$.

Figure 4.14 shows the emission of the n-type doped QDMs for low ($p \approx 0.15$ kW/cm^2) and high ($p \approx 5$ kW/cm^2) excitation power. The width (FWHM) of the emission peak at low excitation power is 70 meV, which is about twice the width of the luminescence of conventional isolated InAs QDs (cp. Figure 4.3), due to a larger size and composition distribution of the dots in different QDMs. The PL peak broadens significantly at high excitation powers and shifts towards higher energies, which is an indication of the formation of extended states in the QDMs due to coupling of the dots [58].

In contrast to the isolated QDs studied in the first paragraph of this chapter, we do not observe excited states appearing with increasing excitation power (cp. Figure 4.3). This might be attributed to emission from the SL which is close to the QD ground state emission, so excited states in the QDs are not confined. Another possible explanation is the presence of non-radiative channels [59].

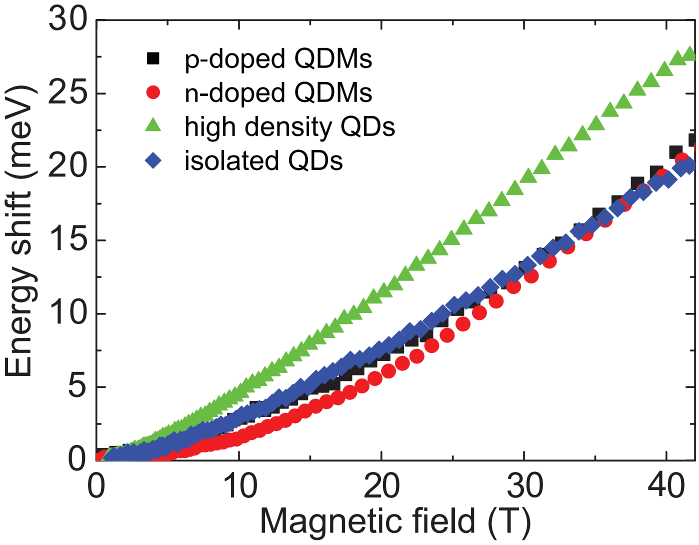

Figure 4.15: *Exciton recombination energies vs. magnetic field for the p-doped QDMs (black squares), n-doped QDMs (red circles), a two-dimensional coupled network [60] (green triangles) and an isolated QD samples (blue diamonds).* $\lambda_{exc} = 532$ *nm,* P_{exc} *~0.1 kW/cm*^{2}*,* T *= 4.2 K for all spectra.*

The emission energy in a magnetic field of the QDMs at low excitation powers, where the emission peak is not broadened, is shown in Figure 4.15. Up to $B = 42\,\mathrm{T}$ the emission of the sample containing a layer with a high density of QDs shows a significantly stronger shift than the emission of the other samples, which we attribute to the two-dimensional coupling of the dots in this sample, making it behave like a two-dimensional quantum well. For the other three samples a transition from a quadratic diamagnetic shift to a linear shift is observed around $B = 15\,\mathrm{T}$. For low magnetic fields the shift is quadratic in the magnetic field, for higher magnetic fields the energy dependence is linear. This energy dispersion indicates a transition from the spatial confinement regime to the magnetic confinement regime. The emission of the QDM samples shows a shift which is smaller than the shift of the emission of the isolated QDs below 20 T and larger above 20 T. We note that the behavior of the diamagnetic shift is very similar for the isolated dots grown on the template and the QDMs. Moreover, the diamagnetic shift is stronger than observed in QD samples which are not grown on a template (cf. Figure 4.5).

Due to the limited exposure time (~ms) in pulsed magnetic fields, the spectral resolution is worse than in the static magnetic field experiments, where the exposure time is in principle unlimited. With our pulsed setup we do not have polarizers in this spectral region, so we cannot determine the circularly polarized emission up to 42 T. Furthermore, because we are using fibers instead of a focussing lens for the excitation, we cannot reach the high excitation powers at which we observe the asymmetric broadening. In the following we show the results obtained by polarized PL spectroscopy in static magnetic fields under low and high excitation powers.

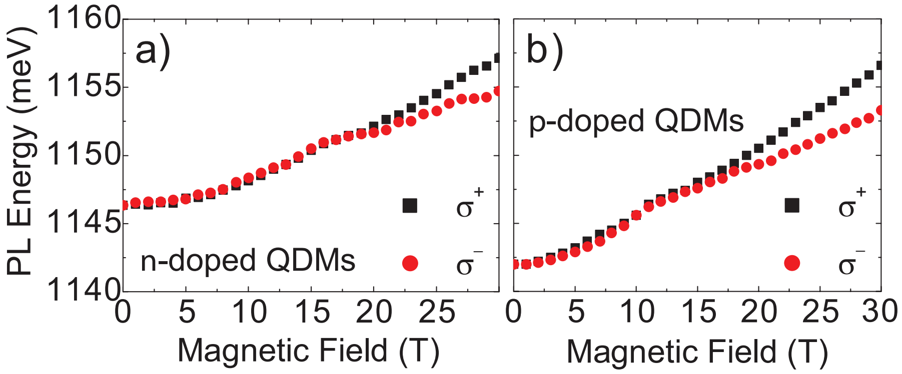

Figure 4.16: *Polarized exciton recombination energies vs. magnetic field for the n-doped QDMs (a) and p-doped QDMs (b). $\lambda_{exc} = 720\,\mathrm{nm}$, P_{exc} ~0.5 kW/cm^2 for (a) and 740 nm, 0.05 kW/cm^2 for (b), $T = 4.2\,K$ for both spectra.*

The peak energy of the circularly polarized emission of the QDMs is shown in Figures 4.16(a) and (b). The spectra were taken at low excitation densities $(0.01 - 0.1P_0)$, and the peak position is obtained by fitting the spectra with a single gaussian. The experimental resolution is limited by the ensemble averaging. The size of the symbols corresponds to the experimental inaccuracy of the measurements.

The spin splitting, defined as $E_{\sigma+} - E_{\sigma-}$ is given in Figure 4.17 for the

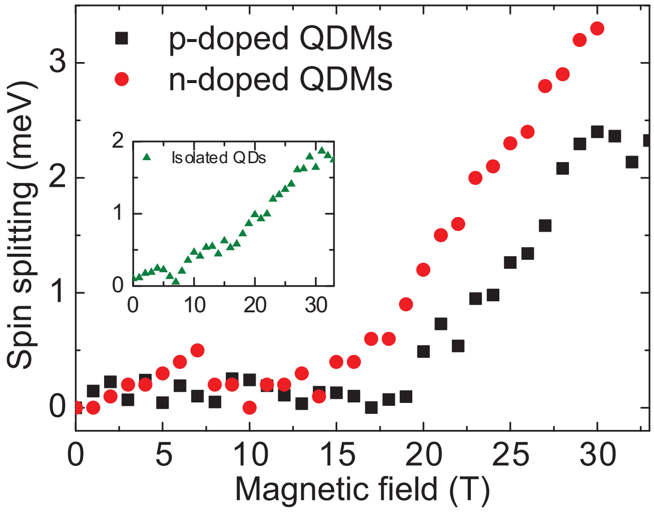

Figure 4.17: *Spin splitting ($E_{\sigma^+} - E_{\sigma^-}$) for p-doped QDMs (black squares), n-doped QDMs (red circles) and isolated QDs (inset, green triangles).* $\lambda_{exc} =$ *740 nm,* P_{exc} *~0.05 kW/cm*^{2} *for p-doped sample and isolated QDs and 720 nm, 0.5 kW/cm*^{2} *for the n-doped sample,* $T = 4.2\,K$ *for all spectra.*

QDMs and the isolated QD reference sample (inset). The σ^+ (σ^-) polarized spectra correspond to the recombination of an electron with spin up (down) and a hole with $J_z = -3/2$ ($J_z = 3/2$). At magnetic fields below 15 T the emission from the QDMs is unpolarized, i.e. the spin splitting is zero within the experimental resolution, whereas the sample with isolated quantum dots (QDs) shows a continuous Zeeman-splitting of the polarized emission.

At high magnetic fields, the emission of the QDMs starts to become polarized and at $B = 30\,$T the splitting of the energy levels (3.3 meV and 2.4 meV for the p-doped and n-doped sample respectively), is significantly larger than the spin splitting of the isolated QDs (1.9 meV). At the magnetic field where the splitting of the emission into two circular polarized states starts (15 T for the p-doped, 20 T for the n-doped QDMs, cf. Figure 4.17) also a kink in the diamagnetic shift is observed (cf. Figures 4.16(a) and (b)). The onset of the circular polarization occurs at the transition from the regime where the excitons are spatially confined to the magnetic confinement regime.

Figure 4.18 shows spectra for the p- and n-type doped QDMs at high excitation power densities ($P_0 \sim 5$kW/cm^2) at $B = 0 - 30\,$T. A narrowing of the emission is observed for both samples by increasing the magnetic field. Since

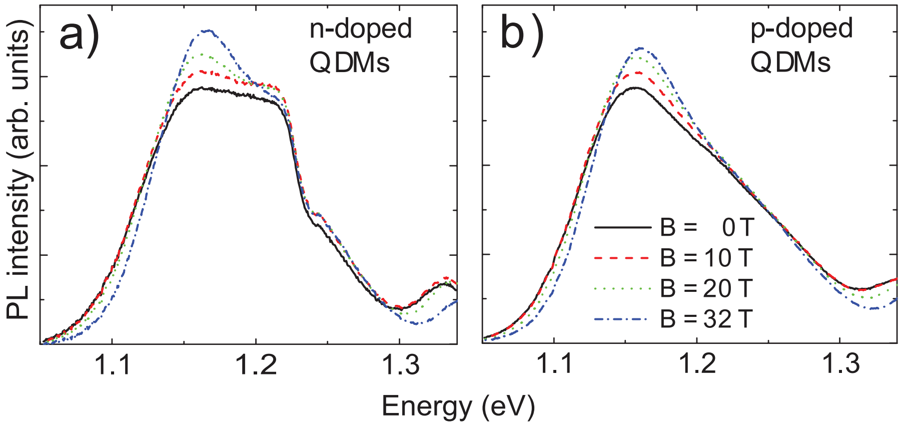

Figure 4.18: *Photoluminescence of the doped QDMs at* $B = 0, 10, 20, 30$ *T.* $\lambda_{exc} = 720\,\text{nm}$, $P_{\text{exc}} \sim 5$ *kW/cm*^{2}, $T = 4.2\,K$*. (a) n-type doped QDMs. (b) p-type doped QDMs.*

the spectra do not have a well-defined line-shape, we use their FWHM as a measure for the width. The FWHM of the PL spectra in both circular polarizations up to 30 T shown in Figures 4.19(a) and (b) for the n-type doped QDMs and p-type doped QDMs respectively.

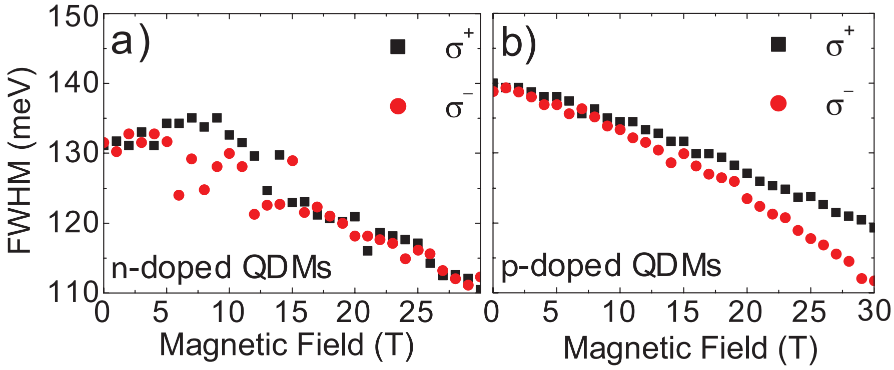

Figure 4.19: *Magnetic field dependence of the FWHM of the polarized PL peak for (a) n-type doped QDMs and (b) p-type doped QDMs.* $\lambda_{exc} = 720\,\text{nm}$, $P_{exc} \sim 5\,\text{kW/cm}^2$ $T = 4.2\,K$.

The asymmetric broadening of the peak is significantly reduced at high magnetic fields for both samples. The decrease of the FWHM of the emission peak of the QDMs at 30 T varies from 10% to 20% depending on the excitation conditions, whereas the FWHM of the peak emission of an isolated dot reference sample increases with 17%, possibly due to contributions of excited states.

4.4.4 Discussion

Experimentally we find that the excitation dependence [56, 58] and magnetic field dependence of the QDM samples is very different from the QDs investigated in the first part of this chapter (compare Figure 4.14 and 4.19 respectively with Figure 4.3): the FWHM of the QDM PL is much larger than that of the aforementioned isolated QDs. This is due to larger fluctuations in size and composition from dot to dot, and makes the QDM samples less well-defined. Furthermore, we observe an asymmetric broadening upon increasing excitation power, where for isolated QDs we see excited states appearing at equidistant energies. In a magnetic field we observe a significant decrease of the linewidth for the QDMs and a non-linear Zeeman splitting, which is zero up to around 15 T, where the magnetic confinement takes over from the spatial confinement.

Without a magnetic field, the extension of the confined wavefunction within a QD is determined by the lateral size (radius) of the QD, which in this system is l_0 ~10 nm. However the details of the wavefunction strongly depend on the precise shape of the confinement potential, which can be calculated by considering the composition and shape of the dots. The effect of the magnetic field on the extension of the wavefunction compared to the confinement can be roughly estimated by considering the magnetic length ($l_B = \sqrt{\hbar/eB}$). For both the QDMs and the isolated QDs the magnetic confinement starts to be comparable to the size confinement around 15 T, which is experimentally seen in the transition from a quadratic to a linear energy shift.

In our samples the distance between two QDs within one QDM is in the same order as the lateral size of the QDs, i.e. around 25 nm. For this inter-dot distance the quantum mechanical coupling is expected to be very weak. Previous experiments on tunnel coupled dots showed that the tunnel splitting is in the order of 1 meV for dots less than 10 nm apart [51, 53]. Since the tunnel coupling decreases exponentially with the inter-dot distance, we cannot explain the observed broadening of several tens of meV by assuming the dots are tunnel coupled.

The distance between two QDMs is ~ 10 times larger, so we expect no significant coupling between QDs in different QDMs. Since the distance between two QDs is similar to their lateral size, any decoupling of the wavefunctions between the dots in a molecule is expected to occur simultaneously with the onset of magnetic confinement within the dots, although the dots are not quantum mechanically coupled. When the extent of the wavefunctions is reduced such that they are localized within the dots, the influence of their environment outside the dots will reduce.

Above reasoning suggests that the absence of spin polarization in the emission of the QDMs for low magnetic fields is due to some sort of (electrostatic) coupling between the QDs. A possible explanation is the formation of a so-called mini-band of extended states induced by the superlattice [55, 61]. As the excitation intensity is increased this mini-band is filled, which leads to a broadening of the PL. Since the lifetime of excitons in this mini-band is expected to be much shorter than that of excitons localized in the dots, time-resolved PL measurements could be performed. In this case the narrowing of the PL in a magnetic field could be explained by a magnetic-field induced change of the exciton lifetimes and/or a change in the relaxation from the extended to the localized states as soon as the magnetic length becomes smaller than the interdot length.

All experimental data shown give strong indications the dots within one QDM are coupled by a mechanism different from tunnel coupling. However, a quantitative analysis, taking into account the precise shape and composition of the dots, Coulomb interactions between the charged particles and all relevant relaxation processes, is needed to explore the nature of this coupling. In all our experiments the p- and n-doped samples behave in a similar way, which indicates that the nature of the most abundant charge carries does not play a major role in the coupling mechanism. To obtain further information on the nature of the coupling between the QDs, future experiments will focus on the one side on measurements on a single QDM where the magnetic and electric field (i.e. the number of electrons/holes per dot) can be tuned independently. Additionally with time-resolved PL measurements additional information on the relaxation processes between the dots can be obtained.

4.4.5 Conclusion

We have investigated clusters of four coupled QDs by means of polarized photoluminescence in high magnetic fields. The shift in energy in a magnetic field and the absence of circular polarization for magnetic fields $< 15\,\mathrm{T}$ give strong indications that the dots within one QDM are coupled and this coupling can be tuned and probed by a magnetic field. This statement is supported by the behavior of the asymmetric broadening of the spectra in magnetic fields, which strongly reduces above $15\,\mathrm{T}$. The inter-dot distance is too large for the dots to be tunnel coupled and we speculate that the dots are coupled through the underlying superlattice.

References

[1] Bimberg, D., Grundmann, M., and Ledentsov, N. *Quantum Dot Heterostructures.* Wiley, (1999).

[2] Yuan, Z., Kardynal, B. E., Stevenson, R. M., Shields, A. J., Lobo, C. J., Cooper, K., Beattie, N. S., Ritchie, D. A., and Pepper, M. *Science* **295**, 102– (2002).

[3] Arakawa, Y. and Sakaki, H. *Appl. Phys. Lett.* **40**, 939 (1982).

[4] Kouwenhoven, L. P., Austing, D. G., and Tarucha, S. *Rep. Prog. Phys.* **64**, 701 (2001). and references therein.

[5] Drexler, H., Leonard, D., Hansen, W., Kotthaus, J. P., and Petroff, P. M. *Phys. Rev. Lett.* **73**, 2252 (1994).

[6] Warburton, R. J., Miller, B. T., Durr, C. S., Bodefeld, C., Karrai, K., Kotthaus, J. P., Medeiros-Ribeiro, G., Petroff, P. M., and Huant, S. *Phys. Rev. B* **58**, 16221 (1998).

[7] Wibbelhoff, O. S., Lorke, A., Reuter, D., and Wieck, A. D. *Appl. Phys. Lett.* **86**, 092104 (2005).

[8] Reuter, D., Kailuweit, P., Wieck, A. D., Zeitler, U., Wibbelhoff, O., Meier, C., Lorke, A., and Maan, J. C. *Phys. Rev. Lett.* **94**, 26808 (2005).

[9] Reuter, D., Schafmeister, P., Kailuweit, P., and Wieck, A. D. *Physica E* **21**, 445 (2004).

[10] He, L. and Zunger, A. *Phys. Rev. B* **73**, 115324 (2006).

[11] He, L., Bester, G., and Zunger, A. *Phys. Rev. Lett.* **95**, 246804 (2005).

[12] Climente, J. I., Planelles, J., Pi, M., and Malet, F. *Phys. Rev. B* **72**, 233305 (2005).

[13] Arakawa, Y., Yamauchi, T., and Schulman, J. N. *Phys. Rev. B* **43**, 4732 (1991).

[14] Ancilotto, F., Fasolino, A., and Maan, J. C. *Phys. Rev. B* **38**, 1788 (1988).

[15] Bayer, M., Kuther, A., Forchel, A., Gorbunov, A., Timofeev, V. B., Schafer, F., Reithmaier, J. P., Reinecke, T. L., and Walck, S. N. *Phys. Rev. Lett.* **82**, 1748 (1999).

[16] Bayer, M., Stern, O., Hawrylak, P., Fafard, S., and Forchel, A. *Nature* **405**, 923 (2000).

[17] Raymond, S., Studenikin, S., Sachrajda, A., Wasilewski, Z., Cheng, S. J., Sheng, W., Hawrylak, P., Babinski, A., Potemski, M., Ortner, G., and Bayer, M. *Phys. Rev. Lett.* **92**, 187402 (2004).

[18] Seidl, S., Kroner, M., Dalgarno, P. A., Hogele, A., Smith, J. M., Ediger, M., Gerardot, B. D., Garcia, J. M., Petroff, P. M., Karrai, K., and Warburton, R. J. *Phys. Rev. B* **72**, 195339 (2005).

[19] Luttjohann, S., Meier, C., Lorke, A., Reuter, D., and Wieck, A. D. *Appl. Phys. Lett.* **87**, 163117 (2005).

[20] Sidor, Y., Partoens, B., Peeters, F. M., Schildermans, N., Hayne, M., Moshchalkov, V. V., Rastelli, A., and Schmidt, O. G. *Phys. Rev. B* **73**, 155334 (2006).

[21] Babinski, A., Awirothananon, S., Lapointe, J., Wasilewski, Z., Raymond, S., and Potemski, M. *Physica E* **26**, 190 (2005).

[22] Banin, U., Cao, Y., Katz, D., and Millo, O. *Nature* **400**, 542 (1999).

[23] Narvaez, G. A., Bester, G., and Zunger, A. *J. Appl. Phys.* **98**, 043708 (2005).

[24] Wasilewski, Z. R., Fafard, S., and McCaffrey, J. P. *Journal of Crystal Growth* **201-202**, 1131 (1999).

[25] Schliwa, A., Winkelnkemper, M., and Bimberg, D. *Phys. Rev. B* **76**, 205324 (2007).

[26] Walther, T., Cullis, A. G., Norris, D. J., and Hopkinson, M. *Phys. Rev. Lett.* **86**, 2381 (2001).

[27] Leonard, D., Krishnamurthy, M., Reaves, C. M., Denbaars, S. P., and Petroff, P. M. *Appl. Phys. Lett.* **63**, 3203 (1993).

[28] Bruls, D. M., Vugs, J. W. A. M., Koenraad, P. M., Salemink, H. W. M., Wolter, J. H., Hopkinson, M., Skolnick, M. S., Long, F., and Gill, S. P. A. *Appl. Phys. Lett.* **81**, 1708 (2002).

[29] Costantini, G., Rastelli, A., Manzano, C., Acosta-Diaz, P., Katsaros, G., Songmuang, R., Schmidt, O., v. Kanel, H., and Kern, K. *Journal of Crystal Growth* **278**, 38 (2005).

[30] Offermans, P., Koenraad, P. M., Wolter, J. H., Granados, D., Garcia, J. M., Fomin, V. M., Gladilin, V. N., and Devreese, J. T. *Appl. Phys. Lett.* **87**, 131902 (2005).

[31] Fry, P. W., Itskevich, I. E., Mowbray, D. J., Skolnick, M. S., Finley, J. J., Barker, J. A., O'Reilly, E. P., Wilson, L. R., Larkin, I. A., Maksym, P. A., Hopkinson, M., Al-Khafaji, M., David, J. P. R., Cullis, A. G., Hill, G., and Clark, J. C. *Phys. Rev. Lett.* **84**, 733 (2000).

[32] Kleemans, N. A. J. M., Bominaar-Silkens, I. M. A., Fomin, V. M., Gladilin, V. N., Granados, D., Taboada, A. G., Garcia, J. M., Offermans, P., Zeitler, U., Christianen, P. C. M., Maan, J. C., Devreese, J. T., and Koenraad, P. M. *Phys. Rev. Lett.* **99**, 146808 (2007).

[33] Babinski, A., Potemski, M., Raymond, S., Lapointe, J., and Wasilewski, Z. R. *Phys. Rev. B* **74**, 155301 (2006).

[34] Fock, V. *Z. Phys.* **47**, 446 (1928).

[35] Darwin, C. *Proc. Cambridge Philos. Soc.* **27**, 86 (1930).

[36] Kailuweit, P., Reuter, D., Wieck, A. D., Wibbelhoff, O., Lorke, A., Zeitler, U., and Maan, J. C. *Physica E* **32**, 159 (2006).

[37] Reuter, D., Kailuweit, P., Wieck, A. D., Zeitler, U., and Maan, J. C. *Physica E* **26**, 446 (2005).

[38] Medeiros-Ribeiro, G., Ribeiro, E., and Westfahl, H. *Appl. Phys. A* **77**, 725 (2003).

[39] Alegre, T. M., Hernandez, F., Pereira, A., and g. Medeiros-Ribero. *Phys. Rev. Lett.* **97**, 236402 (2006).

[40] Pryor, C. E. and Flatté, M. E. *Phys. Rev. Lett.* **96**, 26804 (2006).

[41] Since the diamagnetic shift of the energy levels is small compared to the confinement energy, we assume a constant exciton binding energy for all magnetic fields.

[42] Ulloa, J. M., Celebi, C., Koenraad, P. M., Simon, A., Gapihan, E., Letoublon, A., Bertru, N., Drouzas, I., Mowbray, D. J., Steer, M. J., and Hopkinson, M. *J. Appl. Phys.* **101**, 081707 (2007).

[43] Blokland, J. H., Wijnen, F. J. P., Christianen, P. C. M., Zeitler, U., Maan, J. C., Kailuweit, P., Reuter, D., and Wieck, A. D. *Phys. Rev. B* **75**, 233305 (2007).

[44] Biolatti, E., Iotti, R. C., Zanardi, P., and Rossi, F. *Phys. Rev. Lett.* **85**, 5647 (2000).

[45] Gywat, O., Burkard, G., and Loss, D. *Phys. Rev. B* **65**, 205329 (2002).

[46] Solomon, G. S., Trezza, J. A., Marshall, A. F., and Harris, Jr., J. S. *Phys. Rev. Lett.* **76**, 952 (1996).

[47] Gaudreau, L., Studenikin, S. A., Sachrajda, A. S., Zawadzki, P., Kam, A., Lapointe, J., Korkusinski, M., and Hawrylak, P. *Phys. Rev. Lett.* **97**, 036807 (2006).

[48] Korkusinski, M., Gimenez, I. P., Hawrylak, P., Gaudreau, L., Studenikin, S. A., and Sachrajda, A. S. *Phys. Rev. B* **75**, 115301 (2007).

[49] Songmuang, R., Kiravittaya, S., and Schmidt, O. G. *Appl. Phys. Lett.* **82**, 2892–2894 (2003).

[50] Bayer, M., Hawrylak, P., Hinzer, K., Fafard, S., Korkusinski, M., Wasilewski, Z. R., Stern, O., and Forchel, A. *Science* **291**, 451 (2001).

[51] Beirne, G. J., Hermannstadter, C., Wang, L., Rastelli, A., Schmidt, O. G., and Michler, P. *Phys. Rev. Lett.* **96**, 137401 (2006).

[52] Delgado, F., Shim, Y.-P., Korkusinski, M., and Hawrylak, P. *Phys. Rev. B* **76**, 115332 (2007).

[53] Stinaff, E. A., Scheibner, M., Bracker, A. S., Ponomarev, I. V., Korenev, V. L., Ware, M. E., Doty, M. F., Reinecke, T. L., and Gammon, D. *Science* **311**, 636 (2006).

[54] Sanguinetti, S., Henini, M., Grassi Alessi, M., Capizzi, M., Frigeri, P., and Franchi, S. *Phys. Rev. B* **60**, 8276 (1999).

[55] Lan, S., Akahane, K., Song, H.-Z., Okada, Y., Kawabe, M., Nishimura, T., and Wada, O. *Phys. Rev. B* **61**, 16847 (2000).

[56] van Lippen, T. *Strain Engineered Lateral Quantum Dot Molecules.* Proefschrift TU/e, (2006).

[57] v. Lippen, T., Notzel, R., Hamhuis, G. J., and Wolter, J. H. *Appl. Phys. Lett.* **85**, 118 (2004).

[58] v. Lippen, T., Silov, A. Y., and Notzel, R. *Phys. Rev. B* **75**, 115414 (2007).

[59] Grundmann, M. and Bimberg, D. *Phys. Rev. B* **55**, 9740 (1997).

[60] In the high density QD sample, the QDs are coupled in a two-dimensional network.

[61] Lan, S., Akahane, K., Song, H.-Z., Okada, Y., Kawabe, M., Nishimura, T., Nishikawa, S., and Wada, O. *Journal of Applied Physics* **88**, 227 (2000).

Chapter 5

Excitons in self-assembled InAs/GaAs quantum rings

Abstract

We have investigated the exciton energy level structure of InAs/GaAs quantum rings by photoluminescence (PL) spectroscopy. Firstly, the PL of a large ensemble of quantum rings is measured in magnetic fields up to 30 T for different excitation densities. We show that the energy levels have features characteristic for excitons confined in a ring geometry. A model based on realistic parameters of the self-assembled quantum rings, reproduces the essential features of the observed PL spectra on the basis of the calculated optical transition probabilities. Secondly we discuss the PL of single quantum rings in magnetic fields up to 30 T, where, in contrast to the ensemble measurements, the ground state of individual rings is probed.

This work is based on:
N.A.J.M. Kleemans, J.H. Blokland et al. Phys. Rev. B **80**, 155318 (2009)

5.1 Introduction

The excitonic energy structure of self-assembled quantum dots is well studied [1, 2], cf. also Chapter 4. By magnetoluminescence experiments it has been demonstrated that the electronic energy levels in a quantum dot can be described by the Fock-Darwin model for a two-dimensional harmonic oscillator in a magnetic field [3–9]. Changing the geometry of quantum dots to a ring-like shape modifies the energy spectrum. For electrons, it has been shown that the ring geometry gives rise to signatures of the Aharonov-Bohm (AB) effect [10–15] as explained in more detail in Chapter 2. The AB effect is a purely quantum mechanical phenomenon, describing the oscillatory behavior of the energy levels of charged carriers confined in a ring-like geometry in the presence of a magnetic field [16]. This has recently been observed by magnetization measurements on self-assembled InAs/GaAs [17].

The optical emission of above-mentioned quantum rings has already been studied experimentally without a the presence of a magnetic field [18]. The emission of the different charged complexes showed for rings with up to six electrons an energy shell structure similar to that of quantum dots. However, the excitonic energy level structure has not been studied in magnetic fields higher than 9 T [19]. Since the boundary conditions on the wavefunction are related to the geometry of the confinement potential, we expect that the energy level structure of a quantum ring is different from the Fock-Darwin levels in a quantum dot.

Calculations performed using a model including strain and taking into account the oscillator strengths of the different exciton levels, showed that only a weak reminiscent feature of the AB effect in the PL spectrum of type I GaAs/AlGaAs and several type II nanorings might be observed [20]. Excitons are neutral excitations, thus we do not expect on forehand any sensitivity to the magnetic flux. However, since the exciton is a polarizable composite particle, the area between the different trajectories of the electron and the hole determines the phase picked up by the exciton [21]. Therefore the possible prominence of the AB effect for excitons strongly depends on their polarization. Recently, the exciton energy spectra for various models of the $\mathrm{In}_x\mathrm{Ga}_{x-1}\mathrm{As}$/GaAs self-assembled quantum rings were calculated and it was shown that the behavior of exciton energy spectra and optical-transition probabilities as a function of the applied magnetic field is very sensitive to the details of the quantum-ring shape [22].

In this chapter we measure the excitonic energy levels of self-assembled InAs/GaAs quantum rings in high magnetic fields. In the first part, we report on the optical properties of an ensemble of quantum rings in magnetic fields up to 30 T. Using different excitation densities we probe the magnetoluminescence of the ground and excited states. The experimental results are compared with the calculations based on the realistic quantum ring model. In the second part we show the results of PL of single rings up to 30 T. The spectral resolution is increased over two orders of magnitude, since the spectra are no longer inhomogeneously broadened. We use a low excitation power, so we only probe the ground state.

5.2 Ensemble magnetoluminescence measurements

5.2.1 Experimental details

For the ensemble PL studies, a sample containing a single layer of quantum rings is mounted in a liquid-helium bath cryostat at T=4.2 K. The excitation is provided by a tunable Dye laser operating at 2.0 eV. The excitation power is varied with a Babinet-Soleil compensator in combination with a linear polarizer. A Wollaston prism allowed for simultaneous detection of both circular polarizations. The PL signal is dispersed by a single grating spectrometer (Acton SP300i). The detection is performed by a liquid-nitrogen-cooled CCD camera. Static magnetic fields up to 30 T were applied parallel to the growth direction and the PL is detected in the Faraday configuration.

The sample used for the ensemble PL studies has a single layer of quantum rings with a density $n = 7 \times 10^9\,\mathrm{cm}^{-2}$ embedded in a GaAs matrix. Figure 5.1 shows an AFM picture (a) and two X-STM pictures (b,c) of quantum rings similar to those used in our study. From the X-STM images we find that the rings have a radius of $\approx 11.5\,\mathrm{nm}$ [23]. More importantly, we observe that the shape of these nanostructures is considerably different from an ideal ring: firstly, the ring is highly anisotropic and secondly, there is no hole in the middle of the ring, due to the presence of indium in its center.

5.2.2 Experimental results

The dependence of the quantum ring emission spectrum on the excitation density is shown in Figure 5.2a. The ground state emission energy of these rings is centered around 1.308 eV, typical for these nanostructures [15]. As can be observed at low excitation densities, the ground state emission has an inhomogeneous broadening with a Full-Width-at-Half-Maximum (FWHM) of 26 meV due to the distribution of ring sizes, shapes and composition. With increasing excitation density two additional peaks can be resolved. These peaks have an energy of 39 meV and 63 meV above the ground state energy. The peak po-

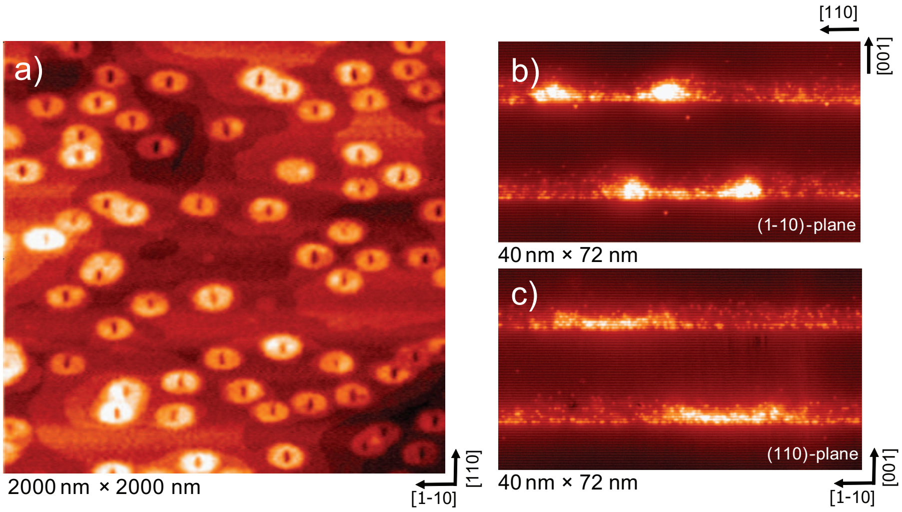

Figure 5.1: *(a) AFM picture of self-assemble InGaAs quantum rings (b,c) X-STM images of two quantum rings in the (1-10)-plane and the (110)-plane. A pronounded difference in the height of the rim between the [110] and [1-10] directions is observed.*

sitions do not depend on the excitation density, within the resolution of the system. The wetting layer emission (not shown) is centered around 1.438 eV which is 67 meV above the highest confined-state energy of the quantum rings.

We determine the energy of the ground state PL by fitting the spectra taken at low excitation densities by a Gaussian peak. Figure 5.2b shows the emission energy of the ground state as a function of the magnetic field for both circular polarizations. We observe a smooth dependence of the ground state energy as a function of the magnetic field. The observed ground state emission energy $E(B)$ of an exciton in a quantum ring in relatively small magnetic fields B is approximately given by [24]:

$$E(B) = E_0 \pm g_{ex}\mu_B B + \alpha_d B^2, \tag{5.1}$$

where E_0 is the emission energy at $B = 0\,\mathrm{T}$, g_{ex} is the exciton g factor, $\mu_B = +5.79 \times 10^{-5}\,\mathrm{eV/T}$ is the Bohr-magneton, and α_d is the diamagnetic coefficient. The second term of Equation (1) is the Zeeman term which gives rise to a spin induced splitting of the exciton PL in a magnetic field. We define g_{ex} as:

$$g_{ex} = \frac{E(\sigma^+) - E(\sigma^-)}{\mu_B B} \tag{5.2}$$

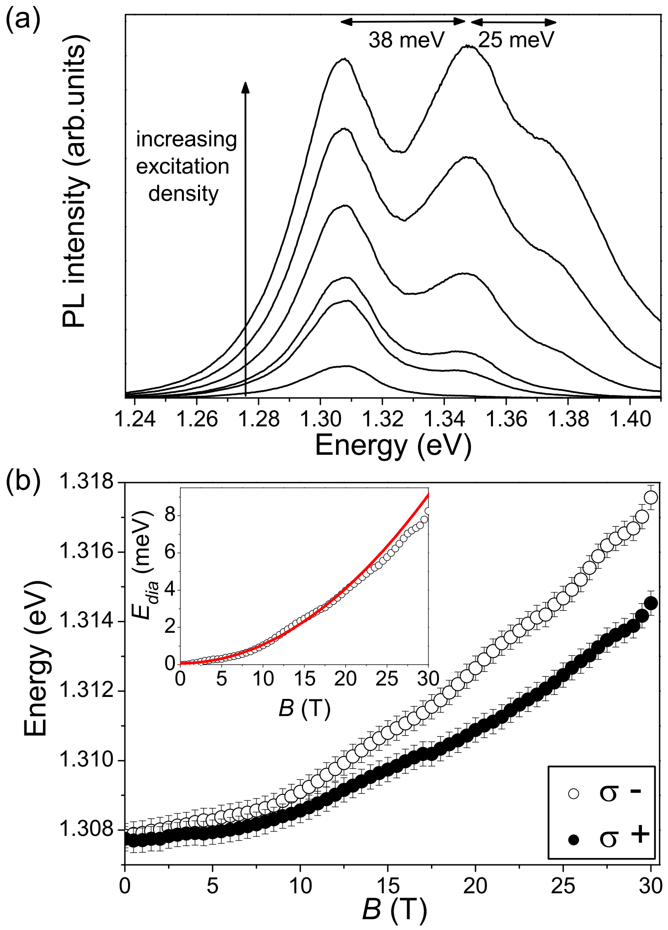

Figure 5.2: *(a) PL as a function of excitation density. Two excited states can be distinguished for higher excitation density located 38 meV and 63 meV above the ground state emission energy. (b) PL energy of the ground state as function of the magnetic field for both circular polarizations. The energies are determined by fitting the PL spectra for low excitation densities by a Gaussian peak. The inset shows the diamagnetic shift* E_{dia}*. The quadratic fit (red line) is used to determine the diamagnetic coefficient* α_d*.*

For our quantum rings we obtain g_{ex}=-1.7, in correspondence with previously reported values obtained on individual quantum rings and comparable to values found for quantum dots [25, 26]. In the inset of Figure 5.2b the diamagnetic shift E_{dia} is shown, defined by:

$$E_{dia} = \frac{E(\sigma^-) + E(\sigma^+)}{2} - E_0 \tag{5.3}$$

The diamagnetic shift also has a smooth dependence on the magnetic field. From the quadratic fit (red solid line) we find α_d=10 μeV/T^2, in good agreement with values earlier before for rings [19] and for dots [25].

To investigate the influence of the ring-like geometry on the excitonic behavior in the excited states of the quantum rings, we measured the magnetoluminescence of these structures for higher excitation intensities. The dependence of the PL for higher excitation densities on the magnetic field is shown in Figure 5.3a in intervals of 5 T in σ^- polarization. The dashed lines are a guide to the eye and follow the peak positions in magnetic field. We have determined the PL peak positions as function of magnetic field, as shown in Figure 5.3b. We observe a smooth dependence of the PL energies in a magnetic field. As can be seen in Figure 5.3a, both resolvable excited states split up in *two* separate peaks in magnetic field. Each of the PL peaks of the quantum rings split further with a smaller energy separation into two peaks of opposite circular polarization as a result of the Zeeman splitting.

5.2.3 Theoretical calculations

To understand the energy structure of the excitons we use a model based on the structural properties, i.e. size, shape and composition of these quantum rings obtained by X-STM measurements [23, 27, 28]. The model is used to calculate the single-exciton optical transition probability spectrum [22]. The results are shown in Figures 5.4a and 5.4b, for a non-interacting and an interacting electron-hole pair, respectively. In order to enhance the visibility, a Gaussian broadening (Γ=1 meV) is introduced for all the energy levels. For a non-interacting electron-hole pare we calculate that around the field of 15 T there is a crossover in the ground state energy (cf. Figure 5.4a), in agreement with magnetization experiments [17].

The inclusion of the Coulomb interaction results into a smooth behavior of the ground state energy as function of the magnetic field, as shown in Figure 5.4b. At a magnetic field of 15 T the calculated spectrum shows that the first excited state has a reduced optical spectral probability. This is due to the redistribution of the oscillator strength between the first excited state and the ground state in favor of the latter, especially when they are close to each other. In case of the interacting electron-hole pair the ground state energy is lowered by the energy of the electron-hole Coulomb attraction, which is 13 meV.

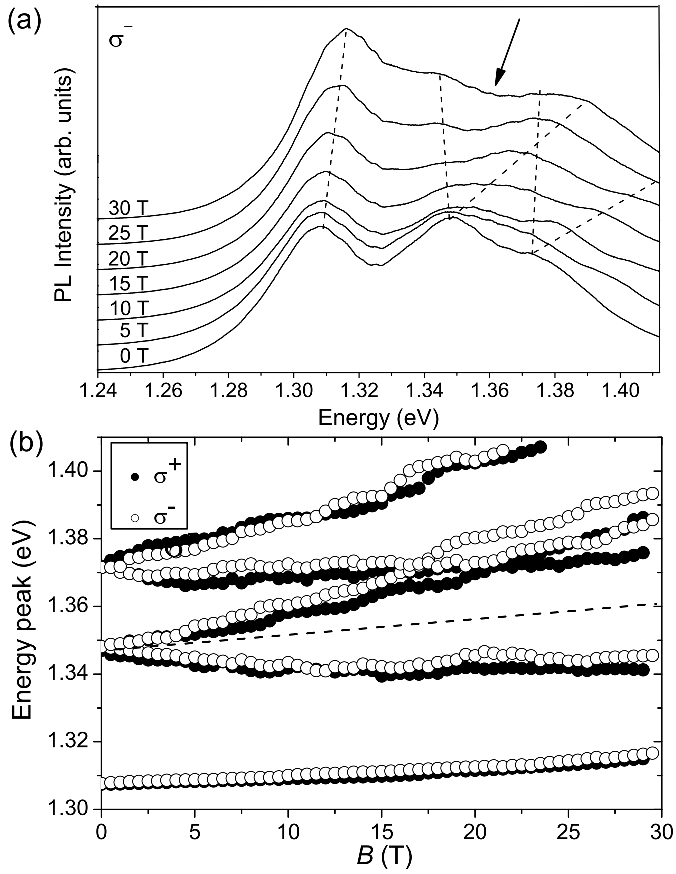

Figure 5.3: *(a) Excited states as a function of magnetic field in σ^- polarization. The dashed lines are guides to the eye in order to follow the evolution of the peak positions in magnetic field. The arrow indicates the emission energy at which for quantum dots a third peak is present. As opposed to quantum dots we observe a minimum in PL intensity. (b) The energy diagram showing the peak position in magnetic field in both σ^- (empty circles) and σ^+ (filled circles) polarization. The quantum rings exhibit splittings into two states of the different excited states, in contrast to quantum dots where a third peak (indicated by the dotted line) is observed.*

5.2.4 Discussion

In the following we compare the experimental results with the theoretical calculations. First we look at the ground state. The calculated ground state

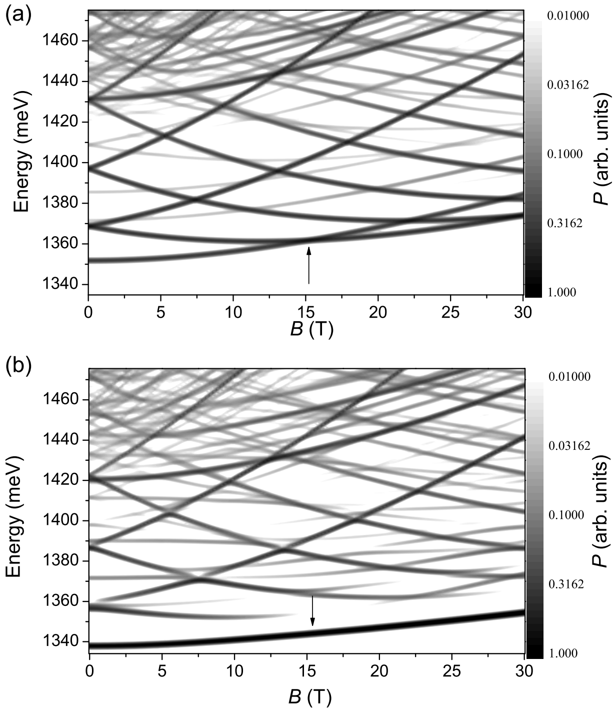

Figure 5.4: *Calculated optical transition probabilities for a realistic quantum ring in the case of (a) a non-interacting electron-hole pair and (b) an interacting electron-hole pair. The grey scale is logarithmic where black (white) corresponds to the highest (lowest) transition probability. The arrows correspond to the first excitonic AB resonance in the ground state.*

emission energy is 1.34 eV, in reasonable agreement with the measured ground state PL energy (1.31 eV). In general we find that the calculated energies are about 30 meV higher than the experimental values. The PL of the continuum states in the wetting layer is calculated to be at 1.43 eV, which agrees with the measured value of 1.438 eV. Moreover, the calculations show at B=30 T a 10 meV shift of the ground state to higher energy, where the experimental value is 8 meV, which means that the diamagnetic coefficient α_d is overestimated by approximately 25%. The Zeeman interaction is not taken into account in the calculations. Both experimentally and theoretically we find a smooth dependence of the ground state emission energy on the magnetic field. Also the oscillator strength of the ground state of the single exciton of our modeled quantum ring does not significantly change in magnetic field. In contrast to the AB effect of single electrons in these rings, we do not observe nor expect an excitonic AB effect based on our model. This leads to the conclusion that there is a strong Coulomb interaction between the electron and the hole (cp. Figures 5.4a and 5.4b) [21].

Secondly, to interpret the higher lying energy states, we will focus only on the states in the model having a large spectral transition probability (cf. Figure 5.4b), and compare them with the experimentally observed PL peaks. The first excited state (*p*-state with $l = 1$, cf. Figure 2.3) is expected at 20 meV above the ground state emission energy. In our experimental data we cannot resolve this peak. The second excited state (*d*-state with $l = 2$) at 58 meV above the ground state emission energy corresponds to the second peak in our experiment, whereas the calculated energy level at 1.42 eV, 82 meV above the ground state emission corresponds to the third peak we observe. In order to better compare the calculated spectra to the experimental spectra we introduce a Gaussian broadening Γ, which simulates the inhomogeneous broadening of the ensemble. For Γ=10 meV, we find the best comparison of the calculated spectra with the experimental data. Figure 5.5 compares the calculated and measured PL spectra for magnetic fields up to 30 T in steps of 5 T. The calculated and measured spectra show a striking qualitative resemblance, although the absolute values of the energy splittings are different in the model and the experiment. Importantly, the introduced broadening indeed shows that the first excited state is not resolvable in the magnetoluminescence data as a result of the inhomogeneous broadening. We do note that based on our model, which is consistent with the magnetization measurements on similar quantum rings [17], we assign the measured PL peaks to different excitonic states in the quantum rings as compared to the identification based on PLE measurements on single rings [29].

This excitonic behavior is typical for ring-like structures and different from the excitonic behavior of InAs/GaAs dots [5–9]. As opposed to the quantum rings, experiments on quantum dots resulted in a magnetic induced splitting of the *d*-state into 3 states [5, 6]. This *d*-state corresponds to the second peak in Figure 5.3a, having predominantly a $l = 2$ character. As is indicated with the dotted line in Figure 5.3b, a possible third energy level would be resolved easiest at magnetic fields beyond 25 T. However, we observe a minimum in PL intensity at this emission energy (arrow in Figure 5.3a) indicating the absence of this third peak.

The dependence of the calculated optical transition probabilities for the different excitonic states on applied magnetic field, shown in Figure 5.3a, does not manifest fluctuations, which could be related to bright-to-dark transitions [21].

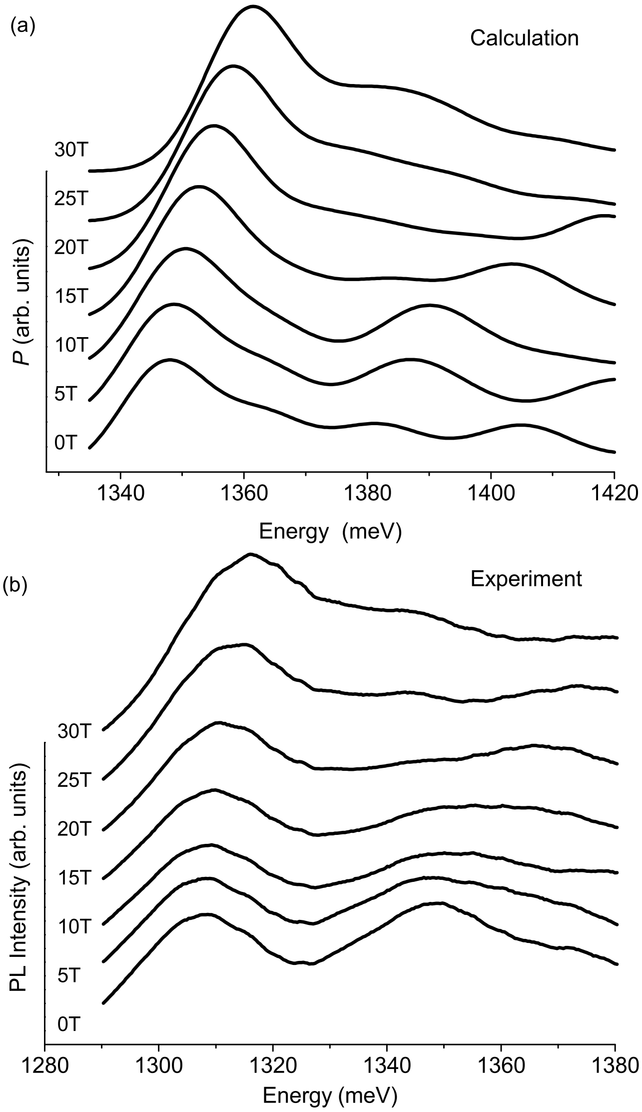

Figure 5.5: *(a) Calculated broadened optical transition probabilities P as a function of the emission energy E for B=0 to 30 T in 5 T steps. (b) The measured PL spectra for σ^- polarization in steps of 5 T.*

From the calculations the strongest effect on the oscillator strength is expected for the first excited state with predominantly a $l = 1$ character. However, this state we do not resolve in our measurements due to the inhomogeneous broadening.

The absence of the bright-to-dark transitions in the ground state energy of the calculated spectra has several reasons. Due to the relatively large heavy-hole mass, the size quantization energy of the heavy hole is relatively small. As a result of the level mixing due to the low symmetry of the quantum rings the splitting between the two lowest heavy-hole levels is in the order of 0.05 meV [30]. Therefore, the energy spacing between the lowest dark state and the lowest bright state cannot exceed 0.05 meV, which corresponds to a temperature of 2 K. Secondly, the Coulomb interaction modifies the exciton energy levels in such a way that the order of sequence of exciton states modifies, for some values of B . This can qualitatively be understood when taking into account that in structures with C_∞ or C_2 symmetry the lowest bright state corresponds to the same parity of the electron and hole wave functions, while the lowest dark state corresponds to different parity of the electron and hole wave functions. The efficiency of the Coulomb interaction is higher when the electron and hole wave functions have the same symmetry. As a result, the lowest dark state, which was the ground state in the absence of the Coulomb interaction, may have a higher energy than the lowest bright state in the case when the Coulomb interaction is switched on.

As can be inferred from the arguments given above, one hardly expects observable manifestations of the bright-to-dark transitions in the measured PL intensity. There are also practical reasons which make it even more difficult to observe these transitions. The magnetic fields corresponding to the bright-to-dark transition and a subsequent dark-to-bright transition, depend on various geometric parameters of the quantum ring. Therefore in an ensemble of quantum rings, even with a significant polarization of the exciton, at a given magnetic field both dark (in some rings) and bright (in other rings) states coexist due to the dispersion of geometric parameters of the quantum rings. As a consequence, the expected variation of the total PL intensity with the magnetic field may not reveal a strong and sharp bright-to-dark transition at all. Moreover, even dark excitonic states might appear in the quantum ring PL spectra due to phonon-assisted radiative transitions [31]. In an ensemble PL experiment, those contributions can not easily be distinguished from the contributions of the transitions involving the bright states because of the significant inhomogeneous broadening of the peaks.

In order to measure the excitonic AB effect in an ensemble of rings it would be necessary to decrease the inhomogeneity, which is hard to do, and increase the energy level separation between the ground state energy and the first excited state. The latter involves adjusting the growth parameters of quantum rings. The other approach to measure more precisely the emission energy of quantum rings and detect the excitonic AB effect is to measure the magnetoluminescence of individual quantum rings, which is the subject of the second part of this chapter. Moreover a charge-tunable quantum ring sample allows for the control of the charged state of the excitons in the ring [18], giving us the ability to study better the influence of the Coulomb interaction on the AB effect in these quantum rings. Nevertheless, even in the proposed single ring magnetoluminescence experiments it will be hard to detect bright-to-dark transitions. Sufficiently low temperatures and weak excitation densities are a necessary condition in order to observe these transitions.

Using our model we are able to understand the structure of the observed PL spectra on the basis of the calculated optical transition probabilities. The details of the calculated spectrum are very sensitive to the size, shape and composition of the quantum ring and it is therefore hard to find a quantitative agreement between the calculated optical transition probabilities and the measured PL spectra [22]. The model used does not include many-exciton complexes and charged excitonic states, which might influence the optical transition probability spectra. Finally, the optical transition probability spectrum is only an indication of how the PL spectrum would look like. In order to calculate the actual PL spectrum one needs to take in account a non-equilibrium distribution function for excitons in a strong laser field and use a response theory. Nevertheless, in spite of the preliminary character of our model, we are able to find a qualitative agreement between the measurements and the calculations and thereby we can explain the essential features in our measurements.

5.2.5 Conclusion

We have analyzed the emission energy of a large ensemble of self-assembled InAs/GaAs quantum rings in high magnetic fields, which reveals an excitonic behavior typical for rings. The optical transition probabilities are calculated within our model, based on the characterization of the realistic quantum ring. Comparing these calculations with our experimental data we find a qualitative agreement, which allows us to identify the different PL peaks and helps to explain the excitonic behavior in magnetic field. Experimentally we did not observe features of the AB effect in the excitonic ground and excited states. This indicates that the optical manifestation of the AB effect in these nanostructures is not detected within the experimental accuracy, in contrast to the electronic AB effect, which is observed in the magnetization experiments. Our model showed that the inclusion of the Coulomb interaction indeed results in the smooth dependence of the ground state emission energy on the magnetic field. Nevertheless, the ring character of our nanostructures results in the non-equidistant energy level splitting in the exciton diagram and into a magnetic field induced splitting of each excited state into two states. This is in contrast to what has been observed in the quantum dot measurements.

5.3 Single ring PL spectroscopy

The FWHM of the ensemble PL, shown in Figure 5.6, is 26 meV. In practice, this width hinders the observation of effects smaller than ≈ 1 meV. To observe effects on the μeV scale we have measured the emission of single InAs/GaAs quantum rings; a typical spectrum is also shown in Figure 5.6. The spectral width of a single ring is $\approx 0.1 - 0.2$ meV, thus the energy resolution is improved by two orders of magnitude.

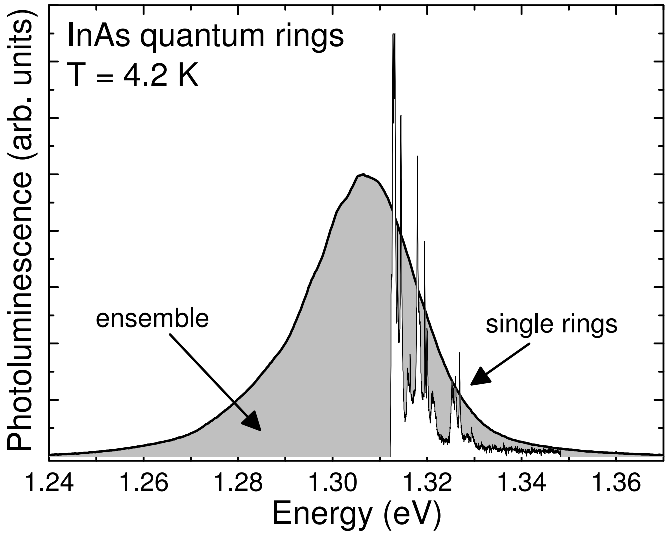

Figure 5.6: *Comparison of an ensemble PL spectrum with a spectrum of several single quantum rings at $T = 4.2\,K$, $B = 0$.*

5.3.1 Experimental details

The setup used for the single ring experiments is similar to the imaging setup described in Chapter 3. The excitation is provided by a HeNe laser emitting at 633 nm. The excitation power is $\approx 1\,\mathrm{mW/cm^2}$ and can be tuned by a Babinet-Soleil compensator, used as a half-wavelength plate, and two linear polarizers. To optimize the spectral resolution to $26\,\mu$eV and minimize the intensity losses in the detection path, we have decreased the magnification by a factor of three compared to the imaging setup in Chapter 3, using an f=300 mm lens. The total magnification of the setup is 65×. By making an image of the sample on the entrance slit of the spectrograph, we are able to separate the signal from different rings both spectrally and spatially, which enhances the ability to isolate the signal from a single ring and enables us to measure multiple ring spectra at the same time. The typical exposure time for one spectrum is 60 s. The magnetic field is applied parallel to the growth axis of the sample and the PL is measured in Faraday configuration. All measurements are performed at $T = 4.2\,\mathrm{K}$.

The sample consists of a single layer with a low density InAs/GaAs quantum rings ($n = 7 \times 10^9\,\mathrm{cm}^{-2}$, estimated from AFM measurements). This sample is from the same wafer as the sample used for the ensemble measurements, but has a lower ring density due to the indium gradient in the MBE chamber.

5.3.2 Experimental results

We have measured about 20 single rings up to a maximum magnetic field of 30 T. We were not able to measure all rings up to 30 T, since in some cases the position of the laser on the sample changed, due to movements of the probe induced by the magnetic field. In those cases the signal of the ring under investigation was lost. Figure 5.7 shows the energy of four quantum rings up to 30 T measured simultaneously. The different colors are representative for the intensity of the peaks. The spectral peaks are slightly asymmetric, which is an artefact of the experimental setup. The FWHM differs between different rings and is typical $\approx 0.1 - 0.2\,\mathrm{meV}$. In a magnetic field, we observe a quadratic diamagnetic shift of the PL emission and a Zeeman splitting of the emission peak into a doublet. This behavior is typical for all rings we have measured.

The value of the exciton g-factor g_{ex} and the diamagnetic coefficient α_d depend on the emission wavelength of the ring. For the rings shown in Figure 5.7 (emitting around 1.35 eV) we find $\alpha_d = 7.5\mu\,\mathrm{eV/T^2}$ and $g_{ex} = -2.7$. For a quantum ring emitting at lower energy (1.255 eV, not shown) we find $g_{ex} = -2.33$ and $\alpha_d = 8.16\mu\,\mathrm{eV/T^2}$. The sign of the g-factor is deduced by comparing our results to the ensemble measurements and to polarized data taken at lower

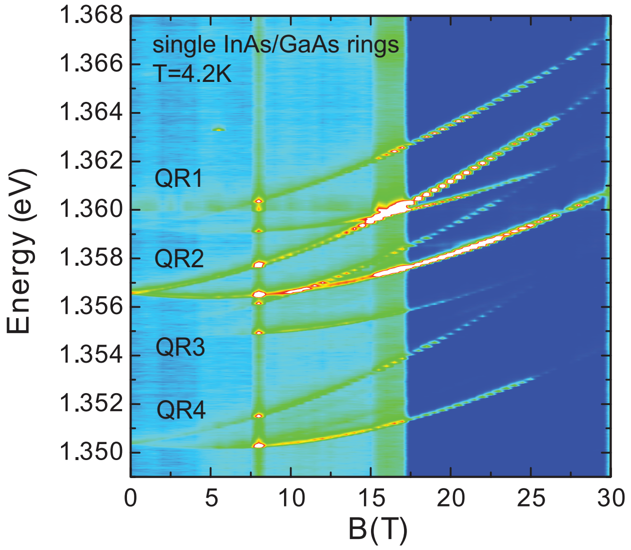

Figure 5.7: *Photoluminescence of four single InAs/GaAs quantum rings at $T = 4.2\,K$. Both circular polarizations are shown. The colors are representative for the intensity of the peaks in arbitrary units. At 6 T and 16 T the plot is rescaled to increase visibility.*

magnetic fields at the Technical University Eindhoven. The g-factor found for these single rings is about 1.5 times bigger than the g-factor measured for the ensemble, whereas the diamagnetic shift is slightly smaller. This could be due to inaccuracy in the determination of the peak position values for the ensemble measurements, due to the broad and asymmetric peak. Another reason could be that the rings used for the single ring experiments have a different composition, due to the indium gradient in the MBE chamber. For quantum dots it has been shown that the exciton g-factor is smaller for dots with a higher indium concentration, consistent with our findings and different from the composition dependence expected from bulk materials [32].

For two rings out of 20 we observe an additional peak appearing at the low energy side of both peaks of the Zeeman doublet, as shown in Figure 5.8. We do not know what is the nature of this peak and since we have no polarizers in our setup, we are not able to determine its polarization. A trivial reason of the appearance of this peak could be that it is emission from a nearby quantum ring, which moves into the detection focus. Also the additional peaks could be

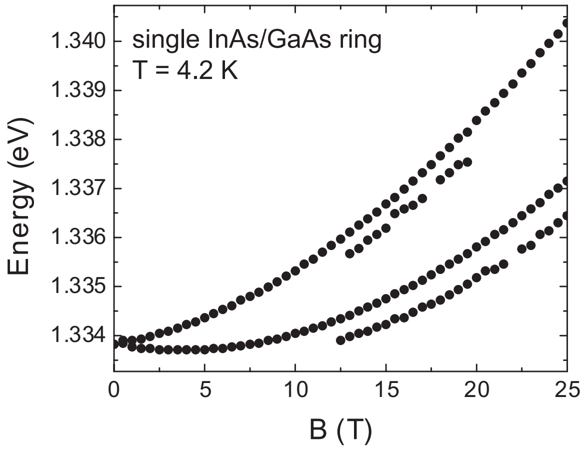

Figure 5.8: *Energy versus magnetic field a single InAs/GaAs quantum rings at $T = 4.2\,K$. Both circular polarizations are shown. Above 12 T an additional peak appears at the low energy side of both Zeeman components.*

related to mixing of dark and bright states [33], which causes the dark state to gain oscillator strength due to a magnetic field induced mixing with the bright states. The additional peak could as well be emission from charged complexes in the ring. For quantum dots it has been shown that a magnetic field applied parallel to the growth axis can influence the electron transport in the plane and change the charge state of the dot [34]. Finally we could attribute the peak to a crossing of energy levels related to the AB-effect. However, in the latter case we would expect a (anti-)crossing of energy levels, instead of a peak with a constant energy separation to the main peak.

As was the case for the ensemble measurements, also in the single ring experiments we do not observe any dark-to-bright transitions. This could be due to the limited accuracy with which we can measure the intensity of the PL. A more fundamental reason could be that the PL from the single rings is not arising from one energy level, but a mixture of states which become alternatively dark and bright. This is a realistic possibility since the width of the peaks ($\approx 0.1 - 0.2\,\text{meV}$) exceeds the level separation between exciton states ($0.05\,\text{meV}$).

5.3.3 Discussion

These measurements are the first observation of the exciton spectrum of single self-assembled quantum rings in high magnetic fields. We have measured about 20 single rings up to high fields, which is an experimentally challenging task. However we do not observe any clear features of the emission due to the ring geometry to which the excitons are confined. In the following we will suggest a number of improvements to the experiment which we need to conclusively map the exciton structure of quantum rings in a magnetic field.

The density of rings in our sample is still relatively high for a single-object experiment. Therefore we were only able to measure at the high- and low-energy side of the ensemble. This makes it impossible to systematically study the dependence of the g-factor and the diamagnetic shift on the emission energy. To lower the number of rings in the detection volume, we could use a solid-immersion lens, make masks on the sample or grow a sample with a lower density. Furthermore, for more precise measurements of the splitting we would need a system with a higher spectral resolution, with which we would also be able to measure the expected small asymmetry splitting at zero magnetic field.

While changing the magnetic field, the sample moves slightly. For this movements we correct by moving the sample with piezo-positioners and optimize the emission again. A drawback of this procedure is that we cannot quantitatively compare the intensity of the peak at different magnetic fields to observe an effect related to bright-to-dark transitions of the ground state [21]. Finally the experiment could be improved by using a gated sample to tune in a controlled way the charge state of the system [18].

5.3.4 Conclusion

We have measured the PL of single self-assembled InAs/GaAs quantum rings up to 30 T. We can accurately determine the diamagnetic coefficient and the g-factor of these rings. Furthermore, we observe an additional peak at the low-energy side of both Zeeman components, which might be related to the ring-like geometry of our nano-structures. However, a more quantitative analysis is difficult due to the low number of statistics and beyond the scope of this thesis.

References

[1] M. Bayer, O. Stern, P. H., Fafard, S., and Forchel, A. *Nature* **405**, 923 (2000).

[2] Warburton, R. J., Miller, B. T., Dürr, C. S., Bödefeld, C., K, Karrai, Kotthaus, J., Medeiros-Ribeiro, G., Petroff, P. M., and Huant, S. *Phys. Rev. B* **58**, 16221 (1998).

[3] Fock, V. *Z. Phys.* **47**, 446 (1928).

[4] Darwin, C. *Proc. Cambridge Philos. Soc.* **27**, 86 (1930).

[5] Babinski, A., Potemski, M., Raymond, S., Lapointe, J., and Wasilewski, Z. R. *Phys. Rev. B* **74**, 155301 (2006).

[6] Awirothananon, S., Raymond, S., Studenikin, S., Vachon, M., Render, W., Sachrajda, A., Wu, X., Babinski, A., Potemski, M., Fafard, S., Cheng, S. J., Korkusinski, M., and Hawrylak, P. *Phys. Rev. B* **78**, 235313 (2008).

[7] Hayden, R. K., Uchida, K., Miura, N., Polimeni, A., Stoddart, S. T., Henini, M., Eaves, L., and Main, P. C. *Physica B* **249**, 262 (1998).

[8] Raymond, S., Studenikin, S., Sachrajda, A., Wasilewski, Z., Cheng, S. J., Sheng, W., Hawrylak, P., Babinski, A., Potemski, M., Ortner, G., and Bayer, M. *Phys. Rev. Lett.* **92**, 187402 (2004).

[9] Blokland, J. H., Wijnen, F. J. P., Christianen, P. C. M., Zeitler, U., Maan, J. C., Kailuweit, P., Reuter, D., and Wieck, A. D. *Phys. Rev. B* **75**, 233305 (2007).

[10] Lévy, L. P., Dolan, G., Dunsmuir, J., and Bouchiat, H. *Phys. Rev. Lett.* **64**, 2074 (1990).

[11] Chandrasekhar, V., Webb, R. A., Brady, M. J., Ketchen, M. B., Gallagher, W. J., and Kleinsasser, A. *Phys. Rev. Lett.* **67**, 3578 (1991).

[12] D. Mailly, C. C. and Benoit, A. *Phys. Rev. Lett.* **70**, 2020 (1993).

[13] Fuhrer, A., Lüscher, S., Ihn, T., Heinzel, T., Ensslin, K., Wegscheider, W., and Bichler, M. *Nature* **413**, 822 (2001).

[14] García, J. M., Medeiros-Ribeiro, G., Schmidt, K., Ngo, T., Feng, J. L., Lorke, A., Kotthaus, J., and Petroff, P. M. *Appl. Phys. Lett.* **71**, 2014 (1997).

[15] Granados, D. and García, J. M. *Appl. Phys. Lett.* **82**, 2401 (2003).

[16] Aharonov, Y. and Bohm, D. *Phys. Rev.* **115**, 485 (1959).

[17] Kleemans, N. A. J. M., Bominaar-Silkens, I. M. A., Fomin, V. M., Gladilin, V. N., Granados, D., Taboada, A. G., García, J. M., Offermans, P., Zeitler, U., Christianen, P. C. M., Maan, J. C., Devreese, J. T., and Koenraad, P. M. *Phys. Rev. Lett.* **99**, 146808 (2007).

[18] Warburton, R. J., Schäflein, C., Haft, D., Bickel, F., Lorke, A., Karrai, K., Garcia, J. M., Schoenfeld, W., and Petroff, P. M. *Nature* **405**, 926 (2000).

[19] Haft, D., Schulhauser, C., Govorov, A. O., Warburton, R. J., Karrai, K., Garcia, J. M., Schoenfeld, W., and Petroff, P. M. *Physica E* **13**, 165 (2002).

[20] Grochol, M., Grosse, F., and Zimmermann, R. *Phys. Rev. B* **74**, 115416 (2006).

[21] Govorov, A. O., Ulloa, S. E., Karrai, K., and Warburton, R. J. *Phys. Rev. B* **66**, 081309(R) (2002).

[22] Fomin, V. M., Gladilin, V. N., Devreese, J. T., Kleemans, N. A. J. M., Bozkurt, M., and Koenraad, P. M. *Phys. Stat. Sol. (b)* **245**, 2657 (2008).

[23] Offermans, P., Koenraad, P. M., Wolter, J. H., Granados, D., García, J. M., Fomin, V. M., Gladilin, V. N., and Devreese, J. T. *Appl. Phys. Lett.* **87**, 131902 (2005).

[24] Walck, S. N. and Reinecke, T. L. *Phys. Rev. B* **57**, 9088 (1998).

[25] Schulhauser, C., Haft, D., Warburton, R. J., Karrai, K., Govorov, A. O., Kalameitsev, A. V., Chaplik, A., Schoenfeld, W., Garcia, J. M., and Petroff, P. M. *Phys. Rev. B* **66**, 193303 (2002).

[26] Bayer, M., Korkusinski, M., Hawrylak, P., Gutbrod, T., Michel, M., and Forchel, A. *Phys. Rev. Lett.* **90**, 186801 (2003).

[27] Fomin, V. M., Gladilin, V. N., Klimin, S. N., Devreese, J. T., Kleemans, N. A. J. M., and Koenraad, P. M. *Phys. Rev. B* **76**, 235320 (2007).

[28] Fomin, V. M., Gladilin, V. N., Devreese, J. T., Kleemans, N. A. J. M., and Koenraad, P. M. *Phys. Rev. B* **77**, 205326 (2008).

[29] Alén, B., Martínez-Pastor, J., Granados, D., and García, J. M. *Phys. Rev. B* **72**, 155331 (2005).

[30] Climente, J. I., Planelles, J., and Jaskólski, W. *Phys. Rev. B* **68**, 075307 (2003).

[31] Fomin, V. M., Gladilin, V. N., Devreese, J. T., Pokatilov, E. P., Balaban, S. N., and Klimin, S. N. *Phys. Rev. B* **57**, 2415 (1998).

[32] Nakaoka, T., Saito, T., Tatebayashi, J., and Arakawa, Y. *Phys. Rev. B* **70**, 235337 (2004).

[33] Bayer, M., Ortner, G., Stern, O., Kuther, A., Gorbunov, A. A., Forchel, A., Hawrylak, P., Fafard, S., Hinzer, K., Reinecke, T. L., Walck, S. N., Reithmaier, J. P., Klopf, F., and Schäfer, F. *Phys. Rev. B* **65**, 195315 (2002).

[34] Moskalenko, E. S., Larsson, L. A., Larsson, M., Holtz, P. O., Schoenfeld, W. V., and Petroff, P. M. *Phys. Rev. B* **78**, 075306 (2008).

Chapter 6

Shape and material dependent magnetic properties of colloidal nanocrystals

Abstract

In the first part of this chapter we show that small changes in the shape of colloidal CdSe nanocrystals have a dramatic effect on their magneto-optical properties. The photoluminescence emission energy of the two circular polarizations of quantum rods shows a giant splitting at 8 T, equivalent to an effective g-factor of -30, substantially larger than that of spherical quantum dots. We also find that the quantum-rod photoluminescence has a circular polarization opposite to that of quantum dots and is dominated by emission from higher lying exciton levels. We explain these findings by an empirical, effective-mass model for the exciton fine structure of quantum rods, in which the exciton levels are strongly mixed in a magnetic field. The second part of this chapter is devoted to the study of the polarized photoluminescence of spherical nanocrystals of different materials: CdSe, CdTe, PbSe and PbS. We show that the degree of circular polarization of their emission is remarkably similar, despite their very different crystal structure and electronic band structures.

6.1 Shape tuneable magneto-optical properties of colloidal nanocrystals

6.1.1 Introduction

Colloidal nanocrystals (NCs) are fabricated in a large variety by changing their composition, crystal structure, size, shape, strain and doping [1–7]. In this way the optical properties, such as emission wavelength and quantum yield can be tuned over a wide range and can be optimized for advanced applications [8, 9]. With increased control over the shape of the NCs during the synthesis, it is possible to grow one-dimensional (1D) CdSe nanorods (NQRs) which have shown relevant optical properties for applications, such as fast carrier dynamics [10–12] and linearly polarized emission [13–15]. Here we show that also the *magnetic* properties of these 1D NQRs differ significantly from those of spherical quantum dots (NQDs). We demonstrate that by changing the shape of the nanocrystal from 0D to 1D the splitting of the polarized components increases over an order of magnitude.

The magneto-optical response of NCs is understood in terms of their underlying exciton fine structure. Contrary to spherical CdSe nanocrystals (NQDs), which have been studied extensively in experiments [16–19] and theory [20–23] the exciton fine structure of NQRs is not yet fully characterized. Due to the electron-hole exchange interaction and the intrinsic crystal/shape anisotropy, the spin degeneracy of the exciton ground state in a NC is lifted, leading to five different states labeled by their spin projection (F) along the NC c-axis. The character of the NC ground state is calculated to be strongly dependent on its size and shape, having a heavy-hole character in NQDs and a light-hole character in elongated NQRs [24, 25].

In this paper we investigate the energy levels of the exciton fine structure of NQRs by using a strong magnetic field. We compare the magneto-optical properties of CdSe NQRs under resonant and non-resonant excitation with those of NQDs. Under non-resonant excitation the excitation energy is much higher than the energy of emitting levels. Therefore we are able to see the higher energy levels [10]. Under resonant excitation we only measure the lowest energy levels [17]. The photoluminescence (PL) of NQRs shows a giant splitting of the two circular polarizations at a magnetic field of 8 T, which corresponds to an effective g-factor of -30. Until now such large Zeeman splittings have only been observed in quantum dots doped with magnetic ions, due to the enhancement of the magnetic $sp-d$ interaction [7,26]. For NQDs a g-factor in the order of unity has been found [18,19], which is comparable to the g-factor found in epitaxially grown quantum dots [27–29]. Also the degree of circular polarization (DCP) of the NQRs is opposite to the DCP of the NQDs [19,30]. The large effective g-factor of NQRS is shown not to arise from single exciton levels, but can be explained satisfactorily by a strong mixing of the exciton levels influenced by the magnetic field.

6.1.2 Experimental details

The synthesis of the CdSe NCs used in this study is described elsewhere [31]. The NCs are capped with tri-n-octylphosphine oxide (TOPO) and hexadecylamine (HDA) to passivate the surface, increasing the quantum yield and providing solubility. An initial characterization has been done using transmission electron microscopy (Figure 6.1a). From this image we find a length of 10.7 ± 3.8 nm and a radius of 1.85 ± 0.52 nm. From these dimensions a mean aspect ratio, defined as the ratio of length and diameter, of 2.9 is extracted. The NQDs we have used have a comparable radius of 1.78 nm and their full magneto-optical characterization has been reported in ref. [19].

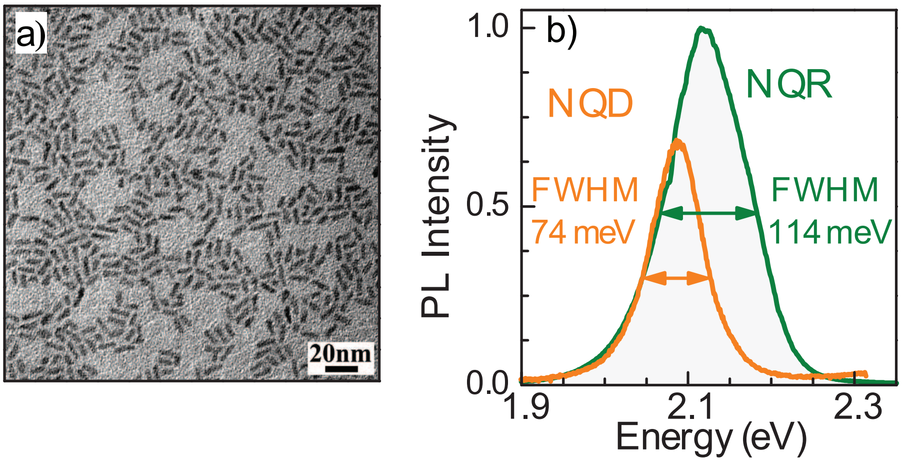

Figure 6.1: *(a) TEM image of CdSe colloidal NQRs. (b) Non-resonant PL spectra of CdSe NQDs and NQRs at $B = 0$ T and $T = 4.2$ K.*

We have performed magneto-PL measurements at low temperatures (4.2-1.2 K). The PL measurements performed under non-resonant excitation were performed with a standard PL setup using lenses. A quarter waveplate and a polarizing beamsplitter allowed for the simultaneous recording of both circular polarizations. For the fluorescence line narrowing (FLN) measurements, i.e. PL measurements using resonant excitation, the sample was mounted on a fibre coupled probe, in which excitation light from a tuneable dye-laser is coupled to the sample with fibers. The light is polarized by a circular polarizer and is focussed on the sample by a lens. The PL of the sample is then collected by a spherical mirror, analyzed by a second circular polarizer and focussed into the detection fibre. The light is dispersed by a single grating spectrograph and detected by a LN cooled CCD camera. All experiments are performed in a 33 T Bitter magnet in Faraday geometry.

Figure 6.1b shows the PL spectra of a NQR and a NQD sample, prepared by drop-casting a solution of NCs in toluene on a GaAs substrate. The PL of the NQRs (NQDs) at $T = 4.2\,\mathrm{K}$ is centered around 2.121 eV (2.086 eV) and has a Full-Width-at-Half-Maximum (FWHM) of 114 meV (74 meV). The larger FWHM of the NQR PL is most probably due to the larger size dispersion of the NQRs and to excited states contributing to the PL [10].

6.1.3 Experimental results

Figures 6.2a and 6.2b show the PL peak energy and intensity respectively of spectra recorded at $T = 1.2\,\mathrm{K}$ in magnetic fields up to 33 T. In general we find that with increasing magnetic field the σ^- (σ^+) polarized peak shifts rapidly to higher (lower) energy up to $B = 8\,\mathrm{T}$. When the magnetic field is increased further, the energy of the σ^- polarized peak decreases again, whereas the energy of the σ^+ polarized peak slightly increases. The normalized PL intensity of the σ^- polarized peak decreases up to around 15 T, when it levels off. The σ^+ polarized PL intensity initially drops, but then steadily increases.

The behavior of the NQR magneto-PL is strikingly different from that of NQDs [19] (Figure 6.2c and 6.2d). The energy splitting $\Delta E = E_{\sigma^-} - E_{\sigma^+}$ of the NQRs increases to 10 meV at 8 T, after which it decreases. We define the effective g-factor as

$$g = -\frac{\Delta E}{\mu_B B}, \tag{6.1}$$

where μ_B is the Bohr magneton. For the NQRs we find an effective g-factor which is magnetic-field dependent and has a maximum of -30. This is in marked contrast to the small and constant g-factor found for NQDs (cf. Figure 6.2c). Surprisingly, the DCP, calculated as

$$\mathrm{DCP} = \frac{I_{\sigma^-} - I_{\sigma^+}}{I_{\sigma^-} + I_{\sigma^+}}, \tag{6.2}$$

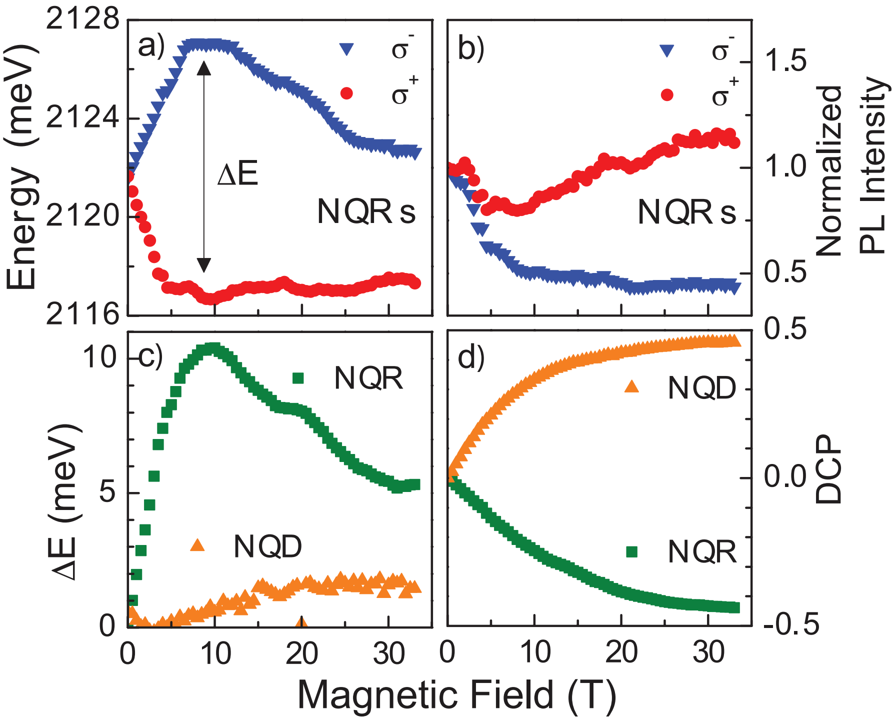

Figure 6.2: *Non-resonant polarized PL data at $T = 1.2\,K$ and $B = 0 - 33\,T$. (a) PL energy for NQRs (b) Normalized PL intensity for NQRs. The blue triangles (red circles) correspond to σ^- (σ^+) polarized light. (c) Energy splitting $\Delta E = E_{\sigma^-} - E_{\sigma^+}$ between the two circular polarizations for NQRs and NQDs. (d) Degree of circular polarization for NQRs and NQDs. The green squares (orange triangles) correspond to the NQRs (NQDs).*

for the NQRs increases monotonously, comparable in amplitude to that of the NQDs, but opposite in sign (cf. Figure 6.2d).

We have performed FLN measurements to have direct access to the lowest levels of the NC exciton fine structure, which are schematically shown in the inset of Figure 6.3 for NQDs (left) and NQRs (right). The bright $F = \pm 1$ levels are similar for both NCs, but the expected ground state has a different character: a dark, polarized $F = \pm 2$ state for the NQDs and a dark, unpolarized $F = 0^L$ state for the NQRs [24,25,32]. The spin-splitting between the two bright exciton states is indicated by Δ_{ss}; the splitting between the bright exciton state and the zero phonon line is indicated by Δ_1.

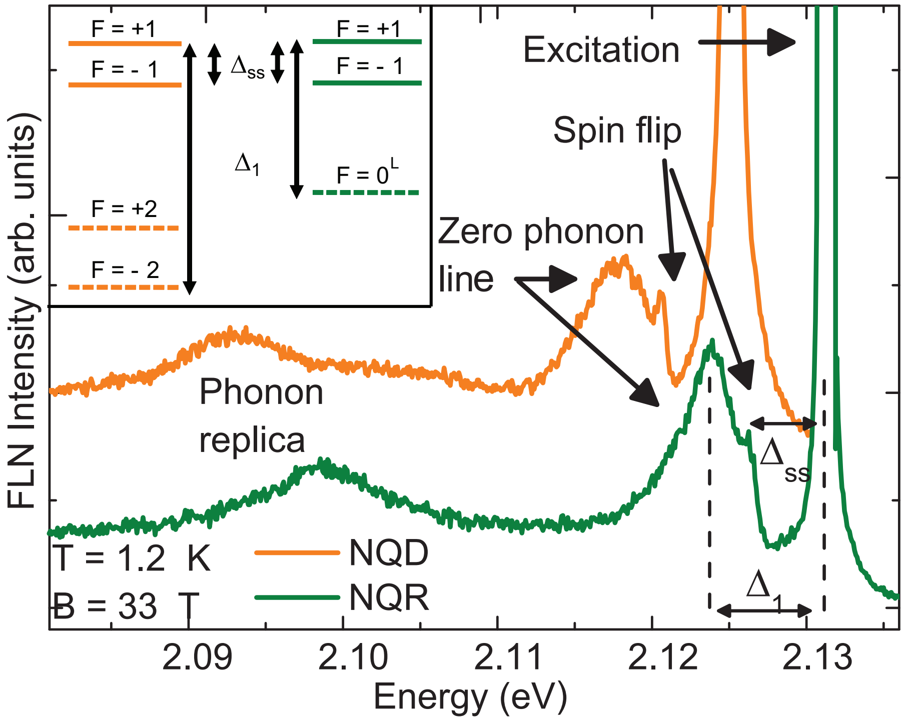

Figure 6.3: *FLN spectrum of NQDs (upper spectrum) and NQRs (lower spectrum) at $T = 1.2$ K and $B = 33$ T. The sample is excited with σ^+ polarized light, the PL is detected in σ^- polarization. The energy splittings between the excitation and the ZPL emission from the ground state (Δ_1) and between the excitation and the resonant spin-flipped state (Δ_{ss}) are indicated. The inset shows the lowest exciton levels of the NQDs (left panel) and the NQRs (right panel)*

The FLN spectra of NQRs (lower spectrum) and NQDs (upper spectrum) at $T = 1.2\,\mathrm{K}$ and $B = 33\,\mathrm{T}$ for one cross-circular polarization (σ^+ excitation, σ^- detection) are shown in Figure 6.3a. Despite the difference in NC shape, both FLN spectra look similar [17, 19]. The Lorentzian shaped laser line, visible on the right hand side, is in resonance with a bright $F = +1$ exciton level. To the left of the laser line we resolve the spin-flipped $F = -1$ bright exciton level, the zero phonon line (ZPL) of the dark exciton ground state and its first Gaussian shaped, phonon replica. All peaks are superimposed on a small broad Gaussian background.

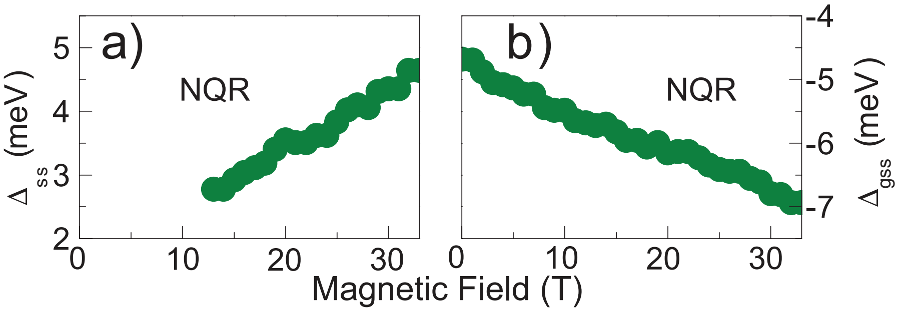

Figure 6.4: *(a) The energy splitting (Δ_{ss}) between the two bright $F = \pm 1$ states of the NQRs. (b) The shift of the $F = 0^L$ ground state of the NQRs. Δ_{gss} is defined as the average of Δ_1 for the two cross-circular polarizations.*

The FLN spectra in magnetic fields $B = 0 - 33$ T of the NQRs are analyzed by fitting each peak to its appropriate profile. The spin-splitting between the two bright states, Δ_{ss} (Figure 6.4a) can only be determined above 14 T when the spin-flipped transition is observed. By extrapolating we find a zero-field splitting of the bright states of 1.5 meV and an exciton g-factor of 1.7, comparable to the g-factor of the NQD bright states, which is 1.8. The shift of the ground state Δ_{gss} (Figure 6.4b) is extracted by measuring the energy difference between the bright and dark exciton levels Δ_1 in both cross-circular polarization schemes. The energy of the ground state is measured with respect to the middle of the $F = \pm 1$ states and shifts from -4.5 meV at 0 T to -7 meV at 30 T.

6.1.4 Discussion

In the remainder of the paper we will describe both our non-resonant and resonant PL results in terms of the exciton fine structure of NQRs. Because the NQR exciton fine structure has not yet been calculated in a magnetic field, we use an empirical model (shown in Figure 6.5) based upon the zero-field model of Efros et al. within the framework of the effective-mass approximation (EMA) [24,32]. The four lowest-lying states have mainly a light-hole (LH) character ($F = 0^L, \pm 1, 0^U$ in order of increasing energy), because the 1D symmetry of the NQRs causes the light holes to shift up in energy [24, 25]. Three of the LH excitons are bright and one is dark, due to the optical selection rules for circularly polarized light (solid (dashed) lines indicate bright (dark) exciton states in Figure 6.5). Both $F = 0$ states have bright, linearly polarized components, since the long axis of the rods is perpendicular to the direction of the light. For the $F = 0^U$ state these components interfere constructively, adding oscillator strength, whereas for the $F = 0^L$ state they interfere destructively, causing this state to be dark at $B = 0\,\mathrm{T}$. At higher energy there are four states with a heavy hole (HH) character ($F = \pm 2, \pm 1$) of which we take only into account the lower lying (dark) $F = \pm 2$ states.

The magnetic field dependence of the exciton levels now follows from our PL and FLN data. The behavior of the bright $F = \pm 1$ states we directly extract from Δ_{ss} measured by FLN (Figure 6.4a). The shift of the ground state Δ_{gss} (Figure 6.4b) is also directly measured, assuming that the average energy of the $F = \pm 1$ states is constant.

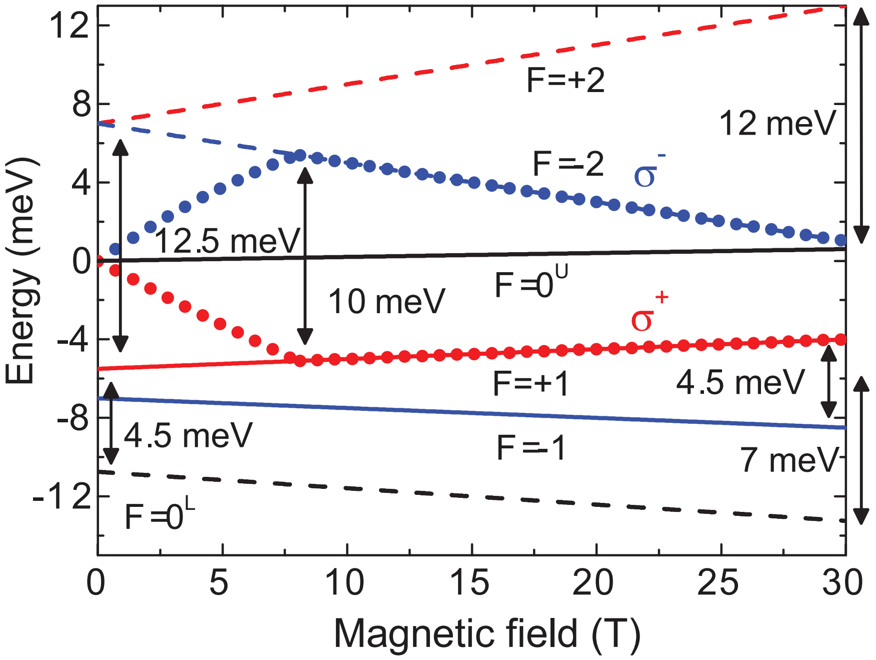

Figure 6.5: *Exciton fine structure model for NQRs. The round symbols are a guide to the eye to indicate the ensemble PL. The solid (dashed) lines represent bright (dark) exciton states. The color of the lines represents the majority circular polarization, where blue (red) indicates* σ^- *(*σ^+*) polarization.*

The intriguing behaviour of the non-resonant PL is more difficult to understand. The most striking feature is the giant energy splitting between the two circular components, which is much larger than the Zeeman splittings of the individual exciton levels. This implies that, unlike the FLN emission, the PL is not merely determined by the lowest exciton levels, but rather by the combined recombination of all exciton levels.

For instance, at $B = 0$ the emission is predominantly determined by the bright, higher lying $F = 0^U$ level, since it has four times more oscillator strength than the bright $F = \pm 1$ levels [20,24,32]. In addition, the relative contributions of the different exciton levels to the total non-resonant PL strongly depends on the magnetic field, as a result of the field-induced mixing between the bright and dark single exciton levels [16, 20, 30]. This mixing depends on the angle between the long axis of the NQRs and the magnetic field, and is strongest for angles of 90°, which is our experimental situation, since all the NQRs have their long axis parallel to the surface (cf. Figure 6.1a). Invoking this mixing results in a PL energy (solid symbols in Figure 6.5) consistent with the experimentally determined PL (Figure 6.2a). With increasing magnetic field the unpolarized $F = 0^U$ level mixes with the $F = -2$ ($F = +1$) level in σ^- (σ^+) polarization. Until 8 T the PL is determined by a mixture of aforementioned levels, which in Figure 6.5 is represented by a linear combination of the energy of both levels. For higher magnetic fields the non-resonant emission is mainly determined by the $F = -2$ and $F = +1$ levels. From the shift of the σ^- polarized level we infer that this level is not the ground state, but has a higher energy than the unpolarized $F = 0$ states. Since there is only one $F = |2|$ state in the exciton fine structure, we have strong evidence that the ground state of NQRs does not have an $F = |2|$ like the NQDs.

The DCP of the NQRs is opposite to that of the NQDs. The latter was explained satisfactorily by invoking exciton mixing and taking an average over different angles of the crystal *c*-axis and the magnetic field [19, 30]. By the same arguments we expect for NQRs the lower-lying σ^+ state having more intensity, since it is a mixture of two bright states, whereas the σ^- polarization is a mixture of one bright and one dark state. Furthermore the energy of the σ^+ polarized level is lower and therefore might have a higher population, although in non-resonant PL we cannot assume a purely thermal distribution. Our proposed schematic model catches the essential features, i.e. the energy shifts and polarization, of both resonantly and non-resonantly excited magneto-PL. A full quantitative description, which answers why the splitting of the polarized components is maximal at 8 T and includes the intensity of the PL, would require a dedicated theoretical model.

6.1.5 Conclusion

From resonant and non-resonant magneto-PL experiments on CdSe NCs we find that the change of shape of colloidal nanocrystals from zero- to one-dimensional has a dramatic effect on their magneto-optical properties. For the 1D NQRs we observe an energy splitting of the two circularly polarized components, equivalent to a g-factor of -30. We find that the NQR PL has DCP opposite to the NQDs and is dominated by emission from higher lying exciton levels, strongly mixed in a magnetic field. The exciton ground state of the system is an unpolarized dark $F = 0$ state with a LH character, as expected for 1D NCs. We propose a empirical model for the exciton fine structure of NQRs within the EMA. This shape-dependent behavior of the spin polarized exciton levels opens a new route for spin-based applications of semiconductor nanocrystals.

6.2 Material-dependent circular polarization in high magnetic fields

6.2.1 Introduction

As noted in the first part of this Chapter, the properties of colloidal NCs can easily be varied by changing their composition, crystal structure, size, shape, strain and doping. Here we study the influence of the constituting material on the circular polarization of NQDs in high magnetic fields. We compare cadmium-telluride (CdTe) and cadmium-selenide (CdSe) NQDs, having a very similar exciton fine structure (cf. Figure 2.5) and lead-sulfide (PbS) and lead-selenide (PbSe) NQDs. PbS and PbSe NQDs are IV-VI nanocrystals with a narrow energy gap, relevant for optical applications in the near-infrared region of the optical spectrum such as long wavelength (1.3 and 1.55 μ m) telecommunication [33] and photovoltaics because of their efficient multiple exciton generation [34]. Lead salts crystallize in the cubic sodium chloride structure having a high symmetry. Furthermore the sizes of the lead nanocrystals we have used in this study are much smaller than their exciton radius (cf. Table 2.1). Their valence band structure, with the direct minimum at the L-point in the Brioullin zone, is completely different from CdSe and CdTe, having a direct optical gap at the Γ-point. Therefore we expect the optical properties of the lead salt nanocrystals to be very different from those of the nanocrystals formed from cadmium alloys.

However, we find that the degree of circular polarization (DCP) does not conclusively depend on the material nor on the size of the NQDs. This is demonstrated by the comparison of the DCP at $T = 4.2\,\mathrm{K}$ of CdSe, CdTe, PbSe and PbS NQDs an by comparing the temperature-dependent DCP of PbS NQDs with the results found in literature for CdSe.

6.2.2 Experimental details

The PL spectra of the five samples we have studied are shown in Figure 6.6. The material properties of the semiconductors used are given in Table 2.1. The CdSe and CdTe NQDs are dissolved in toluene, the PbS NQDs are in an aqueous solution and the PbSe NQDs are dissolved in trichloroethylene (TCE). The widths of the spectra of the different NQDs, obtained by a Gaussian fit, are comparable and range from $\sigma = 60\,\text{meV}$ for the CdSe NQDs with a radius $d = 3.7\,\text{nm}$ to $94\,\text{meV}$ for the CdTe NQDs.

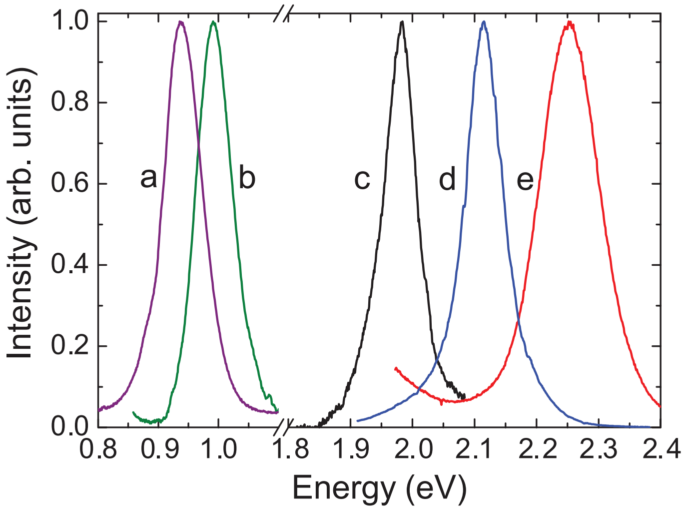

Figure 6.6: *Photoluminescence spectra of several colloidal quantum dots. $T = 4.2\,\text{K}$. a) PbS $r = 4.5\,\text{nm}$, b) PbSe $r = 1.5\,\text{nm}$, c) CdSe $r = 3.7\,\text{nm}$, d) CdSe $r = 1.8\,\text{nm}$, e) CdTe $r = 1.7\,\text{nm}$.*

To determine the polarized emission in magnetic fields, we have dropcasted the samples on a Si/SiO$_2$ substrate (glass for the PbS NQDs). It is important to note that we can only detect polarized light from dropcasted samples and solutions which are unfrozen or freeze transparently. When the solution becomes non-transparent, the detection of the polarization is hindered due to scattering in the sample.

We have performed magneto-PL measurements in Faraday configuration up

	Material	d (nm)	E (eV)	σ (meV)	DCP @ 10 T
a	PbS	4.5	0.94	60	0.16
b	PbSe	1.5	0.99	61	0.42
c	CdSe	3.7	1.98	60	0.38
d	CdSe	1.8	2.21	67	0.21
e	CdTe	1.7	2.25	94	0.18

Table 6.1: *Radius r, emission energy E, width σ and DCP at $B = 10$ T of the NQDs investigated in this paragraph. All spectra are taken at $T = 4.2$ K.*

to 30 T at variable temperatures (120-4.2 K), with a standard PL setup using lenses. The excitation was provided by a solid state laser operating at 532 nm. The luminescence was dispersed by a single grating spectrometer (300 g/mm grating, f=30 cm) and recorded by a LN-cooled CCD camera for the CdSe and CdTe NQDs. For the PbSe and PbS NQDs the PL was dispersed by a 150 g/mm grating and recorded by a LN-cooled InGaAs array.

6.2.3 Experimental results

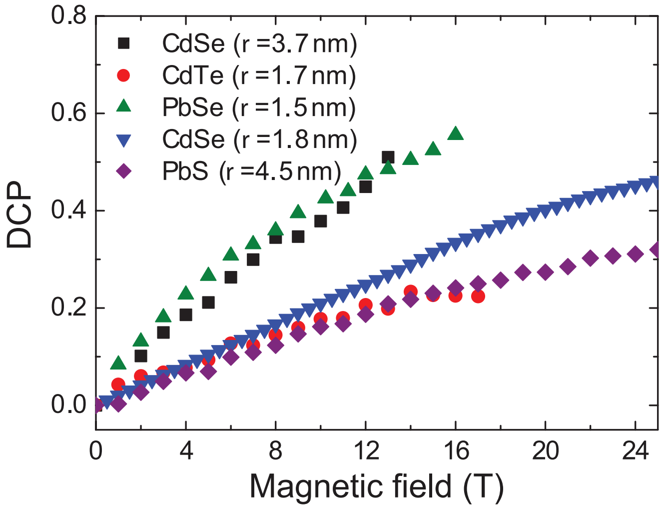

Figure 6.7: *Degree of circular polarization of several colloidal quantum dots. $T = 4.2$ K.*

The DCP of the five NQD samples is shown in Figure 6.7. The DCP has the same sign for all samples, contrary to the one-dimensional NQRs studied in the first part of this Chapter. However, the DCP does not show a consistent trend nor in material type, nor in crystal structure, nor in size. This suggests that there are other factors determining the polarized emission of these nanostructures.

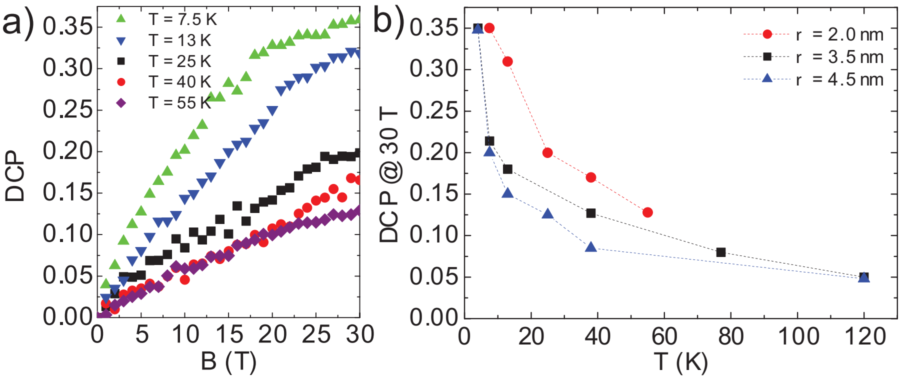

Figure 6.8: *a) Temperature dependent DCP for PbS NQDs with $r = 2.0$ nm. b) DCP at $B = 30$ T for PbS NQDs with $r = 2.0, 3.5, 4.5$ nm.*

Figure 6.8 shows the temperature dependent DCP for PbS NQDs of different sizes. The DCP decreases with increasing temperature and reduces to zero within the experimental accuracy around $T = 120\,\mathrm{K}$. In a simple model, where we assume the carriers are thermally distributed over the energy levels, the DCP is given by the Boltzmann distribution

$$\frac{1+\mathrm{DCP}}{1-\mathrm{DCP}} = \exp\left(-\frac{\Delta E}{k_B T}\right) \tag{6.3}$$

We thus expect indeed that the DCP decreases with increasing temperature. At 120 K $k_B T = 10\,\mathrm{meV}$ is much larger than the splitting of the polarized levels, which is zero within the experimental accuracy of $\approx 1\,\mathrm{meV}$. However, we cannot satisfactorily fit the temperature dependent curves in Figure 6.8 with an exponential decay having the same energy separation Δ for all temperatures. This indicates that the polarization is not solely determined by a thermal distribution of carriers over two polarized energy levels.

6.2.4 Discussion and conclusion

From the experimental results we cannot determine the mechanisms which give rise to the circular polarized emission of colloidal nanocrystals. We do observe, however, that nor the material, nor the size of the dots plays a major role. In the previous paragraph of this chapter, we have already shown that the shape of the nanocrystal is an important factor. Furis *et al.* [30] observed a similar temperature dependence of the DCP of CdSe NQDs with a radius of 1.3 nm as we observe for the PbS NQDs. The authors explain their results invoking the random orientation of the NQD *c*-axis with respect to the magnetic field. However, in rock-salt nanocrystals there is no *c*-axis present due to the cubic symmetry of the lattice.

Other possible mechanisms causing the polarized emission are the dielectric screening of the surrounding medium [35, 36] and the influence of the surface ligands [37]. Therefore a systematic study of the influence of the substrate onto which the samples are dropcasted and of surface ligands is necessary to find the mechanism behind the polarized emission of colloidal NQDs.

In conclusion, we have studied the DCP of NQDs of several different materials at low temperatures and the temperature dependence of the DCP of PbS NQDs. Surprisingly we do not observe striking differences between the PbS and PbSe dots on the one hand and CdSe and CdTe dots on the other hand. This observation is in strong contrast to what is expected from the exciton fine structure models. This suggests that the polarized emission of NQDs is not only determined by the size or bandstructure of the NQDs themselves, but also their surroundings, as the dielectric medium and surface ligands dominate the emission process.

References

[1] Kan, S., Mokari, T., Rothenberg, E., and Banin, U. *Nature Materials* **2**, 155 (2003).

[2] Milliron, D. J., Hughes, S. M., Cui, Y., Manna, L., Li, J., Wang, L.-W., and Alivisatos, A. P. *Nature* **430**, 190 (2004).

[3] Peng, X., Manna, L., Yang, W., Wickham, J., Scher, E., Kadavanich, A., and Alivisatos, A. P. *Nature* **404**, 59 (2000).

[4] Manna, L., Scher, E. C., and Alivisatos, A. P. *J. Am. Chem. Soc.* **122**, 12700 (2000).

[5] Smith, A. M., Mohs, A. M., and Nie, S. *Nature Nanotechnology* **4**, 56 (2009).

[6] Erwin, S. C., Zu, L., Haftel, M. I., Efros, A. L., Kennedy, T. A., and Norris, D. J. *Nature* **436**, 91 (2005).

[7] Bussian, D. A., Crooker, S. A., Yin, M., Brynda, M., Efros, A. L., and Klimov, V. I. *Nature Materials* **8**, 35 (2009).

[8] Klimov, V., Mikhailovsky, A., Xu, S., Malko, A., Hollingsworth, J., Leatherdale, C., Eisler, H., and Bawendi, M. *Science* **290**, 314 (2000).

[9] Leuenberger, M. and Loss, D. *Nature* **410**, 789 (2001).

[10] Mohamed, M. B., Burda, C., and El-Sayed, M. A. *Nano Letters* **1**, 589 (2001).

[11] Scholes, G. D., Kim, J., Wong, C. Y., Huxter, V. M., Nair, P. S., Fritz, K. P., and Kumar, S. *Nano Letters* **6**, 1765 (2006).

[12] Achermann, M., Bartko, A. P., Honningsworth, J. A., and Klimov, V. I. *Nature Physics* **2**, 557 (2006).

[13] Hu, J., Li, L.-s., Yang, W., Manna, L., Wang, L.-w., and Alivisatos, A. P. *Science* **292**, 2060 (2001).

[14] Li, L.-s. and Alivisatos, A. P. *Phys. Rev. Lett.* **90**, 097402 (2003).

[15] Thomas, N. L., Herz, E., Schops, O., Woggon, U., and Artemyev, M. V. *Phys. Rev. Lett.* **94**, 016803 (2005).

[16] Nirmal, M., Norris, D. J., Kuno, M., Bawendi, M. G., Efros, A. L., and Rosen, M. *Phys. Rev. Lett.* **75**, 3728 (1995).

[17] Furis, M., Htoon, H., Petruska, M. A., Klimov, V. I., Barrick, T., and Crooker, S. A. *Phys. Rev. B* **73**, 241313 (2006).

[18] Htoon, H., Crooker, S. A., Furis, M., Jeong, S., Efros, A. L., and Klimov, V. I. *Phys. Rev. Lett.* **102**, 017402 (2009).

[19] Wijnen, F. J. P., Blokland, J. H., Chin, P. T. K., Christianen, P. C. M., and Maan, J. C. *Phys. Rev. B* **78**, 235318 (2008).

[20] Efros, A. L., Rosen, M., Kuno, M., Nirmal, M., Norris, D. J., and Bawendi, M. *Phys. Rev. B* **54**, 4843 (1996).

[21] Efros, A. L. and Rosen, M. *Ann. Rev. Mater. Sci.* **30**, 475 (2000).

[22] Zhang, X. W. and Xia, J. B. *Phys. Rev. B* **72**, 075363 (2005).

[23] Califano, M., Franceschetti, A., and Zunger, A. *Phys. Rev. B* **75**, 115401 (2007).

[24] Shabaev, A. and Efros, A. L. *Nano Letters* **4**, 1821 (2004).

[25] Zhao, Q., Graf, P. A., Jones, W. B., Franceschetti, A., Li, J., Wang, L. W., and Kim, K. *Nano Letters* **7**, 3274 (2007).

[26] Kudelski, A., Lemaître, A., Miard, A., Voisin, P., Graham, T. C. M., Warburton, R. J., and Krebs, O. *Phys. Rev. Lett.* **99**, 247209 (2007).

[27] Bayer, M., Kuther, A., Forchel, A., Gorbunov, A., Timofeev, V. B., Schäfer, F., Reithmaier, J. P., Reinecke, T. L., and Walck, S. N. *Phys. Rev. Lett.* **82**, 1748 (1999).

[28] Alegre, T. P. M., Hernández, F. G. G., Pereira, A. L. C., and Medeiros-Ribeiro, G. *Phys. Rev. Lett.* **97**, 236402 (2006).

[29] Pryor, C. E. and Flatté, M. E. *Phys. Rev. Lett.* **96**, 026804 (2006).

[30] Furis, M., Hollingsworth, J. A., Klimov, V., and SA, C. *J. Phys. Chem. B* **109**, 15332 (2005).

[31] Chin, P., Hikmet, R., Meskers, S., and Janssen, R. *Adv. Funct. Mater.* **17**, 3829 (2007).

[32] Shabaev, A. and Efros, A. L. *Private communication* (2008).

[33] Schaller, R. D., Petruska, M. A., and Klimov, V. I. *Journal of Phys. Chem. B* , 13765 (2003).

[34] Ellingson, R. J., Beard, M. C., Johnson, J. C., Yu, P., Micic, O. I., Nozik, A. J., Shabaev, A., and Efros, A. L. *Nano Letters* **5**, 865 (2005).

[35] Harbold, J. M. and Wise, F. W. *Phys. Rev. B* **76**, 125304 (2007).

[36] Climente, J. I., Royo, M., Movilla, J. L., and Planelles, J. *Phys. Rev. B* **79**, 161301 (2009).

[37] Guyot-Sionnest, P., Wehrenberg, B., and Yu, D. *Journal Chem. Phys.* , 074709 (2005).

Chapter 7

Optical probing of electronic fractional quantum Hall states

Abstract

We report the observation of a fine structure in the photoluminescence emission of high mobility GaAs/AlGaAs single heterojunctions in the fractional quantum Hall regime. A splitting of the emission peak into three lines is found both at filling factor $\nu = 2/3$ and in the region $1/3 < \nu < 2/5$. The dependencies on magnetic field strength, electron density and temperature show that the fine structure arises from recombination of fractionally-charged elementary excitations of the two-dimensional electron liquid and a photo-excited valence band hole. These quasi-particle excitations have a dispersion relation with a minimum at finite momentum, confirming a long-standing theoretical prediction.

7.1 Introduction

Electron-electron interactions in a two-dimensional electron gas (2DEG) in a strong magnetic field (B) give rise to highly correlated electron states, the so-called fractional quantum Hall effect (FQHE) [1]. At fractional filling factors

$$\nu = \frac{1}{q}\ (\nu = 2\pi n_e l_B^2), \tag{7.1}$$

with $l_B = \sqrt{\hbar/eB}$ is the magnetic length and n_e is the electron density, the electrons form an incompressible quantum liquid (IQL) [2–4]. The elementary excitations of the IQL are quasi-electrons (QEs) and quasi-holes (QHs) with a fractional charge and a finite excitation energy [2–4]. The existence of fractionally charged quasi-particles has been first demonstrated by magnetotransport experiments [1,4] and later on by shot noise [5,6] and cyclotron resonance [7,8] measurements. Anomalies in the photoluminescence (PL) of a 2DEG in the FQH regime with photo-excited holes also evidence correlated electron states [9–16], although the detailed nature of these anomalies is still not fully understood.

The origin of the PL of 2D systems, such as quantum wells (QWs) and heterojunctions (HJs), in the FQH regime depends strongly on the relative strength of the electron-electron (*e*-*e*) and electron-hole (*e*-*h*) interactions [17–24]. When the distance d between the electron and hole confinement layers is small, like in most QW systems that have been studied, the strength of the *e*-*e* and *e*-*h* interactions is comparable. In this case the electron correlations are strongly affected by the photo-injected valence band holes and the PL emission is determined by neutral and charged excitons, rather than by the correlated 2DEG itself [17–21, 23, 24]. This has led to a wide variety of PL features: at low electron densities n_{2D} distinct PL peaks are due to neutral and charged excitons that can be regarded isolated from the 2DEG [25]. At higher density the (charged) excitons interact with correlated 2DEG, most often leading to doublets in the PL emission and distinct jumps in the PL peak energy at fractional filling factors [9, 10, 16].

In this chapter we study a different regime in which the *e*-*e* correlations are probed optically by using the 2DEG of high-quality single GaAs/AlGaAs HJs. The internal electric field in a HJ results in a large electron-hole separation and, therefore, a strongly reduced *e*-*h* interaction. Measurements of high density HJs in the FQH regime are remarkably scarce, and limited to the detection of PL anomalies at integer filling factors [26–28] and a doublet structure at $\nu = 2/3$ [11]. Theoretically, a multiple PL line structure is predicted when $d >> l_B$ arising from the radiative recombination of a photo-excited valence hole with several fractionally charged excitations of the 2DEG [17–21, 23, 24, 29, 30].

We report the observation of a triplet fine structure in the PL spectra around both $\nu = 2/3$ and $1/3$. By using HJs with different 2DEG densities we find that the energy splittings of the PL fine structure around $\nu = 1/3$ scale with the Coulomb energy. Most importantly we find that the lowest PL emission line is broad and increases in intensity with decreasing temperature. We associate this line with a magneto-roton minimum at finite momentum [18].

7.2 Experimental details

We have studied four different high-mobility ($> 5 \cdot 10^6 \mathrm{cm}^2/\mathrm{Vs}$) GaAs/AlGaAs single HJs with electron densities n_e=$(1.4 - 2.7) \cdot 10^{11}\mathrm{cm}^{-2}$. The samples are grown by MBE along the (100)-direction and have a thick GaAs buffer layer (width of 1μm). The n-type δ-doped layer is separated from the interface by an undoped AlGaAs layer. Polarized PL spectra were measured at temperatures 0.4 K and 1.2 K in magnetic fields up to 33 T in Faraday configuration. The sample was illuminated by a Ti:Sapphire laser tuned below the AlGaAs barrier with low power density ($< 10\mathrm{mW/cm}^2$) to prevent the sample from heating. Left and right circularly polarized PL was collected using optical fibers and circular polarizers. The spectra were dispersed by single grating spectrometer (Jobin Yvon HR640) and recorded by a liquid-nitrogen cooled CCD camera (PI TEK512x512 DB). The resolution of the system is 0.1 meV.

7.3 Experimental results

All four samples show a similar PL evolution with filling factor ν. Figure 7.1 shows the polarized PL of a HJ with $n_e = 2.7 \cdot 10^{11}\mathrm{cm}^{-2}$ in magnetic fields $B = 0 - 32$ T at 0.4 K. At $B = 0$ only PL from bulk excitons in the GaAs layer is observed around 1.515 eV [31]. With increasing magnetic field the energy of the bulk excitons shows a diamagnetic shift and the intensity in σ^+ polarization increases, while the intensity in σ^- polarization decreases. We have observed similar behavior in a pure GaAs reference sample.

At $\nu = 2$, the excitonic PL abruptly transfers its intensity to the σ^- emission from the 2DEG, and the PL peak energy jumps down to the energy of the optical transition between the lowest Landau levels of the 2D-electrons and valence holes [26, 27]. The precise origin of the sharp transitions from the bulk exciton to 2DEG-h PL at $\nu = 2$ and $\nu = 1$ is not fully understood yet [27, 28, 31], but can be phenomenologically explained by the dissociation of free excitons near the 2DEG into electrons and free itinerant valence holes [27]. As

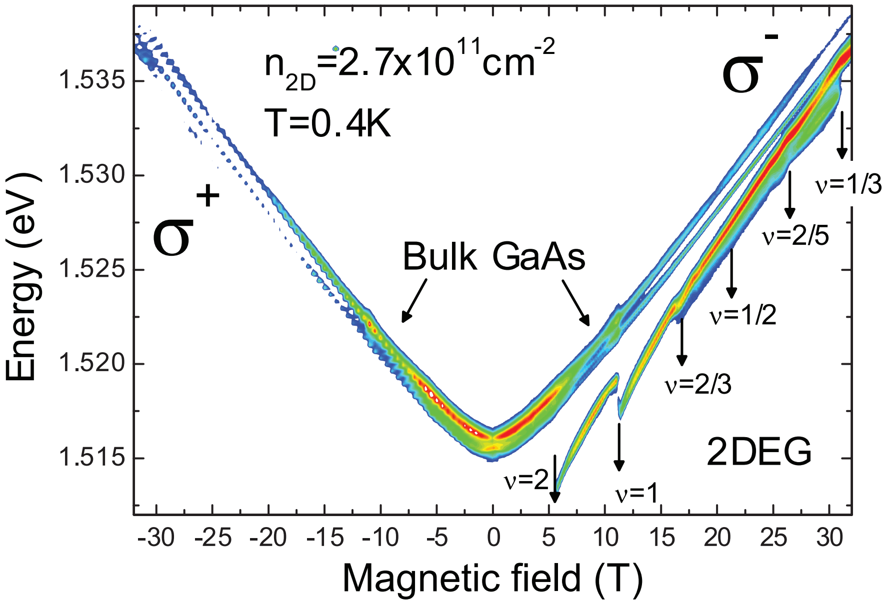

Figure 7.1: *Contour plot of the polarized emission spectra of a single HJ ($n_e = 2.7 \cdot 10^{11} cm^{-2}$) at temperature $T = 0.4\,K$ in magnetic fields up to 32 T. The false color scale indicates the intensity of the emission.*

shown in experiments with HJs of various densities, the interplay between the hole repulsion (due to the built-in HJ electric field) and the hole attraction to the 2DEG (depending on the 2DEG screening properties in magnetic field) controls the exciton to 2DEG-h PL changeover at integer filling factors. Here, we use the sharp discontinuity of the 2DEG-h PL energy at $\nu = 1$ to determine the 2DEG density, which roughly equals the density obtained from transport measurements. We note that the electron density decreases slightly when the magnetic field is increased. We found that this changed density is dynamical on a timescale of minutes.

In the following we will focus on the PL features in the FQH regime ($\nu < 1$). In contrast to the PL of QWs, the energy of which shows distinct jumps [16], we observe a relatively smooth shift of the energy of the main PL line. On top of this the PL has an internal structure around fractional filling factors $\nu = 2/3$ and for $1/3 < \nu < 2/5$. The latter regime corresponds to $1 < \nu^* < 2$ for composite fermions with two flux quanta attached (cf. Chapter 2). Figure 7.2a

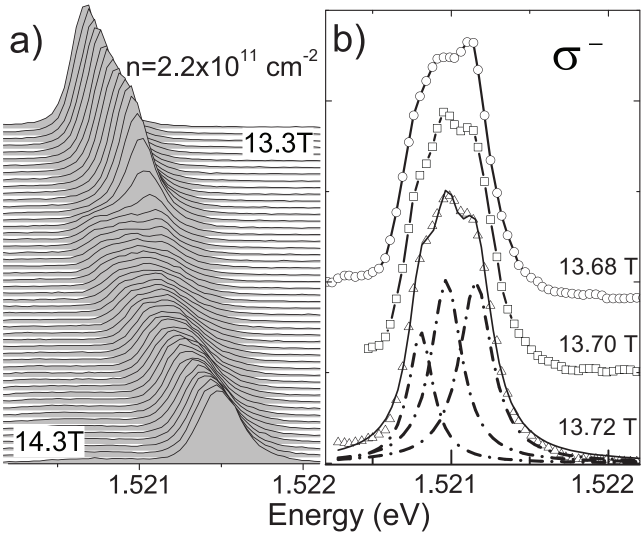

Figure 7.2: *PL of a 2DEG ($n_e = 2.2 \cdot 10^{11} cm^{-2}$) around $\nu = 2/3$ at 0.4 K in σ^- polarization. a) The spectra for $B = 13.3 - 14.3$ T with 0.02 T step. b) PL spectra fitted with three Lorentzian peaks.*

shows the PL spectra of a HJ sample with $n_e = 2.2 \cdot 10^{11}\,\text{cm}^{-2}$ around $\nu = 2/3$ at 0.4 K. Just below 13.3 T ($\nu \geq 0.68$), the PL spectrum consists of a single narrow peak with a line width of 0.2 meV. Around $\nu = 2/3$ ($B = 13.6\,\text{T}$), the peak abruptly splits into three lines with PL intensity transferring to the lowest-energy one. At higher B, the PL lines merge gradually into one single peak, which is slightly broader than 0.2 meV.

The energy and width of the peaks in the vicinity of $\nu = 2/3$ are obtained by fitting the PL spectra with three Lorentzians as shown in Figure 7.2b. We find that the three peaks are nearly equidistant with an energy separation of 0.15 meV and a width of 0.2 meV, as shown in Figure 7.3. The relative intensities of the peaks suggest a competition between different processes but this cannot be further quantified from these data. Note that the observation of three peaks at $\nu = 2/3$ differs from previous PL experiments on a similar sample [11], where only two peaks were observed.

The PL emission at higher B, i.e. when the filling factor is decreased below $\nu = 1/2$ is shown in Figure 7.4 for HJs with $n_e = 2.7 \cdot 10^{11}\text{cm}^{-2}$ and $n_e = 1.9 \cdot 10^{11}\text{cm}^{-2}$. Figure 7.5 shows the same data as Figure 7.4a, but now as a contour plot with the peak positions and their relative intensities indicated

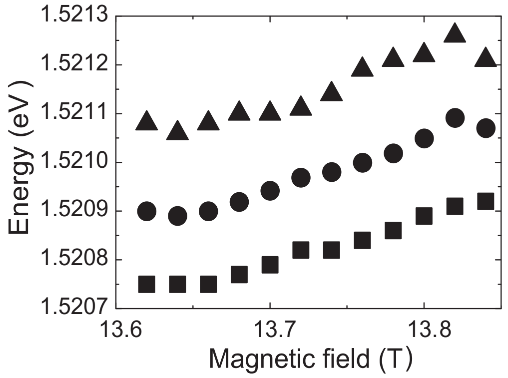

Figure 7.3: *PL energy of the* $n_e = 2.2 \cdot 10^{11} cm^{-2}$ *2DEG emission peaks at* $0.4 K$ *in* σ^- *polarization around* $\nu = 2/3$ *obtained by Lorentzian fits to the spectra.*

by the solid symbols.

Figure 7.6 shows the positions of the PL peaks ($n_e = 2.7 \cdot 10^{11}\mathrm{cm}^{-2}$), with a linear energy subtracted ($\approx$ 0.79 meV/T) to highlight the energy splittings. This linear energy shift corresponds to the cyclotron energy of excitons with an effective mass $0.074 m_e$. We observe emission of the bulk GaAs (higher emission energy, squares) and the 2DEG (lower emission energy, circles and triangles, marked by the dashed lines in Figure 7.4). Most remarkably, between $\nu = 2/5$ and $\nu = 1/3$ the emission peak splits into a doublet (circles in Figure 7.6), with a splitting Δ_2 of maximal 0.4 meV at 30.5 T. This splitting is preceded by the appearance of an additional peak at the low energy side (triangles in Figure 7.6), located approximately Δ_1 =1.2 meV below the center of the doublet. As the magnetic field is increased from $\nu = 2/5$, first the intensity of high energy peak decreases and a peak at the low energy side appears with increasing intensity. When the magnetic field is increased further the high-energy peaks splits into a doublet and gains intensity. When the magnetic field is increased, such that the filling factor $\nu < 1/3$, the doublet structure of the peak disappears, together with the peak on the low energy side. From the relative intensities of the emission from the 2DEG, we conclude that the doublet and the peak at the low energy side arise from competing processes.

The emission from the bulk GaAs (squares in Figure 7.6) does not show any anomalous behavior, which strongly suggests that the observed features are evidence of FQH states. This is supported by the fact that we only observe

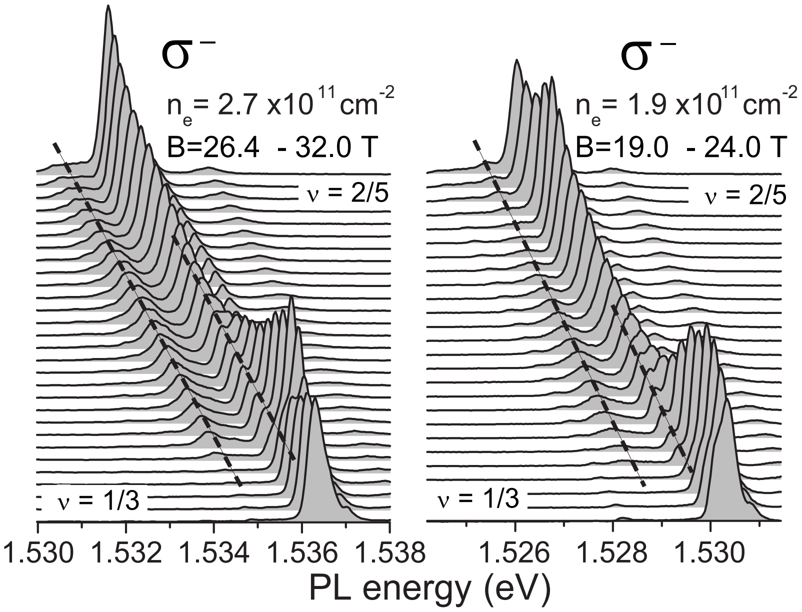

Figure 7.4: *PL of two HJs ($n_e = 2.7 \cdot 10^{11} cm^{-2}$ and $n_e = 1.9 \cdot 10^{11} cm^{-2}$) between $\nu = 2/5$ and $\nu = 1/3$ at a temperature of 0.4 K. The dashed lines are a guide to the eye to indicate the spectral features at fractional filling factors.*

these effects at low temperatures (0.4 K). The PL at $T = 1.2\,\mathrm{K}$ (cf. Figure 7.7 for the sample with $n_e = 2.7 \cdot 10^{11}\,\mathrm{cm}^{-2}$) does not show any anomalies and consists of a single peak. Most importantly, the extra peaks at low energy increase in intensity with decreasing temperature, opposite to the behaviour reported for QWs [9, 16].

Figure 7.8 shows PL spectra of three samples containing 2DEGs with different densities taken in the region between $\nu = 2/5$ and $\nu = 1/3$ where the observed doublet splitting is maximal. The dashed lines are a guide to the eye to indicate the splittings. The splitting increases with increasing electron density in the sample and with the magnetic field. Figure 7.9 shows the peak energies as function of the inverse magnetic length. Within the experimental accuracy, both the doublet splitting and the splitting between the doublet and the additional peak are inversely proportional to the magnetic length. This proportionality is expected from theory, since the energy splittings in the FQH regime scale with the Coulomb energy ($\sim e^2/l_B$) [22, 23].

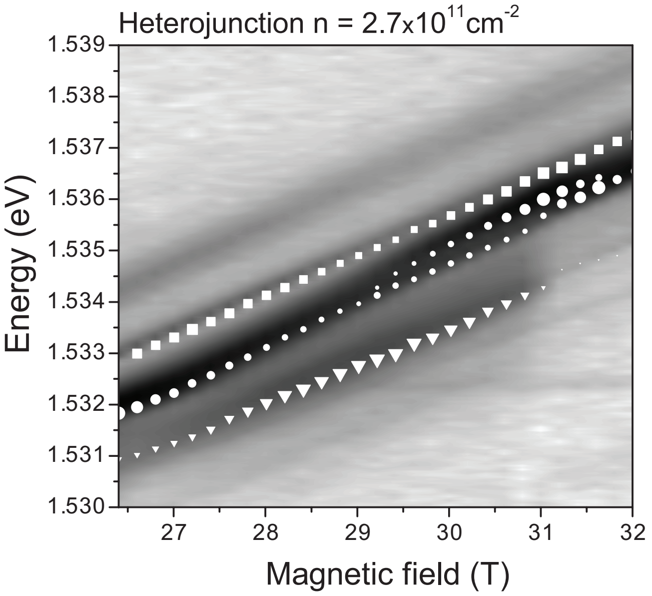

Figure 7.5: *PL of a $n_e = 2.7 \cdot 10^{11} cm^{-2}$ HJ between $\nu = 2/5$ and $\nu = 1/3$ at a temperature of 0.4 K. The solid symbols indicate the peak positions and their relative intensities. For visibility the symbols are rescaled to the maximum of each transition.*

7.4 Discussion

We identify the observed PL fine structure of our high quality HJs as the characteristic optical response of a 2DEG in the FQH regime, probed by a photo-excited hole at a distance much larger than the magnetic length ($d >> l_B$). Our experimental results are therefore an excellent basis to test theoretical calculations. Many theoretical papers have discussed this regime using several different approaches. One type of approach is to calculate the optical response starting from excitons [17, 18, 21, 32] or trions [23] that interact with the quasiparticles of the IQL. Due to the suppression of the exciton dispersion by the IQL the exciton recombination is strongly affected. This results in a doublet structure in the PL spectrum, one peak originating from the direct ($k = 0$) exciton recombination, whereas the other peak is due to magneto-roton assisted recombination, i.e. recombination with quasiparticles at finite momentum. These indirect transitions occur from an extensive area of k-space leading to a broad PL band at lower energy of the direct recombination. This leads to a peculiar

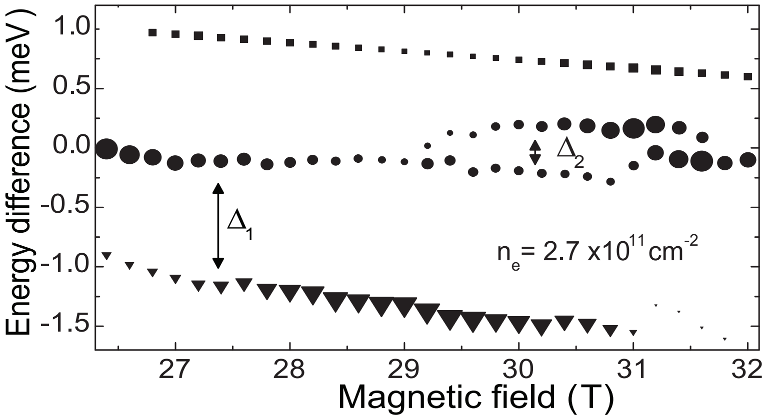

Figure 7.6: *Energy difference between the transitions with respect to the center of the doublet peak (i.e. a linear energy subtracted) for the HJ with* $n_e = 2.7 \cdot 10^{11}$ *cm*$^{-2}$. *The size of the symbols represents the amplitude of the transitions. For visibility the symbols are rescaled to the maximum of each transition.*

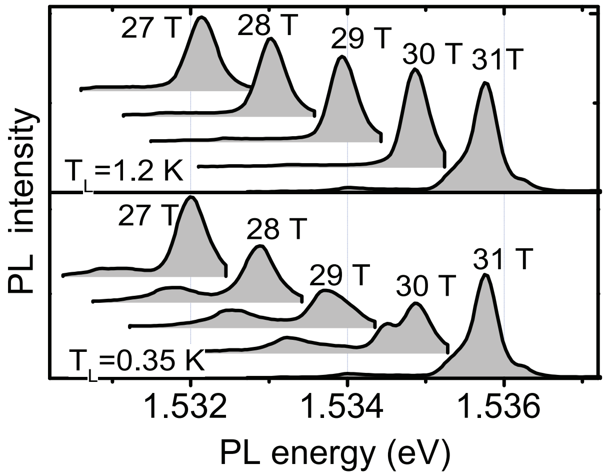

Figure 7.7: *Spectra at 0.4 K and 1.2 K for the HJ sample with* $n_e = 2.7 \cdot 10^{11}$ *cm*$^{-2}$

temperature dependence of the doublet for small d/l_B, which has been observed experimentally [9,16]: the higher energy peak ($k = 0$) peaks becomes more intense when the temperature is decreased, which indicates that the groundstate

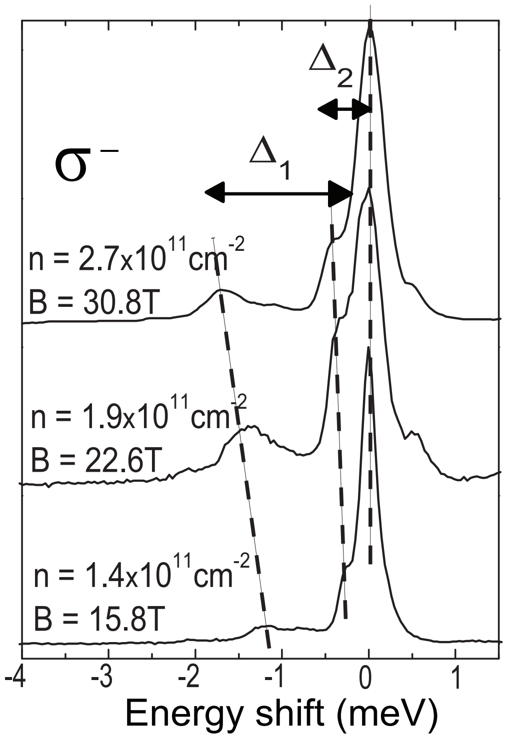

Figure 7.8: *Spectra in the region between $\nu = 2/5$ and $\nu = 1/3$ at 0.4 K for three samples with electron densities $n_e = 1.4 - 2.7 \cdot 10^{11} cm^{-2}$. The dashed lines are a guide to the eye to indicate the peak positions.*

of the initial photo-excited state is still at $k = 0$ [18].

An alternative theoretical approach calculates the optical spectrum starting from a free valence hole that interacts with quasi-particles of the IQL to form anyonic excitons [19,20,22,23] (cf. Chapter2), consisting of valence holes bound to several QEs of the IQL. At $\nu < 1/3$, there are no QEs available, and the spectrum consists of a single line due to the recombination of a hole with an electron in the condensate creating three QHs

$$h \rightarrow 3\text{QH} + \text{photon}, \tag{7.2}$$

The most interesting regime occurs for $1/3 < \nu < 2/5$ where (fractionally charged) hole-QE complexes are formed that can recombine via annihilation of n QEs and creation of $(3 - n)$ QHs within the condensate

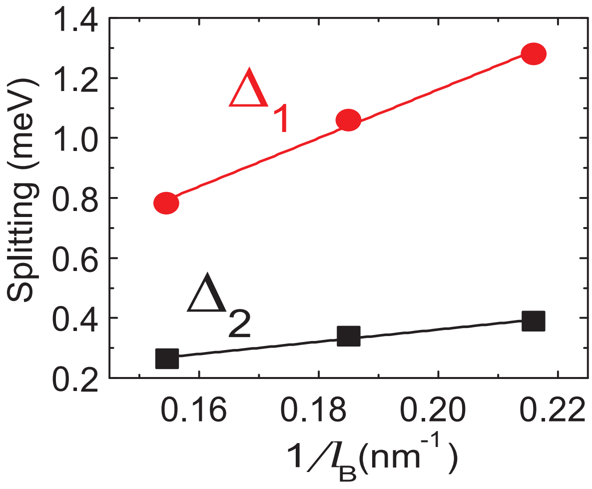

Figure 7.9: *Doublet splitting (circles) Δ_2 and energy difference between the doublet and the additional peak (squares) Δ_1 as function of $1/l_B$ for the three different samples. The lines are a linear fit to the data with a slope of* 8.1 ± 0.6 *meVnm and* 2.0 ± 0.2 *meVnm respectively.*

$$hQE_n \rightarrow (3-\mathrm{n})\mathrm{QH} + \mathrm{photon}, \tag{7.3}$$

with $n = 0, 1, 2$ or 3.

Despite their different approaches, all theories aforementioned predict the appearance of multiple PL lines around $\nu = 1/3$ in accordance with our experimental results. Without a dedicated calculation it is, however, difficult to obtain a definite identification of the transitions within the triplet fine structure. Qualitatively, we can say that the broad PL peak, observed at low energy, is due to the magnetoroton-assisted transition at finite momentum. This broad PL peak seems to have an additional internal structure (Figure 7.8), which supports the assumption that it arises from recombination of magnetoroton states over an extended range of k-values [16, 18, 23]. The energy gap between $k = 0$ and magnetoroton-assisted transitions is predicted to scale with the inverse magnetic length, which is consistent with the behavior of the splittings Δ_1. Finally, we observe a temperature dependence that is opposite to that of QWs: for lower temperatures the lowest-lying emission peak gains intensity (cf. Figure 7.7). This observation agrees with the theoretical prediction that at $d > l_B$ the indirect magneto-roton minimum becomes lowest in energy. In this case the competition of the direct and indirect recombination leads to a PL emission consisting of narrow and broad lines, with the latter becoming broader and more intense with increasing d/l_B and decreasing temperature. An alternative explanation is that the doublet structure around $\nu = 1/3$ is due to recombination of composite fermions with four flux quanta attached [33], which is consistent with the energy scales we find.

7.5 Conclusion

We have studied the correlations of electrons in the FQH regime by PL spectroscopy. We show that by using a 2DEG confined in a HJ, the photo-excited hole is sufficiently far away from the 2DEG to probe the electronic correlations rather than excitonic effects. We demonstrate that the electronic correlations lead to characteristic PL fine structure, consisting of PL triplets both at $\nu = 2/3$ and $\nu = 1/3$. We tentatively attribute the lowest peak in the emission between $\nu = 2/5$ and $\nu = 1/3$ to a magnetoroton-assisted transition corresponding to a FQH ground state of the photo-excited system at finite momentum.

References

[1] Tsui, D. C., Stormer, H. L., and Gossard, A. C. *Phys. Rev. Lett.* **48**, 1559 (1982).

[2] Laughlin, R. B. *Phys. Rev. Lett.* **50**, 1395 (1983).

[3] Haldane, F. D. M. *Phys. Rev. Lett.* **51**, 605 (1983).

[4] Chakraborty, T. and Pietilainen, P. *The Quantum Hall Effect.* 2 edition, (1995).

[5] Saminadayar, L., Glattli, D. C., Jin, Y., and Etienne, B. *Phys. Rev. Lett.* **79**, 2526 (1997).

[6] de Picciotto, R., Reznikov, M., Heiblum, M., Umansky, V., Bunin, G., and Mahalu, D. *Nature* **389**, 162 (1997).

[7] Kukushkin, I., Smet, J., von Klitzing, K., and Wegscheider, W. *Nature* **415**, 409 (2002).

[8] Kukushkin, I. V., Smet, J. H., Schuh, D., Wegscheider, W., and von Klitzing, K. *Phys. Rev. Lett.* **98**, 066403 (2007).

[9] Heiman, D., Goldberg, B. B., Pinczuk, A., Tu, C. W., Gossard, A. C., and English, J. H. *Phys. Rev. Lett.* **61**, 605 (1988).

[10] Goldberg, B. B., Heiman, D., Pinczuk, A., Pfeiffer, L., and West, K. *Phys. Rev. Lett.* **65**, 641 (1990).

[11] Turberfield, A. J., Haynes, S. R., Wright, P. A., Ford, R. A., Clark, R. G., Ryan, J. F., Harris, J. J., and Foxon, C. T. *Phys. Rev. Lett.* **65**, 637 (1990).

[12] Davies, H. D. M., Harris, J. C., Ryan, J. F., and Turberfield, A. J. *Phys. Rev. Lett.* **78**, 4095 (1997).

[13] Yusa, G., Shtrikman, H., and Bar-Joseph, I. *Phys. Rev. Lett.* **87**, 216402 (2001).

[14] Schüller, C., Broocks, K.-B., Schröter, P., Heyn, C., Heitmann, D., Bichler, M., Wegscheider, W., Chakraborty, T., and Apalkov, V. M. *Phys. Rev. Lett.* **91**, 116403 (2003).

[15] Hirjibehedin, C. F., Pinczuk, A., Dennis, B. S., Pfeiffer, L. N., and West, K. W. *Phys. Rev. Lett.* **91**, 186802 (2003).

[16] Byszewski, M., Chwalisz, B., Maude, D. K., Sadowski, M. L., Potemski, M., Saku, T., Hirayama, Y., Studenikin, S., Austing, D. G., Sachrajda, A. S., and Hawrylak, P. *Nature Physics* **2**, 239 (2006).

[17] Apalkov, V. M. and Rashba, E. I. *Phys. Rev. B* **46**, 1628 (1992).

[18] Apalkov, V. M. and Rashba, E. I. *Phys. Rev. B* **48**, 18312 (1993).

[19] Rashba, E. I. and Portnoi, M. E. *Phys. Rev. Lett.* **70**, 3315–3318 (1993).

[20] Portnoi, M. E. and Rashba, E. I. *Phys. Rev. B* **54**, 13791 (1996).

[21] Zang, J. and Birman, J. L. *Phys. Rev. B* **51**, 5574 (1995).

[22] Chen, X. M. and Quinn, J. J. *Phys. Rev. Lett.* **70**, 2130 (1993).

[23] Wójs, A. and Quinn, J. J. *Phys. Rev. B* **63**, 045303 (2000).

[24] Wójs, A., Gladysiewicz, A., and Quinn, J. J. *Phys. Rev. B* **73**, 235338 (2006).

[25] Bar-Joseph, I., Yusa, G., and Shtrikman, H. *Solid State Communications* **127**, 765 – 770 (2003).

[26] Nicholas, R. J., Kinder, D., Priest, A. N., Chang, C. C., Cheng, H. H., Harris, J. J., and Foxon, C. T. *Physica B* **249-251**, 553 – 557 (1998).

[27] Ashkinadze, B. M., Linder, E., Cohen, E., Rudenkov, V. V., Christianen, P. C. M., Maan, J. C., and Pfeiffer, L. N. *Phys. Rev. B* **72**, 075332 (2005).

[28] Ashkinadze, B. M., Voznyy, V., Cohen, E., Ron, A., and Umansky, V. *Phys. Rev. B* **65**, 073311 (2002).

[29] MacDonald, A. H., Rezayi, E. H., and Keller, D. *Phys. Rev. Lett.* **68**, 1939 (1992).

[30] Chen, X. M. and Quinn, J. J. *Phys. Rev. B* **50**, 2354 (1994).

[31] Ashkinadze, B. M., Linder, E., and Umansky, V. *Phys. Rev. B* **62**, 10310 (2000).

[32] Apalkov, V. M., Pikus, F. G., and Rashba, E. I. *Phys. Rev. B* **52**, 6111 (1995).

[33] Peterson, M. R. and Jain, J. K. *Phys. Rev. Lett.* **93**, 046402 (2004).

Summary

In this thesis we study the behaviour of electrons in low-dimensional semiconductor nanostructures, by exploring the energy levels of single electrons, and the correlations between the electrons. We find that not only the dimensionality is important, but also the material, the symmetry of the electronic bandstructure, the occupation of the electron levels and the surroundings of the nanostructure.

We give a general introduction and motivations in Chapter 1. Chapter 2 is an introduction to the basic physics of semiconductor nanostructures in magnetic fields. Here we explain the essential concepts of the different nanostructures, such as the concept of excitons and the energy scales.

We describe the experimental techniques that are used, in Chapter 3. One technique used is ensemble photoluminescence spectroscopy in pulsed magnetic fields up to 52 T at low temperatures, where timing and triggering play an important role, since the duration of the total magnetic field pulse is less than a second. The other technique we describe in this Chapter is spatially dependent time-resolved photoluminescence in continuous magnetic fields up to 33 T. We have designed an imaging setup which is minimally sensitive for displacements due to the magnetic field. It has a spatial resolution of 0.127 μm and a time resolution of 4 ps.

In Chapter 4 we present the results on the energy levels and charging spectra of holes in self-assembled InAs quantum dots obtained by capacitance-voltage and polarized photoluminescence spectroscopy. The magnetic field dependence of the single-particle hole energy levels can be understood by considering a spin-orbit coupled valence-band. To relate the spectroscopic properties to the structure of the quantum dots, we have performed a detailed structural characterization of the same dots based on cross-sectional scanning tunneling microscopy experiments on 13 individual quantum dots. This characterization reveals an ellipsoidal dot shape with an average height of 8 nm and a 26 nm diameter. The dots consist of an InGaAs alloy with a profound gradient in the indium concentration in both horizontal and vertical directions. We conclude this Chapter by the study of samples of InAs quantum dots grown on a template, which we have investigated in pulsed magnetic fields up to 42 T by means of polarized PL spectroscopy. The emission of these laterally coupled quantum dots changes significantly in high magnetic fields and we discuss the behavior of the PL energy, width and polarization.

We continue in Chapter 5 with the study of epitaxial InAs quantum rings, obtained by a change in the growth procedure of self-assembled InAs quantum dots. We have studied the exciton energy level structure of InAs/GaAs quantum rings. We show that the energy levels have features characteristic for excitons confined in a ring geometry. A model based on realistic parameters of the self-assembled quantum rings reproduces the essential features of the observed photoluminescence spectra on the basis of the calculated optical transition probabilities. Also we discuss the photoluminescence of single quantum rings in magnetic fields up to 30 T. Here we probe the ground state of individual rings, in contrast to the ensemble measurements.

We change from from semi two-dimensional epitaxial quantum dots to true zero-dimensional colloidal quantum dots in the Chapter 6. We show that small changes in the shape of colloidal CdSe nanocrystals have a dramatic effect on their magneto-optical properties. The photoluminescence emission energy of the two circular polarizations of quantum rods shows a giant splitting at 8 T, substantially larger than that of spherical quantum dots. Also we find that the quantum-rod photoluminescence has a circular polarization opposite to that of quantum dots and is dominated by emission from higher lying exciton levels. We explain these results by an empirical, effective-mass model for the exciton fine structure of quantum rods, in which the exciton levels are strongly mixed in a magnetic field. In the remainder of Chapter 6 we study the polarized photoluminescence of spherical nanocrystals of different materials: CdSe, CdTe, PbSe and PbS. We show that the degree of circular polarization of their emission is remarkably similar, despite their very different crystal and electronic band structures.

Finally, in Chapter 7 we move to the physics of two-dimensional systems at very low temperatures in high magnetic fields, where electron correlations dominate. We report the observation of a fine structure in the photoluminescence emission of high mobility GaAs/AlGaAs single heterojunctions in the fractional quantum Hall regime. We find a splitting of the emission peak into three lines both at filling factor $\nu = 2/3$ and in the region $1/3 < \nu < 2/5$. The dependencies on magnetic field strength, electron density and temperature show that the fine structure arises from recombination of fractionally-charged elementary excitations of the two-dimensional electron liquid and a photo-excited valence band hole. These quasi-particle excitations have a dispersion relation with a minimum at finite momentum.

Samenvatting

In dit proefschrift bestuderen we het gedrag van elektronen in laag-dimensionale halfgeleider nanostructuren door de energieniveaus van enkele elektronen te onderzoeken alsmede de correlaties tussen elektronen onderling. We zien dat niet alleen de dimensie een belangrijke rol speelt, maar ook het materiaal, de symmetrie van de electronische bandstructuur, de bezetting van de elektronniveaus en de omgeving van de nanostructuur.

We geven een algemene inleiding en motivaties voor dit werk in Hoofdstuk 1. Hoofdstuk 2 is een inleiding tot de concepten die ten grondslag liggen aan de fysica van halfgeleider nanostructuren in magneetvelden. We lichten de essentiële ingrediënten toe, waaronder het concept exciton en de belangrijke energie schalen.

We beschrijven de technieken die we gebruikt hebben in Hoofdstuk 3. Eén van de gebruikte technieken is fotoluminescenctie spectroscopie van een ensemble nano-objecten in gepulste magneetvelden tot 52 T bij lage temperaturen. Hier spelen timing en triggering een belangrijke rol, omdat de totale magneetveldpuls korter is dan een seconde. De andere techniek die we beschrijven in dit hoofdstuk is plaats-en tijdopgeloste fotoluminescentie in continue magneetvelden tot 33 T. We hebben een imaging-opstelling ontworpen die zeer ongevoelig is voor verplaatsingen ten gevolge van van het aangelegde magneetveld. De opstelling heeft een ruimtelijke resolutie van $0.127\,\mu$m en een tijdsresolutie van 4 ps.

In Hoofdstuk 4 laten we de resultaten zien die de energieniveaus en het laden van gaten in self-assembled InAs quantum dots beschrijven. Deze resultaten hebben we verkregen door capaciteits-spannings metingen en gepolarizeerde fotoluminescentie spectroscopie. De magneetveldafhankelijkheid van de energieniveaus van individuele gaten kan worden begrepen door een spin-baan gekoppelde valentieband te beschouwen. Om de spectroscopische eigenschappen van de quantum dots te relateren aan hun structuur, hebben we een gedetailleerde karakterisatie gemaakt van de structuur op grond van cross-sectional scanning tunneling microscopy experimenten aan 13 individuele quantum dots. Deze karakterisatie laat zien dat de dots ellipsvormig zijn, een gemiddelde hoogte hebben van 8 nm en een diameter van 26 nm. De dots bestaan uit een InGaAs legering met een sterke gradiënt van de indium concentratie in zowel de horizontale als vertikale richting. We besluiten dit hoofdstuk met de studie van clusters InAs quantum dots die op een template gegroeid zijn. We hebben deze onderzocht in gepulste magneetveelden tot 42 T en met behulp van gepolarizeerde fotoluminescentie spectroscopie. De emissie van deze lateraal gekoppelde quantum dots verandert aanzienlijk in hoge magneetvelden en we bespreken het gedrag van de emissie energie, de breedte van het spectrum en de polarizatie.

We vervolgen in Hoofdstuk 5 met het onderzoek naar epitaxiale InAs quantum ringen, die verkregen zijn door de groeiprocedure van InAs quantum dots aan te passen. We hebben de energieniveaus van excitonen bestudeerd in deze InAs/GaAs quantum ringen. We laten zien dat de energieniveaus karakteristieke eigenschappen hebben door de ringstructuur waarin ze opgesloten zijn. Een model gebaseerd op realistische parameters voor deze ringen reproduceert de essentiële kenmerken van de gemeten fotoluminescentie spectra. Verder bespreken we de fotoluminescentie van individuele ringen tot 30 T. In tegenstelling tot de ensemble metingen, kijken we hier naar de grondtoestand van de ringen.

In Hoofdstuk 6 gaan we over van semi-tweedimensionale nanostructuren naar echte nuldimensionale nanokristallen. We laten zien dat kleine veranderingen in de vorm van CdSe nanokristallen een enorm effect hebben op hun optische eigenschappen in magneetvelden. De fotoluminescentie emissie energie van de twee circulair gepolarizeerde componenten van nanostaafjes heeft een zeer grote opsplitsing bij 8 T, die veel groter is dan voor ronde nanokristallen. Ook observeren we dat de circulaire polarizatie van staafjes tegengesteld is aan die van bolletjes. We laten zien dat deze waarnemingen begrepen kunnen worden met een empirisch model, gebaseerd op effectieve-massa berekeningen, als we aannemen dat de energieniveaus van excitons worden gemengd in een magneetveld. In het resterende deel van Hoofdstuk 6 bekijken we de gepolarizeerde emissie van nanokristallen gemaakt van verschillende materialen: CdSe, CdTe, PbSe en PbS. We zien dat hun gepolarizeerde emissie erg op elkaar lijkt, hoewel de materiaaleigenschappen zeer verschillend zijn.

Tenslotte gaan we in Hoofdstuk 7 over naar de natuurkunde van tweedimensionale systemen bij zeer lage temperaturen en hoge magneetvelden. Hier domineren de correlaties tussen elektronen. We zien in ons experiment een fijnstructuur in de fotoluminescentie emissie van hoge-mobiliteits GaAs/AlGaAs heterostructuren in het regime van het fractionele quantum Hall effect. We zien een opsplitsing van de emissie, zowel rond vulfactor $\nu = 2/3$ en in het gebied $1/3 < \nu < 2/5$. De afhankelijkheid van deze opsplitsing als functie van het magneetveld, de elektronen dichtheid en de temperatuur, laat zien dat de fijnstructuur een gevolg is van de recombinatie van fractioneel geladen excitaties van het tweedimensionale elektronsysteem met een foto-geëxciteerd gat uit de valentieband. Deze quasi-deeltjes hebben een dispersierelatie met een minimum bij een eindige impuls.

List of Publications

- J.H. Blokland, P.C.M. Christianen, B.M. Ashkinadze, V.V. Rudenkov, L.N. Pfeiffer, and J.C. Maan: *Optical Probing of Electronic Fractional Quantum Hall States*, *submitted to Physical Review Letters* (2009)

- N.A.J.M. Kleemans, J.H. Blokland, A.G. Taboada, H.C.M. van Genuchten, M. Bozkurt, V.M. Fomin, V.N. Gladilin, D. Granados, J.M. García, P.C.M. Christianen, J.C. Maan, J.T. Devreese, and P.M. Koenraad: *Excitonic behavior in self-assembled InAs/GaAs quantum rings in high magnetic fields* , Physical Review B **80**, 155318 (2009)

- L. Turyanska, U. Elfurawi, M. Li, M.W. Fay, N.R. Thomas, Stephen Mann, J.H. Blokland, P.C.M. Christianen and Amalia Patane: *Tailoring the physical properties of thiol-capped PbS quantum dots by thermal annealing*, Nanotechnology **20** 315604 (2009)

- V.M. Fomin, V.N. Gladilin, J.T. Devreese, J. H. Blokland, P C.M. Christianen, J.C. Maan, A G. Taboada, D. Granados, J. M. Garcia, N.A.J M. Kleemans, H.C.M. van Genuchten, M. Bozkurt, and P.M. Koenraad: *Electronic and excitonic properties of self-assembled semiconductor quantum rings*, Proc. SPIE **7364**, 736402 (2009)

- G. Pettinari, A. Polimeni, M. Capizzi, J.H. Blokland, P.C.M. Christianen, J.C. Maan, V. Lebedev, V. Cimalla, and O. Ambacher: *Carrier mass measurements in degenerate indium nitride*, Physical Review B **79**, 165207 (2009)

- J.H. Blokland, M. Bozkurt, J.M. Ulloa, D. Reuter, A. D. Wieck, P. M. Koenraad, P. C. M. Christianen and J. C. Maan: *Ellipsoidal InAs quantum dots observed by cross-sectional scanning tunneling microscopy*, Applied Physics Letters **94**, 023107 (2009)

- F.J.P. Wijnen, J.H. Blokland, P. C. M. Christianen and J. C. Maan: *Competition between zero-phonon and phonon-assisted luminescence in colloidal CdSe quantum dots*, Physical Review B **78**, 235318 (2008)
- G. Pettinari, A. Polimeni, M. Capizzi, J.H. Blokland, P. C. M. Christianen, J. C. Maan, E.C. Young and T. Tiedje: *Influence of bismuth incorporation on the valence and conduction band edgeds of* $GaAs_{1-x}Bi_x$, Applied Physics Letters **92**, 262105 (2008)
- Vojislav Krstic, Dirk Obergfell, Stefan Hansel, Geert L. J. A. Rikken, Janneke H. Blokland, Mauro S. Ferreira, Siegmar Roth: *Graphene-Metal Interface: Two-Terminal Resistance of Low-Mobility Graphene in High Magnetic Fields*, Nano Letters **8**, 1700-1703 (2008)
- J.H. Blokland: *Elektronen en gaten in halfgeleiderquantumdots. Nederlands Tijdschrift voor Natuurkunde*, **73**, 88-91 (2007)
- J.H. Blokland, F.J.P. Wijnen, P.C.M. Christianen, U. Zeitler and J.C. Maan: *Hole levels in InAs self-assembled quantum dots*, Physical Review B **75**, 233305 (2007)

Curriculum Vitae

Janneke Blokland werd op 5 november 1982 geboren te Tiel. In 2001 behaalde ze haar VWO diploma op het Lingecollege te Tiel en begon hetzelde jaar aan de opleiding Natuur- en Sterrenkunde aan de Radboud Universiteit Nijmegen.

In 2006 studeerde ze *cum laude* af in de experimentele fysica na een afstudeerstage in de groep experimentele vastestof fysica, resulterend in de scriptie *Hole levels in semiconductor quantum dots.* Dit werk is voortgezet als onderdeel van het promotie-onderzoek dat tot dit proefschrift heeft geleid. Per januari 2010 is Janneke werkzaam als post-doc verbonden aan het Fritz-Haber-Institut der Max-Planck-Gesellschaft te Berlijn.